

Catalytic methane conversion with single-site porous catalysts: a computational approach

Szécsényi, Ágnes

DOI

[10.4233/uuid:ed0bee26-e6f7-45c0-a56d-1b3fdfbac1e2](https://doi.org/10.4233/uuid:ed0bee26-e6f7-45c0-a56d-1b3fdfbac1e2)

Publication date

2019

Document Version

Final published version

Citation (APA)

Szécsényi, Á. (2019). *Catalytic methane conversion with single-site porous catalysts: a computational approach*. [Dissertation (TU Delft), Delft University of Technology]. <https://doi.org/10.4233/uuid:ed0bee26-e6f7-45c0-a56d-1b3fdfbac1e2>

Important note

To cite this publication, please use the final published version (if applicable). Please check the document version above.

Copyright

Other than for strictly personal use, it is not permitted to download, forward or distribute the text or part of it, without the consent of the author(s) and/or copyright holder(s), unless the work is under an open content license such as Creative Commons.

Takedown policy

Please contact us and provide details if you believe this document breaches copyrights. We will remove access to the work immediately and investigate your claim.

**CATALYTIC METHANE CONVERSION WITH
SINGLE-SITE POROUS CATALYSTS: A
COMPUTATIONAL APPROACH**

CATALYTIC METHANE CONVERSION WITH SINGLE-SITE POROUS CATALYSTS: A COMPUTATIONAL APPROACH

Dissertation

for the purpose of obtaining the degree of doctor
at Delft University of Technology,
by the authority of the Rector Magnificus Prof.dr.ir.T.H.J.J. van der Hagen,
chair of the Board of Doctorates,
to be defended publicly on
Wednesday 4 September 2019 at 15:00 o'clock

by

Ágnes SZÉCSÉNYI

Master of Science in Chemical Engineering,
Budapest University of Technology, Hungary
born in Szekszárd, Hungary.

This dissertation has been approved by the promotor.

promotor: prof. dr. E. A. Pidko

promotor: prof. dr. J. Gascon

Composition of the doctoral committee:

Rector Magnificus,	chairperson
Prof. dr. E. A. Pidko	Delft University of Technology, promotor
Prof. dr. J. Gascon	Delft University of Technology, King Abdullah University of Science and Technology, Saudi Arabia, promotor

Independent members:

Prof. dr. ir. F. Kapteijn	Delft University of Technology
Prof. dr. A. Urakawa	Delft University of Technology
Prof. dr. ir. V. van Speybroeck	Ghent University, Belgium
Prof. dr. F. Studt	Karlsruher Institut für Technologie, Germany
Prof. dr. D. de Vos	KU Leuven, Belgium

The research presented in this thesis was performed at the Catalysis Engineering section of the Chemical Engineering at the faculty of Applied Sciences of Delft University of Technology. The research was funded by the Nederlandse Organisatie voor Wetenschappelijk Onderzoek (NWO) (VIDI grant agreement 723.012.107-MetMOFCat). SurfSARA and NWO are acknowledged for providing access to the supercomputer facilities.

Dissertation, Delft University of Technology

With summary in Dutch

Cover illustration: <https://www.deviantart.com/maparthur>. Printed with permission.

ISBN: 978-94-028-1630-3

Printed by Ipskamp Printing, Enschede

Copyright © 2019 by Ágnes Szécsényi

So long, and thanks for all the fish.

Douglas Adams

CONTENTS

1	Introduction	1
2	Methane oxidation over Fe-ZSM-5 zeolite – theory of C-H bond activation	29
3	Methane oxidation over Fe-MIL-53(Al) – analysis of overoxidation and H₂O₂ decomposition pathways	55
4	Secondary effects in methane activation over Fe-ZSM-5	71
5	Analysis of C-H bond activation with multireference CASSCF/CASPT2 method	89
	Summary	131
	Acknowledgements	143
	List of Publications	145
	Curriculum Vitæ	147

1

INTRODUCTION

This chapter is based on the following publication: A. I. Olivos-Suarez, Á. Szécsényi, E. J. M. Hensen, J. Ruiz-Martinez, E. A. Pidko, and J. Gascon, Strategies for the Direct catalytic valorization of methane using heterogeneous catalysis: challenges and opportunities, *ACS Catalysis*, **6** (2016) 2965-2981.

1.1. OPPORTUNITIES IN METHANE VALORIZATION

FUELS and chemical feedstocks are important commodities with a great direct impact on the development of society that currently relies on fossil fuels. Transportation (air, ground, and sea) and manufacture of goods, from petrochemical feedstocks to plastics and rubber industries, depend heavily on oil as a raw material. With the rapidly growing world population, the need to increase standards of living, and the dwindling world oil reserves per capita [1], a sustainable plan to couple an economically viable energy model with an environmentally friendly solution is the topic of many debates. Although more and more attention is given to research into renewables, the interest in improving current oil technologies is still pragmatically valid because most of the technologies applying renewable energies are in a very early stage of development, and it will be rather difficult to implement them within a realistic time frame.

An essential prerequisite to implement greener technologies is the efficient use of nonrenewable sources of hydrocarbons. Naturally, this highlights the necessity to further develop efficient technologies for the valorization of methane. Indeed, the enormous gas reserves found (208 trillion cubic feet proven) [2] environmental sustainability, and lower overall costs point to natural gas as the primary source for energy and chemicals in the near future and to methane hydrates as the most important source of hydrocarbons in the long term. Hence, it is not surprising that methane valorization has been a hot topic over the last few decades, as highlighted in several excellent reviews. [3–6]

Natural gas is a mixture of gaseous hydrocarbons with varying quantities of nonhydrocarbons, which normally are considered impurities. Methane is the main component of natural gas, followed by a range of hydrocarbons such as propane and butane. It is also a byproduct from oil refining and chemical processing. It has potential value as a cleaner source of fossil energy and as raw material provided that it can be brought economically to the point of use. [4] In this respect, it would be highly desirable to convert methane to a product (chemical or fuel) that could be easily transported. Although compressed natural gas is a feasible transportation fuel for truck and bus fleets, there are still doubts about the feasibility of running smaller vehicles on this technology. Moreover, bearing in mind that methane is, without any doubt, the main potential source of carbon for the synthesis of chemical commodities, its transformation into more useful products is of the utmost importance, and from the chemocatalytic point of view, the direct activation of methane is one of the remaining grand challenges. [7, 8]

The challenge of methane activation is related to the high stability of this com-

Table 1.1: Overview of the principal reactions in syngas production

Process	Main reaction	ΔH_r^0 (kJ/mol)	H ₂ /CO ratio	Temp. (K) [P (atm)]	Ref.
Steam reforming	$\text{CH}_4 + \text{H}_2\text{O} \rightleftharpoons \text{CO} + 3 \text{H}_2$	206	3:1	1050-1250 (20-30)	[6, 15]
Dry reforming	$\text{CH}_4 + \text{CO}_2 \rightleftharpoons 2 \text{CO} + 2 \text{H}_2$	247	1:1	>1000	[14, 16]
Oxy-reforming	$\text{CH}_4 + 0.5 \text{O}_2 \rightleftharpoons \text{CO} + 2 \text{H}_2$	-36	2:1	>1000 (1)	[17, 18]

pound. Methane is a very stable and symmetrical molecule that does not possess any dipolar moment or functionality that would allow for directing chemical reactions. The activation of the methane C-H bond in the gas phase usually requires high temperature and leads mostly to radical reactions with intrinsic low selectivity. [9]

Because of these reasons, nowadays the industrial transformation of methane into useful chemicals and liquid fuels is only feasible via synthesis gas, [6] a mixture of molecular hydrogen and carbon monoxide, that can be further transformed to methanol or to hydrocarbons under moderate reaction conditions (423-623 K and 10-100 bar) via the Fischer-Tropsch synthesis (Figure 1.1). [10] Other important processes based on syngas are the Haber-Bosch process for ammonia production [11] and the oxo-process [12] for higher chain aldehydes/alcohols production. Although indirect routes are chemically inelegant ways of converting methane (CH₄ first has to be oxidized to CO and further reduced to the final desired products), the direct alternatives have proven difficult to control because of low yields, selectivity, and productivity. In addition to this, the engineering of syngas production is a highly developed and optimized technology, especially at large scales. Table 1.1 summarizes the major processes used for syngas production, that is, steam methane reforming [6] (SMR), partial oxidation or oxy-reforming (can be coal gasification or from methane), and autothermal reforming (formally a combination of SMR and partial oxidation). [13] Methane reforming with CO₂, known as dry reforming, is a potential technology that has not reached enough efficiency to be applied at industrial scale. However, it is very attractive because it utilizes CO₂ as an oxidant, thus using two of the major green house gases. [14]

Indirect routes via syngas have progressed substantially in terms of commercial development [2]. Analysis of the economics of these processes reveals that a majority of the capital investment is associated with synthesis gas generation [19].

This hampers syngas production from remote and small sources of natural gas where, in most cases, it is just flared and is the main motivation for the search of new processes in which methane is initially activated and preferably converted to a valuable chemical in a single step. This challenge has prompted intense research into the development of homo- and heterogeneous catalysts for this reaction, avoiding in this

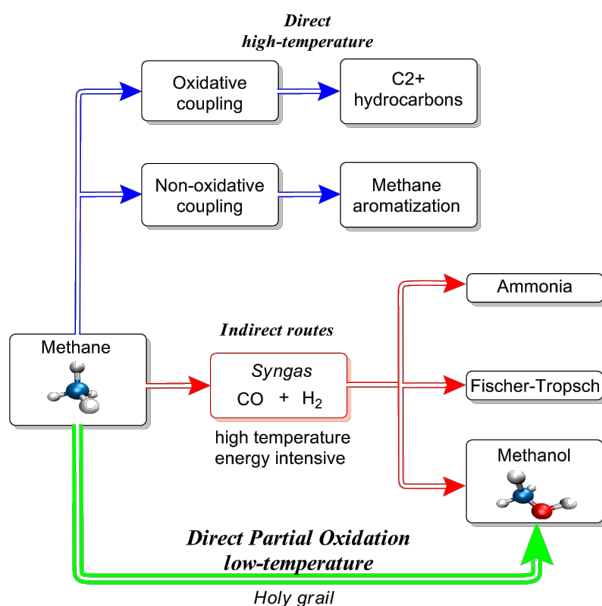


Figure 1.1: Overview of the different routes for the valorization of methane.

way the generation of syngas and eventually allowing the use of such technologies at much smaller scales.

1.2. MECHANISTIC CONSIDERATIONS

METHANE functionalization under mild conditions has been long considered difficult, if not impossible, because of the nonpolar character of its C-H bonds and its low-lying highest occupied molecular orbital (HOMO) and high-lying lowest unoccupied molecular orbital (LUMO). These fundamental properties make methane rather inert toward most common organic chemistry strategies for functionalization.

Activation through either nucleophilic or electrophilic attack has proven difficult to be achieved and controlled. Alternative approaches involving partial oxidation have been intensively investigated since the 1960s [9, 20–23]. In principle, the ability to activate this rather unreactive C-H bond should enable numerous reactions for methane functionalization. However, the C-H bond activation, although a prerequisite, is not the only challenge in methane functionalization (see Figure 1.2). In fact, subsequent reactions, where the functionalization occurs, have received far less attention, in spite of the growing evidence that the activation of the oxidant represents a key challenge in closing the catalytic cycle. Thus, to achieve selective methane oxidation, the cleavage of the C-H bond has to be achieved, but equally important, the activation of the oxidant to form and regenerate the active site has to be compatible with the C-H bond

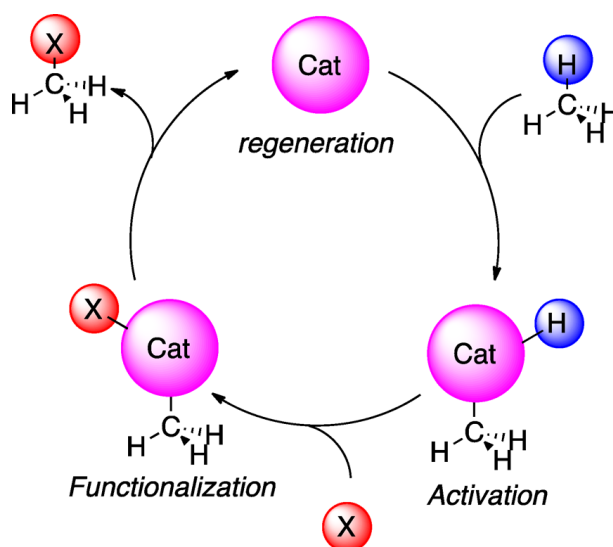


Figure 1.2: Main components of the catalytic cycle for methane functionalization

activation step. Indeed, selectivity is an issue because the low reactivity of the C-H bond requires the use of either harsh reaction conditions or highly reactive reagents [24–26] and this is the main paradigm in methane activation.

1.2.1. C-H BOND ACTIVATION

Most of the literature dedicated to methane activation focuses on understanding the mechanism of C-H bond activation, namely, the cleavage of the strongest and the least-polar carbon-hydrogen bond [24]. Excellent examples by Shilov [25] and by Copéret [26] offer representative overviews of strategies in homogeneous and heterogeneous catalysis. For metal-based catalytic systems, Shilov classifies C-H activation into three main mechanisms, as described in the following sections.

Heterolytic dissociation or "true" activation is one of the most widely encountered mechanisms in transition metal (TM) catalysis: the C-H bond cleavage is promoted through the direct interaction with the metal at the catalytic site, resulting in the formation of a σ M-C bond. This type of reactivity can be further classified according to the electronic nature of the interaction between the C-H bond and the catalyst (see Figure 1.3) [27, 28]. With respect to their relevance for catalytic methane functionalization, we have encountered three classes: oxidative addition, electrophilic activation, and Lewis acid/base [26]. Conceptually, the latter has been used extensively to describe mostly heterogeneous systems. However, it is related to electrophilic activation and mechanistically is a σ -bond metathesis [29].

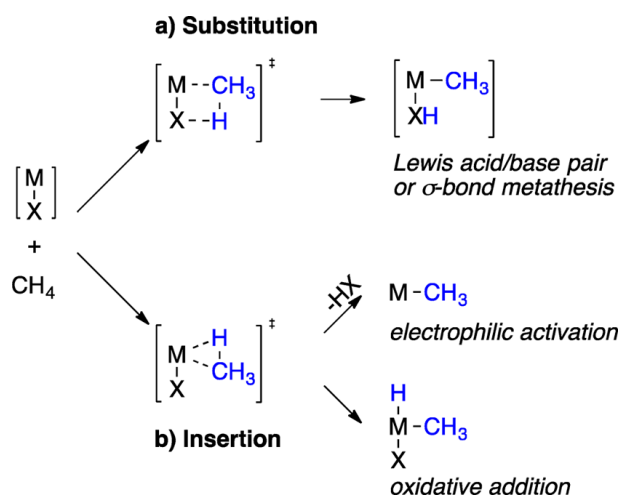


Figure 1.3: Schematic representation of the heterolytic C-H bond activation mechanism: (a) Substitution: the catalyst can be represented by Lewis acid-base pair or formally σ -bond metathesis; (b) Insertion: based on the electronic character of the transition state can be further classified as oxidative addition or electrophilic activation.

Purely based on electronics, analyses of the M-C bonding schemes at the transition states of several complexes have shown that C-H bond activation can be classified as nucleophilic, ambiphilic, and electrophilic [27]. For both, the insertion and the substitution mechanism, the type of reactivity is determined by the total charge transfer from the metal (occupied $d\pi$ orbital) to the C-H bond (empty σ^* orbital) as well as the back-donation from C-H bond (occupied σ orbital) to the metal (empty $d\sigma$ orbital). Oxidative addition can be described as a purely nucleophilic activation (formally only donation from metal to C-H occurs) [28].

For active centres that are composed of electron-deficient metals, the active site can be described as a Lewis acid/base pair. The Lewis acidic metal site (**M**) polarizes the C-H bond to promote its heterolytic dissociation, yielding a σ -bonded M-CH₃ species. The base site (**X**) accepts a proton and provides substantial stabilization to the reaction products (Figure 1.3a). In heterogeneous catalysis, such M-X acid-base pairs are commonly formed on oxide surfaces by under-coordinated Lewis acidic surface metal sites and neighbouring basic oxygen centres. One of the most important examples of such mechanisms is the methane activation in oxidative coupling (OCM) by Li-doped MgO catalyst. Recent experimental and theoretical studies in this reaction revealed that the C-H bond activation takes place over the acid-base pairs involving Mg²⁺ and O²⁻ ions on the edges and steps of the MgO surface [30].

As already anticipated above, oxidative addition (Figure 1.3b) involves electron-rich TM centres in low oxidation states (usually late-transition-metal complexes) and C-H

bond activation proceeds over a single transition-metal site. This reaction starts with the formation of a σ -complex with the coordinatively unsaturated metal centre. The back-donation of two electrons from the metal d-orbitals to the σ^* C-H orbital is the driving force for the C-H bond cleavage, yielding a hydride and CH_3 anion fragment bound to the $2e^-$ oxidized transition-metal species [31, 32].

In the third mechanism, the metal centre has to be in a high oxidation state, electron-deficient, and a coordinatively unsaturated species, thus facilitating electrophilic activation. The organometallic M-C species is encountered only as a transient intermediate, and due to the high oxidation state of the metal centre, these catalysts can withstand polar media such as water or strong acids. This stability enables the use of strong oxidants, contrary to species that undergo oxidative addition where only weak or no oxidants are applicable. Pioneering in this field, Shilov chemistry [33] using Pt^{IV} salts is perhaps one of the most important breakthroughs in C-H bond activation. Importantly, a methyl-platinum(IV) was observed supporting the Pt mediated C-H bond activation via the organometallic intermediate.

Homolytic dissociation or "fake" activation occurs when the metal site is not accessible and methane activation is dominated by the interaction with the surrounding basic ligands. Typically, oxygen atoms at the coordination sphere (or at the surface for heterogeneous catalysts) are responsible for the hydrogen atom abstraction (HAA) [34] from methane, hence activating the C-H bond. This homolytic C-H bond activation mechanism results in the formation of "free" methyl radicals (Figure 1.4).

Most of the examples on partial methane oxidation, including homogeneous, heterogeneous, and enzymatic catalytic systems, involve the homolytic activation mechanism with the aid of electrophilic oxygen. The metal at the active site can have variable oxidation state, and (although it can be argued) 3d transition metals are the most favourable for oxidation reactions via electrophilic oxygen active centres (*vide infra*). Due to the natural abundance of Fe-based enzymes for hydroxylation reactions, most of the research for characterization and toward understanding of the active species in catalysis has focused on Fe^{IV} -oxo cores. However, there is no fundamental reason that this reactivity cannot be encountered for other 3d late transition metals (i.e., Cu or Co).

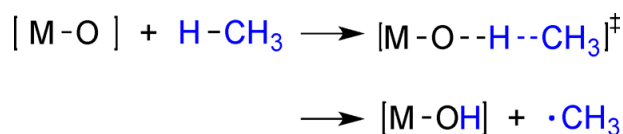


Figure 1.4: Schematic representation of the homolytic dissociation of C-H bond

Based on molecular orbital theory, there are two possibilities in which an electrophile can approach methane and effectively carry out the HAA: the σ -channel and π -channel mechanism [35, 36]. In the first, the electrophilic orbital that participates in the H-abstraction (from a σ_{CH}) is an empty $\sigma^*(\text{Fe-}3d_{z^2}\text{-O-}2p_z)$ of the metal-oxo complex, while in the second case, an empty $\pi^*(\text{Fe-}3d_{xz/yz}\text{-O-}2p_{x/y})$ promotes the reaction. Figure 1.5 shows the simplified frontier molecular orbital diagram and schematic representation of the electron-accepting orbitals of the high spin (HS) $[\text{FeO}(\text{H}_2\text{O})_5]^{2+}$ and the low spin (LS) $[\text{FeO}(\text{NH}_3)_4(\text{H}_2\text{O})]^{2+}$ species, model compounds investigated by Baerends and Kazaryan [37]. The LUMO of the HS compound (Figure 1.5a) is the $d_{xy}(\beta)$ orbital; however, this orbital cannot overlap with the HOMO of methane, because it is exclusively located on the iron centre. The electron acceptor LUMO+1 is the $\sigma^*(\alpha)$ orbital, which is able to accept an α electron from methane, coupled antiferromagnetically to a methyl radical in the transition state. It was observed that the spin state is affected by ligand effects (more electron-donating ligands lead to low spin ground state configuration), and both the spin state and the ligand field significantly influence the reactivity of the FeO^{2+} species and therefore the C-H bond activation mechanism. In the more active HS $[\text{FeO}(\text{H}_2\text{O})_5]^{2+}$ species, the σ -channel mechanism is energetically favoured, whereas for the analogue low spin (LS) $[\text{FeO}(\text{NH}_3)_4(\text{H}_2\text{O})]^{2+}$ species, the π -channel mechanism is preferred, where the $\pi^*(\text{Fe-}3d_{x/y}\text{-O-}2p_{x/y})$ of the FeO^{2+} participates. The presence of the stronger-field NH_3 ligands in the $[\text{FeO}(\text{NH}_3)_4(\text{H}_2\text{O})]^{2+}$ species results in a low-spin ground state and effectively destabilizes or “pushes up” the LUMO $d_{x^2-y^2}$ as well as the higher-lying $\sigma^*(\text{Fe-}3d_{z^2}\text{-O-}p_z)$, resulting in a $\pi^*(\text{Fe-}3d_{xz/yz}\text{-O-}2p_{x/y})$ energetically more favourable for the electrophilic attack.

The $\sigma^*(\alpha)$ orbital is parallel to the Fe-O bond, and thus, in the transition state for maximal overlap, the Fe, O, and H atoms are aligned. In contrast, the electron-accepting orbital $\pi^*_{x/y}(\beta)$ (LUMO in the LS $[\text{FeO}(\text{NH}_3)_4(\text{H}_2\text{O})]^{2+}$) is perpendicular to the Fe-O bond, and therefore, the forming O-H bond is not aligned with the Fe-O bond in the transition state. Not surprising, the activation via the σ -channel mechanism for both HS complexes, $[\text{FeO}(\text{H}_2\text{O})_5]^{2+}$ and $[\text{FeO}(\text{NH}_3)_4(\text{H}_2\text{O})]^{2+}$, proceeds with much lower barriers than via the π -channel. Nevertheless, for $[\text{FeO}(\text{NH}_3)_4(\text{H}_2\text{O})]^{2+}$, the ground state is the LS, and the preferred mechanism becomes the π -channel.

The groups of He, Neese, and Solomon have put forward an alternative proposal, where radical-anion character was postulated to stem from the reactive oxygen ligand and to be key for the efficient HAA for methane (Figure 1.6) [35, 38–40].

This mechanistic concept has been supported by DFT studies on C-H activation

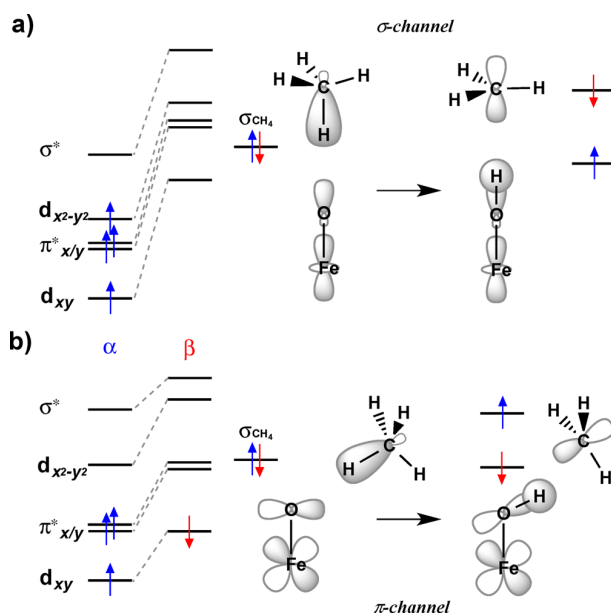


Figure 1.5: Frontier Kohn-Sham orbitals of (a) high spin $[\text{FeO}(\text{H}_2\text{O})_5]^{2+}$ $S=2$ and (b) low spin $[\text{FeO}(\text{NH}_3)_4(\text{H}_2\text{O})]^{2+}$ $S=1$ and the schematic representation of the electron-accepting molecular orbital. The α spin orbitals are to the left and the β spin orbitals to the right.

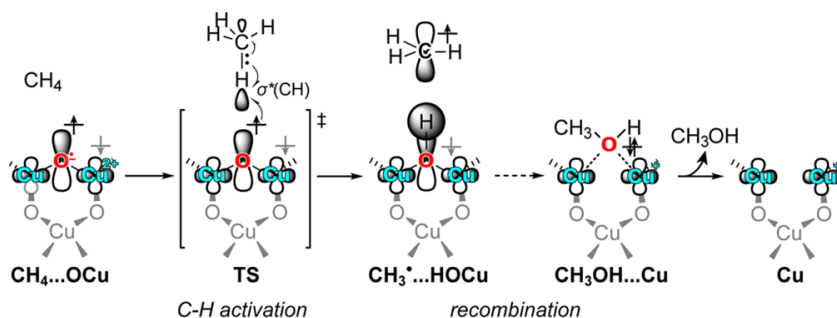


Figure 1.6: Schematic representation of orbital interactions involved in C-H bond activation by the reactive O^* radical in Cu-oxo clusters.[41]

by various metal-oxo clusters, including a promising heterogeneous methane oxo-functionalization system based on Cu-containing high-silica zeolite catalytic system (Figure 1.6) [40]. In a theoretical study, He *et al.* revealed a correlation between the spin density on the reactive oxygen centre of small metal-oxo clusters and the barrier of C-H bond activation [39]. Despite these leads, the role of the putative oxygen radical anion in the C-H bond activation mechanism is still under debate [37]. Additional advanced theoretical analysis of the orbital interaction mechanism is necessary for the $\text{Fe}=\text{O}^{2+}$ core as well as for other metal-mediated HAA systems.

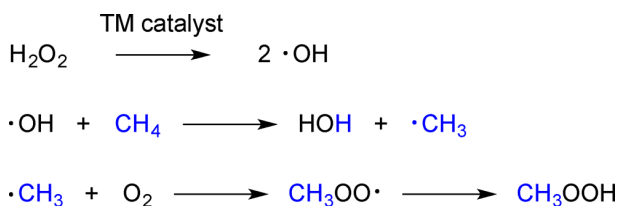


Figure 1.7: Simplified equations of the Fenton-type reaction mechanism

Fenton-type mechanism occurs when neither the metal nor its ligands are directly involved in the C-H bond activation. It is activated by free radicals (see Figure 1.7). A representative example can be found in the works of Shulpin *et al.* [42–44], who applied transition-metal complexes as catalysts for the oxidation of methane as well as other alkanes. In these reactions, the oxidant source is H_2O_2 or O_2 , and the metal facilitates the radical decomposition of H_2O_2 to form reactive species capable of hydrogen abstraction from alkanes. In such radical chain mechanism, the activation of methane by the OH radical is highly exothermic ($\Delta H \cong -60$ kJ/mol) and proceeds with a barrier of only 15 kJ/mol to form a methyl radical and water [45].

1.2.2. ACTIVATION OF THE OXIDANT AS A KEY STEP IN OXIDATIVE DIRECT FUNCTIONALIZATION ROUTES

After the C-H cleavage step, the activation of the oxidant to form and regenerate an appropriate reactive site is crucial. The main difficulty of applying O_2 directly for the selective oxidation of hydrocarbons is associated with the triplet ground state of the oxygen molecule. Wiegner's selection rule states that the multiplicity (M) of the system has to be preserved in the course of a chemical reaction. This implies that the reaction between a substrate with a singlet (CH_4 , $M = 0$) and a substrate with a triplet (O_2 , $M = 1$) electron configuration to form products in the singlet state (CH_3OH and H_2O , $M = 0$) is not allowed.

Such a spin-forbidden process can only take place when a hydrocarbon reacts with O_2 in one of its singlet-excited states (Figure 1.8) lying 157 ($^1\Sigma_g^+$) and 94 kJ/mol ($^1\Delta_g$) above the ground state. However, the respective excited-state reaction pathways are usually quite unselective, especially when taking place at elevated temperatures [46].

There are different possibilities to overcome the spin forbidden limitation for oxidation reactions such as excitation to the singlet state ($^1\Delta_g$), autoxidation or, the most important concerning catalysis, the activation of ($^3\Sigma_g^-$) O_2 by the aid of a metal centre.

In total 4 electrons are necessary to reduce the O_2 molecule to two $\text{M}=\text{O}^{2-}$ species. Less than four electron transfer results in partially reduced O species. Both species can be active in C-H bond activation. In the soluble methane monooxygenase enzymes

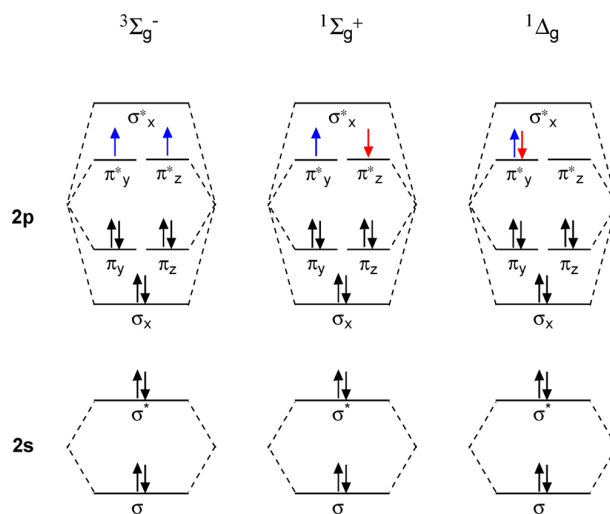


Figure 1.8: Molecular orbital diagram of molecular oxygen in (a) triplet ground state ($^3\Sigma_g^-$), (b) singlet excited state with electrons on different orbitals ($^1\Sigma_g^+$), and (c) singlet excited state with electrons on the same orbitals ($^1\Delta_g$.)

(sMMO), the reduced metal at the active site donates four electrons to the adsorbed O_2 molecule, resulting in its complete reduction to O^{2-} species, which in turn acts as proton-accepting site upon C-H bond activation [47]. However, to establish a true catalytic cycle (i.e., to promote the formation of the oxidation products and the regeneration of the initial active site), the assistance from other components of the enzymatic system is required. These include the cooperation of the metal active centre with functional groups at the protein matrix and/or reactions with cofactors such as NAD(P)H and FADH₂.

This insight into the oxidation processes in biological systems has inspired chemists to construct synthetic schemes following the enzymatic approach but using alternative lower-cost stoichiometric reducing agents to replace NAD(P)H [48]. The generation of electrons and protons within the catalytic cycle can be accomplished by using a combination of iron or zinc powder with carboxylic acids in the well-studied Gif systems [49]. Ultimately, the use of molecular H_2 as the stoichiometric reducing agent is desired. Such a selective oxidation one-pot system has been reported by Otsuka and co-workers [20].

An alternative catalyst design involves the spatial separation of the substrate oxidation and the active-site regeneration steps. The selective oxidation reaction in such a scheme requires the use of preformed reactive oxygen species, which after the completion of the oxidation step has to be separately regenerated. Most commonly, H_2O_2 , O_3 , N_2O , and tert-butyl hydroperoxide are used as reactive oxygen donors in these

schemes. However, other substances like HNO_3 , H_2SO_4 , NaClO , and NaClO_2 have also been applied [46].

A very important and well-known example of this class of selective oxidation systems is the homogeneous Periana “Catalytica” system. On the basis of the studies of electrophilic reactions with alkenes from Shilov [33], Bercaw, and Labinger [50], Periana first employed Hg^{II} as a soft powerful electrophile able to oxidise methane to methyl bisulfate in concentrated sulphuric acid [51]. Although it was a huge step forward, using Hg has the disadvantage that this metal cannot be easily modified by ligands. Thus, the effort was focused on stabilizing Pt species through different ligands in concentrated sulphuric acid. Few ligands withstand the oxidizing and acidic conditions, and remarkably, 2,2'-dipyrimidine binds Pt so effectively that it not only survives the reaction media but also stabilizes Pt^{II} and avoids oxidation to Pt^{IV} [52]. In both cases, the selectivity is remarkably only toward methane because the oxidized product is protected by the bisulfate. It was found that weakly basic counter-anions facilitate the reaction and that electron-deficient C-H bonds are less likely to react. In this system, H_2SO_4 is used as the oxidant but is also the key to stabilize the metal centre. Upon reaction with methane, H_2SO_4 is reduced to SO_2 and has to be separately reoxidized to regenerate sulphuric acid (Figure 1.9).

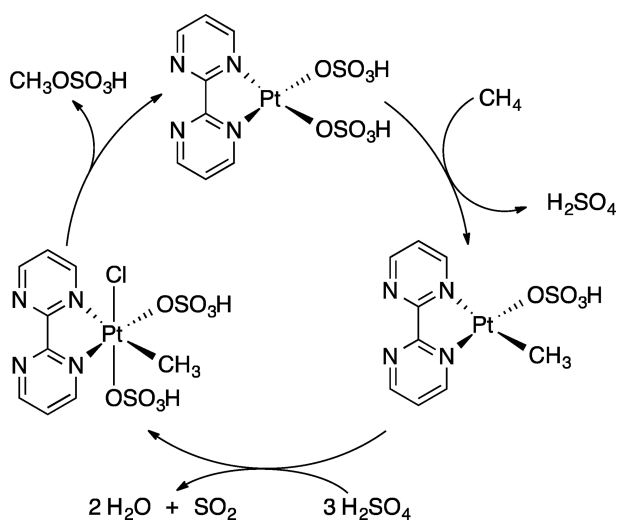


Figure 1.9: Pt-based Catalytica system with sulphuric acid to help to close the catalytic cycle.

The use of H_2O_2 as the oxidant conceptually bridges the above-mentioned approaches. On one hand, the possibility to directly synthesize hydrogen peroxide through a low-temperature catalytic oxidation of H_2 [53, 54] renders the latter as

the O₂ shuttle that can be used to establish a truly catalytic system for the selective oxidation of methane to methanol [55–57]. In spite of its environmental attractiveness, the industrial applicability of H₂O₂ for methane oxo-functionalization is still limited mainly because of the relatively high price of the oxidant compared to that of the target product. Nevertheless, from the academic perspective, the use of H₂O₂ as well as other alternative oxidants [58–60] can provide crucial mechanistic insights into the different steps of the methane oxidation reaction.

To summarize the above mechanistic considerations, it is clear that whereas a wide variety of systems can promote the C-H bond activation, the formation of the active sites and their regeneration within a single catalytic process using molecular O₂ as the oxidant represent the key challenge toward a practical direct route, specially when mild reaction conditions are desired. All the successful catalyst systems employ in one way or another O₂ shuttle strategies, in which the C-H bond and O₂ activation steps are mechanistically separated. Interestingly, nature does not provide exception to this rule. It also does not use directly O₂ as the actual oxidant for methane activation, but it employs more complicated multistep schemes involving the use of stoichiometric reductants to form and regenerate the active sites within the catalytic cycles.

1.3. PROGRESS IN METHANE CONVERSION TO METHANOL

THERMAL oxidation of methane is the simplest alternative to the current two-step process [61]. Relatively high yields of oxygenated products can be achieved. 60% methanol selectivity at 12–13% methane conversion has been reported. Interestingly, it was proposed that the metal wall of the actual reactor is key to the low selectivity of the process as it provides catalytic sites for the overoxidation of methanol to carbon oxides. Although the methanol yields achieved by the thermal oxidation are quite impressive, it was concluded that no further improvement of the process could be delivered by the optimization of the operational conditions. The introduction of a catalyst capable of shifting the selectivity away from the overoxidation path is necessary [9].

Although most of the published literature on heterogeneous catalysis for low-temperature activation of methane are still fundamental studies, these selected examples clearly make use of the knowledge gained over the last few decades on the different activation strategies discussed above. The case of zeolite catalysis mimicking enzymes is an outstanding example.

Most often zeolites incorporate Cu-oxo [62, 63] and/or Fe-oxo [57, 64, 65] species within extra-framework positions, but other transition and non-transition metals,

such as Co [66], Ni [67] and Zn [68, 69] were also reported to activate methane [55, 58, 70, 71]. In general, regeneration of the active site seems to be the most obvious problem, and because of this reason, different oxidants and protocols for methanol desorption have been proposed. The first reports are on Fe-ZSM-5 catalysts activated with N_2O [58, 70] as an oxidant. N_2O oxidises the Fe^{II} species to an Fe^{IV} -oxo cluster, which is able to homolytically cleave the C-H bond of methane. Unfortunately, the formed methanol is strongly bonded to the active site and has to be extracted with water or an aqueous solution of acetonitrile. Gao *et al.* have shown the key role of N_2O as oxidant on Fe-ZSM-5 as the activation with molecular oxygen solely produced full combustion products (i.e., carbon dioxide and water) [72].

The first application of a Cu-loaded zeolite for the partial oxidation of methane was described by Groothaert *et al.* [62]. In this case, the Cu-catalyst activation with molecular oxygen was successful for the selective conversion of methane to methanol. As in Fe-ZSM-5, methanol is strongly bonded to the zeolite, and it has to be extracted with a 1:1 water:acetonitrile mixture. The study was extended to other zeolite frameworks and Cu-MOR showed even higher methanol yields. The nuclearity of the *active* Cu clusters are still debated. An UV-Vis band was identified that is correlated with binuclear Cu-oxo clusters in Fe-ZSM-5 and MOR [62, 73]. The existence of other active Cu-oxo species was further demonstrated by Lercher *et al.* with the synthesis of well-defined trinuclear clusters anchored in two framework Al sites of a zeolite H-MOR [74]. Remarkably, this Cu-zeolite system yields an order of magnitude more methanol than previously reported binuclear Cu-oxo clusters in Cu-ZSM-5.

Other zeolite structures, such as Cu-Beta, Cu-ferrierite [75], Cu-SSZ-13, Cu-SSZ-16, Cu-SSZ-39 and SAPO-34 [76] were found to be active in methane conversion.

The greatest problem of the gas-solid phase reactions is that they are semi-catalytic. Catalyst oxidation, methane activation and methanol formation by hydrolysis of the strongly adsorbed methoxo species are carried out in separate process stages. Additionally the product is obtained as a very low-concentration solution which entails further costs of separation. Recently promising improvements were achieved by the co-feeding of water in the reaction mixture [77].

The use of other oxidants in the liquid phase was explored by Hammond *et al.* [55–57, 78, 79]. Cu containing Fe-ZSM-5 was able to convert methane into methanol in a single step and in the liquid phase by using hydrogen peroxide as oxidant. The nature of the Fe species was investigated by IR and UV-vis spectroscopy. These spectroscopic techniques reveal that after synthesis, Fe was tetrahedrally coordinated in the zeolite framework. The subsequent removal of the template and calcination result in the

migration of the iron species to extra-framework positions. This was also demonstrated by XANES spectroscopy, which shows an increase in Fe species in octahedral coordination upon calcination. Combining EXAFS spectroscopy and DFT calculations unravels the nature of Fe as binuclear Fe complexes containing octahedral Fe³⁺. They also found that the addition of Cu does not activate methane but facilitates the formation of methanol by suppressing the non-selective methane oxidation to formic acid and CO₂. Subsequently, Hammond *et al.* report the promoting effect of Al³⁺ and Ga³⁺, which facilitate the extraction of Fe³⁺ ions to octahedral positions and stabilize these extra-framework active iron species. Further insight into the nature of the iron active species provided by resonance-enhanced Raman spectroscopy directly correlated a band at 521 cm⁻¹ with the Fe-ZSM-5 catalytic activity. The results, in combination with the previous EXAFS spectroscopy and DFT calculations, indicate that this band is an Fe-O(H)-Fe stretching vibration.

The main limitations of transition metal-containing zeolite-based catalysts is the limited number of practical topologies suitable for acting as the stabilizing microporous matrices and the extra-framework nature of the deposited catalytic metal species [80]. The latter factor inevitably causes a heterogeneous metal speciation in practical catalysts [81–83] and the inherent flexibility of the coordination environment as the metal centres are bound to rather weak donor sites of the aluminosilicate zeolite lattice. Whereas the formation of well-defined metal species in zeolite pores can potentially be achieved through the optimization of the synthetic approaches [41, 74], the coordination flexibility of the intra-zeolite complexes is the inherent property. In the context of methane oxidation catalysis, both these factors may contribute to the decreased selectivity of the overall reaction. In this regard, other structured materials such as polyaromatic frameworks or metal organic frameworks may offer design advantages over zeolites for the low temperature activation of methane.

In a seminal work, Palkovits and colleagues [84] demonstrated the potential of covalent triazine frameworks (CTFs) [85], a porous type of organic polymer synthesized from cheap feedstock, for the immobilization of Periana type catalysts. After synthesis, CTFs contain quasi bipyridine moieties that can be used to directly immobilize Pt [86]. Under Periana conditions, the performance of the resulting catalysts is one of the most promising ever published for an heterogeneous catalyst.

A promising alternative to the conventional pure inorganic zeolite-based catalysts are hybrid metal-organic frameworks (MOF) that are crystalline porous materials, which structures are made of metal ions or clusters connected by organic linkers [87]. The well-defined nature of the inorganic nodes and their established coordination

chemistry together with the great versatility of the organic linkers allow to tailor the structural, electronic and catalytic properties of MOFs towards a specific application [88–95].

Lercher [96] *et al.* have described a Zr-based MOF, NU-1000 containing copper oxide cluster synthesized via atomic layer deposition that is active for the selective oxidation of methane with O₂ under mild reaction conditions. Very recently, we reported that the introduction of isolated Fe species into the well-defined inorganic structure of an Al-terephthalate-based MOF gives rise to a MIL-53(Fe,Al) mixed-metal catalyst showing a high activity and selectivity in the oxidation of methane to methanol with H₂O₂ [97]. The parent MIL-53(Al) microporous MOF matrix is made up of [AlO₆] octahedral chains connected by 1,4-benzodicarboxylic acid struts to form well-defined 1D channels (Figure 3.1). The catalytic function can be introduced to this material by creating well-dispersed Fe sites inside these inorganic structure-forming chains. The extensive characterization of the catalysts revealed the predominant speciation of the reactive Fe as dimeric (Fe₂-MIL-53(Al)) and monomeric (Fe₁-MIL-53(Al)) complexes isomorphously substituting Al ions in the MIL-53 crystalline lattice. Such Fe sites are placed in a unique octahedral weak ligand field environment that is expected to be favourable for the C-H bond activation in methane [36, 37]. The isolated nature of the Fe sites in MIL-53(Fe,Al) is crucial for the structural stability of the material towards the oxidizing aqueous environment of the catalytic reaction.

1.4. COMPUTATIONAL METHODS

UNDERSTANDING the nature of the catalytic species and reaction mechanism is key to the rational optimization and improvement of heterogeneous catalysts. Extra-framework clusters present in metal-exchanged zeolites can have different chemical composition and be located at different positions. Distinct configurations and clusters might have different catalytic activity and contribute differently to the overall selectivity of the catalytic process [41, 98–102]. That is why a great deal of research studies has so far been devoted to discriminating the active site from the spectator species and the identification of the reaction mechanism in zeolite catalysis.

Computational chemistry enables us to study our system at an atomistic level that is not possible with any experimental tool at our disposal at the moment. In the past decades it evolved to be one of the most important tools in catalysis next to other techniques like infrared spectroscopy, nuclear magnetic resonance spectroscopy or X-ray diffraction. Atomic level simulations play an important role in understanding catalytic processes [103–107]. Advanced, user-friendly quantum chemical software enable scientists to set up calculations and draw meaningful conclusions without

deep knowledge of programming and underlying theory of quantum mechanics. Particularly DFT is well-suited in studying catalytic systems due its low computational demand vs high accuracy. Accuracy is conventionally referred to how close the computation of some chemical property (most often relative energies of intermediates) is to the experimental results, or calculations of higher level methods. When investigating catalytic, especially heterogeneous, systems, other than the method accuracy (level of the theoretical approximation), the model accuracy (level of chemical details included in the model) also determines the overall accuracy of the calculation [108]. In our case the intrinsic chemistry of 3d transition metals and the heterogeneous catalyst system present a challenge to both accuracies [109].

1.4.1. DENSITY FUNCTIONAL THEORY IN CATALYSIS

Density functional theory within the Kohn-Scham framework is the most applied. The theory assumes an ideal system where electrons do not interact with an electron density that is exactly the same as the electron density of the interacting system. The overall energy functional can be written as following:

$$E[\rho(\mathbf{r})] = T_{ni}[\rho(\mathbf{r})] + V_{ne}[\rho(\mathbf{r})] + V_{ee}[\rho(\mathbf{r})] + \Delta T[\rho(\mathbf{r})] + \Delta V_{ee}[\rho(\mathbf{r})] \quad (1.1)$$

where $T_{ni}[\rho(\mathbf{r})]$ represents the kinetic energy of the non-interacting model, $V_{ne}[\rho(\mathbf{r})]$ the Coulombic term between nuclei and electrons, and $V_{ee}[\rho(\mathbf{r})]$ the classical repulsion term between electrons. $\Delta T[\rho(\mathbf{r})]$ and $\Delta V_{ee}[\rho(\mathbf{r})]$ are correction terms for the kinetic energy and electronic interaction of the non-interacting system. These two are unknown and often lumped together to $E_{xc}[\rho(\mathbf{r})]$ and called exchange-correlation functional.

The exchange-correlation functional is not known, and many attempted to design functionals for DFT to work. The functionals were grouped and the famous "Jacob's ladder of DFT" was created. The functionals are placed on the rungs of the ladder, and as we move upwards on it, higher and higher method accuracy is reached, with on top the unattainable and absolute accuracy. On the lowest ladder are the local density approximation (LDA) functional. This assumes that $E_{xc}[\rho(\mathbf{r})]$ can be obtained solely from the density function. The next level contains the generalised gradient approximation (GGA) functionals (e.g. PBE [110], BLYP [111, 112], BP86[111]) taking into account the gradient of the density, $\nabla\rho(\mathbf{r})$. These are the lowest level functionals suitable to describe chemical transformations. The next level takes into account the second derivative of the density. These functionals are called meta-GGA, and examples are TPSS [113] and M06L [114, 115]. On the next rung sit the hybrid functionals. The exchange term of the energy functional contains terms from the Hartree-Fock

theory. It is a hybrid of the density functional theory and wave function theory. One of the most applied functionals are the hybrid B3LYP [112, 116] functional but also here belong the PBE0[117] and M06 [114, 115] functionals. On the top level, at the door of absolute accuracy are the double-hybrid functionals, like B2-LYP [118].

With the improvement of accuracy the price goes up and it is paid in computational effort. In heterogeneous catalysis, as mentioned before, other than method accuracy, the elaborateness of the model is just as important often making it necessary to include hundreds of atoms in the simulations. On these large models the calculation of many pathways including a lot of transition states is required for meaningful conclusions. This makes the functionals of the higher rungs too expensive to be applied, and scientists are forced to rely on GGA and meta-GGA functionals. This resulted in the development of heavily parametrised functionals where the parameters were fit for the functionals to correctly describe one or another chemical property of certain types of chemical systems, giving the right answers for the wrong reasons [119, 120]. This makes these functionals completely unsuitable to describe systems that they were not designed for. The result is that the calculated properties are dependent on the choice of the functional, making benchmarking essential.

When dealing with 3d transition metal clusters Vogiatzis *et al.* [109] suggests to pay attention to four things: 1) 3d metals are usually open shell systems with potential spin states within a few kJ/mol from each other. They recommend the calculation of the full spectrum of potential spin states. 2) The expectation value of S^2 should be checked. If it is more than 0.2, than the wave function is spin contaminated and the results should be treated with caution. 3) DFT has trouble dealing with antiferromagnetically coupled systems often converging to the higher energy closed shell configuration. Broken symmetry calculations are recommended to be performed in this case. 4) After geometry optimisation frequency calculations should be performed to be certain that the system is in a local minimum and not in a saddle point.

The exchange correlation functionals also have trouble accounting for the long-range non-covalent interactions. This can significantly influence the adsorption and desorption energies of heterogeneous catalysis, but also the reaction energies and barriers in porous frameworks. One of the most popular methods to account for this deficiency was developed by Grimme *et al.* An empirical term is attached to the energy in the calculations. One of the most commonly used version is Grimme's D3 correction [121] with Becke-Johnson damping [122], abbreviated as -D3(BJ).

An adequate choice of the model is important [108]. In the early days of computational chemistry zeolite models were limited to a few atoms of the framework, the active

site and the reactants. These models completely omit the secondary effects of the framework, that, as we will see in Chapter 4, are sometimes overruling the intrinsic chemistry of the reactants with the active site. The rapid development of computational capacity enabled the usage of bigger clusters or study whole unit cells within the periodic boundary conditions. In the latter case it is not necessary to abruptly terminate the extended structure, and the secondary effects of the framework can be better accounted for. This increased model accuracy comes with a price though. The unit cell of extended frameworks often contain hundreds of atoms, limiting the choices of functionals to GGA and meta-GGA methods.

In this thesis we primarily used the PBE GGA functional with Grimme's D3(BJ) correction. This functional was previously successfully applied in zeolite chemistry, and the size of the model and the amount of potential pathways would not allow for much more computational intensive functional. The exception is the last chapter, when single point calculations on a cluster models are presented and the performance of different functionals is tested.

1.4.2. COMPLETE ACTIVE SPACE SELF-CONSISTENT FIELD METHOD

KS-DFT, similarly to the HF method is a single-reference method. The wave function is expressed as a single Slater determinant (eq. 1.2).

$$\Psi_{SD} = \frac{1}{\sqrt{N!}} \begin{vmatrix} \psi_1(1)\alpha(1) & \psi_1(1)\beta(1) & \psi_2(1)\alpha(1) & \cdots & \psi_{N/2}(1)\alpha(1) & \psi_{N/2}(1)\beta(1) \\ \psi_1(2)\alpha(2) & \psi_1(2)\beta(2) & \psi_2(2)\alpha(2) & \cdots & \psi_{N/2}(2)\alpha(2) & \psi_{N/2}(2)\beta(2) \\ \vdots & \vdots & \vdots & \ddots & \vdots & \vdots \\ \psi_1(N)\alpha(N) & \psi_1(N)\beta(N) & \psi_2(N)\alpha(N) & \cdots & \psi_{N/2}(N)\alpha(N) & \psi_{N/2}(N)\beta(N) \end{vmatrix} \quad (1.2)$$

Where N is the number of electrons that occupy N spin orbitals $\psi_a(i)\sigma(i)$, $\sigma = \alpha$ or β .

These methods give qualitatively correct results for closed-shell molecules, and unrestricted HF and DFT calculations can describe many open-shell systems, including transition metal clusters, correctly. However one must be cautious, because in the case of near-degenerate orbitals, typical for TM clusters, often multireference methods are required for the correct electronic description [123]. In these cases KS-DFT does not stand a chance. Sometimes correct relative energies can be obtained from KS-DFT calculations with a fitted functional, however the results are based on error cancellation and as the electronic configuration of the species are not correct, it does not provide insight to the chemistry, denying us the power of prediction.

The basis of multireference or multiconfigurational calculations is a single reference wave function. The wave function (Ψ_{MC}) can be obtained according to equation 1.3 as weighted sum of single determinants, also called configuration state functions (CSFs).

$$\Psi_{MC} = \sum_n c_n \Psi_n \quad (1.3)$$

where c_n are parameters determined variationally, and Ψ_n are the CSFs. The CSFs are created by arranging the electrons on the orbitals in different configurations. This is the basis of configurational interaction (CI) theory and multireference self-consistent field method [124]. In CI theory the c_n coefficients optimised. When all possible configuration of a full SD wave function is used, we are talking about a full CI. When full CI is used with an infinite basis set, it provides the exact Born-Oppenheimer non-relativistic electronic energy in the absence of an external field. The full CI calculation is computationally extremely demanding even for small molecules, therefore a truncated wave function is created, where not all possible CSFs are considered.

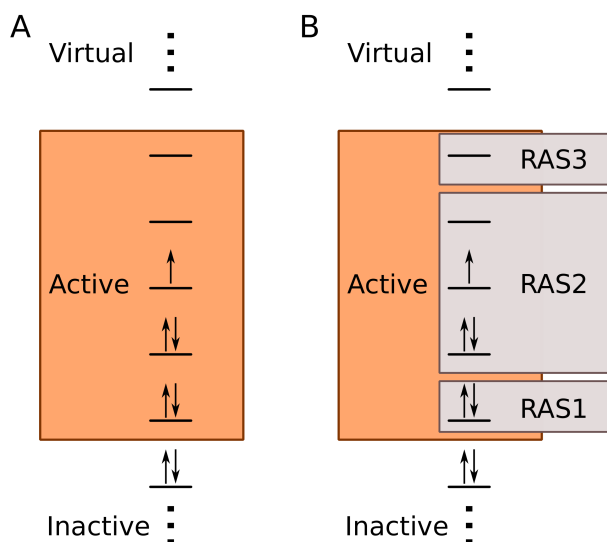


Figure 1.10: Schematic representation of the molecular orbital subspaces defined for (a) CASSCF and (b) RASSCF calculations. Inactive and virtual orbitals remain doubly occupied and unoccupied, respectively, and they do not participate in the formation of the multiconfigurational wave function. A CI expansion is formed from the orbitals in the active space. In the RAS scheme, the active space is divided into three subspaces (RAS1, RAS2, and RAS3) and a constrained CI expansion is formed.

If in addition to the CI coefficients the molecular orbital coefficients are also optimised we talk about multiconfigurational self-consistent-field (MCSCF) theory. The most widely applied MCSCF method is the complete active space SCF (CASSCF) method. During the CASSCF calculations at first usually a Hartree-Fock calculation is performed to obtain the reference wave function. In the next step the orbitals are categorised into doubly occupied, active and empty or virtual orbitals (Figure 1.10A).

CAS(n,m) denotes to n active space with n electrons on m active orbitals. After this, a full CI is created within the active space. In the next step the multireference calculation is performed, during which the CI and orbitals coefficients are optimised.

The size of the CI expansion, and therefore the computation costs of the calculations scales exponentially with the size of the active space, therefore, just like for the CI calculations, the choice of the active orbitals has to be carefully considered. Currently the limit of the active space for single-point calculations is around (16,16). Alternative methods were developed to mitigate the problem. One example is the restricted active space (RAS) method [125] (Figure 1.10B), which further divides the active space to two more spaces: RAS1, RAS2 and RAS3. In RAS2 there is a full CI expansion is created, just like in the case of CASSCF. RAS1 space contains doubly occupied orbitals, while RAS3 space contains empty orbitals. The excitation of a limited number of electrons between the three spaces is possible. This restricts the number of possible configurations making larger calculations feasible. Another example is density matrix renormalization group complete active space self-consistent field (DMRG-CASSCF) method [126]. DMRG allows the use of a large-size active space in multireference calculations, which makes it possible to handle an active space as large as 100 electrons on 100 orbitals. These methods are not black-box, as users are required to define the size of the active space, which is based on chemical considerations. This lead to a bias in the calculations based on the researcher.

A significant limitation of the CASSCF theory is that it lacks dynamic correlation. Most often an other calculation based on perturbation theory follows the CASSCF calculation (CASPT2) [127].

1.5. SCOPE OF THE THESIS

THE aim of this thesis is to develop a deeper understanding of the mechanism of selective methane oxidation over binuclear Fe sites in porous frameworks. Particular emphasis is laid on the effects influencing the reaction other than the intrinsic chemistry of the C-H bond activation including secondary effects provided by the zeolite and the overoxidation of methanol.

Chapter 2 presents a systematic DFT study of the reaction of a binuclear Fe-oxo cluster deposited in ZSM-5 zeolite framework with H_2O_2 and CH_4 . It presents diverse pathways to the formation of different active sites that promote the first C-H bond dissociation of methane. This second step is extensively analysed, finally the formation of methanol and the regeneration of the pre-active site is presented.

Chapter 3 is a study presenting the oxidation of methane with H_2O_2 over a binuclear Fe-oxo cluster, similar to that of Chapter 2 in MIL-53 metal organic framework. Calculations were performed to investigate the overoxidation of methane to CO_2 and compared with experimental results. The mechanism of methyl-hydroperoxide formation and H_2O_2 decomposition was investigated. Additionally calculations with mononuclear Fe site were performed and the effect of the nuclearity on the reaction was investigated.

Chapter 4 investigates the effect of confined environment on the C-H bond activation of the system described in Chapter 2. Binuclear Fe-oxo clusters are placed in different places of the ZSM-5 zeolite representing different confinement environments. Several external effects influencing the C-H bond dissociation of methane is identified with the help of structure-activity relationships.

Chapter 5 discusses the applicability of DFT on the reaction of methane with binuclear Fe-oxo clusters. Single point calculations are performed on mechanistically different types of reaction intermediates with several DFT functionals and the CASSCF/CASPT2 multiconfigurational method. The wave function, the spin ladder and the relative energies of the intermediates obtained by the MC method were carefully analysed and compared with the results obtained by DFT.

REFERENCES

- [1] G. A. Olah, *Angew. Chem. Int. Ed.*, 2005, **44**, 2636–2639.
- [2] A. Hoek and L. B. J. M. Kersten, *The Shell Middle Distillate Synthesis Process: Technology, products and perspective*, 2004, vol. 147, pp. 25–30.
- [3] C. Hammond, S. Conrad and I. Hermans, *ChemSusChem*, 2012, **5**, 1668–1686.
- [4] J. M. Fox, *Catal. Rev.*, 1993, **35**, 169–212.
- [5] N. D. Parkyns, C. I. Warburton and J. D. Wilson, *Catal. Today*, 1993, **18**, 385–442.
- [6] K. Aasberg-Petersen, I. Dybkjær, C. V. Ovesen, N. C. Schjødt, J. Sehested and S. G. Thomsen, *J. Nat. Gas Sci. Eng.*, 2011, **3**, 423–459.
- [7] B. A. Arndtsen, R. G. Bergman, T. A. Mobley and T. H. Peterson, *Acc. Chem. Res.*, 1995, **28**, 154–162.
- [8] R. G. Bergman, *Nature*, 2007, **446**, 391–393.
- [9] Q. Zhang, D. He and Q. Zhu, *J. Nat. Gas Chem.*, 2003, **12**, 81–89.
- [10] C. K. Rofer-DePorter, *Chem. Rev.*, 1981, **81**, 447–474.
- [11] M. Appl, *Ullmann's Encyclopedia of Industrial Chemistry*, Wiley-VCH Verlag GmbH & Co. KGaA, Weinheim, 2000, vol. 3, pp. 139–225.
- [12] R. Franke, D. Selent and A. Börner, *Chem. Rev.*, 2012, **112**, 5675–5732.
- [13] R. Reimert, F. Marschner, H.-J. Renner, W. Boll, E. Supp, M. Brejc, W. Liebner and G. Schaub, *Ullmann's Encyclopedia of Industrial Chemistry*, Wiley-VCH Verlag GmbH & Co. KGaA, Weinheim, 2000, vol. 16, pp. 423–482.
- [14] V. Havran, M. P. Duduković and C. S. Lo, *Ind. Eng. Chem. Res.*, 2011, **50**, 7089–7100.
- [15] G. Jones, J. G. Jakobsen, S. S. Shim, J. Kleis, M. P. Andersson, J. Rossmeis, F. Abild-Pedersen, T. Bligaard, S. Helveg, B. Hinnemann, J. R. Rostrup-Nielsen, I. Chorkendorff, J. Sehested and J. K. Nørskov, *J. Catal.*, 2008, **259**, 147–160.
- [16] J. H. Edwards and A. M. Maitra, *Fuel Process. Technol.*, 1995, **42**, 269–289.
- [17] T. V. Choudhary and V. R. Choudhary, *Angew. Chem. Int. Ed.*, 2008, **47**, 1828–1847.
- [18] W. P. Jones and R. P. Lindstedt, *Combust. Flame*, 1988, **73**, 233–249.
- [19] A. Holmen, *Catal. Today*, 2009, **142**, 2–8.
- [20] K. Otsuka and Y. Wang, *Appl. Catal., A*, 2001, **222**, 145–161.
- [21] P. Khirsariya and R. K. Mewada, *Procedia Engineering*, 2013, pp. 409–415.
- [22] H. D. Gesser, N. R. Hunter and C. B. Prakash, *Chem. Rev.*, 1985, **85**, 235–244.
- [23] J. H. Lunsford, *Catal. Today*, 2000, **63**, 165–174.
- [24] A. Cherkasov and M. Jonsson, *J. Chem. Inf. Comput. Sci.*, 2000, **40**, 1222–1226.

- [25] A. E. Shilov and G. B. Shul'pin, *Chem. Rev.*, 1997, **97**, 2879–2932.
- [26] C. Copéret, *Chem. Rev.*, 2010, **110**, 656–680.
- [27] D. H. Ess, R. J. Nielsen, W. A. Goddard III and R. A. Periana, *J. Am. Chem. Soc.*, 2009, **131**, 11686–11688.
- [28] D. H. Ess, W. A. Goddard and R. A. Periana, *Organometallics*, 2010, **29**, 6459–6472.
- [29] B. A. Vastine and M. B. Hall, *J. Am. Chem. Soc.*, 2007, **129**, 12068–12069.
- [30] K. Kwapien, J. Paier, J. Sauer, M. Geske, U. Zavyalova, R. Horn, P. Schwach, A. Trunschke and R. Schlögl, *Angew. Chem. Int. Ed.*, 2014, **53**, 8774–8778.
- [31] A. Caballero and P. J. Pérez, *Chem. Soc. Rev.*, 2013, **42**, 8809–8820.
- [32] J. Saillard and R. Hoffmann, *J. Am. Chem. Soc.*, 1984, **106**, 2006–2026.
- [33] A. E. Shilov and A. A. Shteinman, *Coord. Chem. Rev.*, 1977, **24**, 97–143.
- [34] J. M. Mayer, *Acc. Chem. Res.*, 2011, **44**, 36–46.
- [35] C. Geng, S. Ye and F. Neese, *Angew. Chem. Int. Ed.*, 2010, **49**, 5717–5720.
- [36] G. Gopakumar, P. Belanzoni and E. Baerends, *Inorg. Chem.*, 2012, **51**, 63–75.
- [37] A. Kazaryan and E. Baerends, *ACS Catal.*, 2015, **5**, 1475–1488.
- [38] S. Ye and F. Neese, *Proc. Natl. Acad. Sci. U.S.A.*, 2011, **108**, 1228–1233.
- [39] X. Ding, X. Wu, Y. Zhao and S. He, *Acc. Chem. Res.*, 2012, **45**, 382–390.
- [40] M. Srnec, S. D. Wong, J. England, L. Que Jr. and E. I. Solomon, *Proc. Natl. Acad. Sci. U.S.A.*, 2012, **109**, 14326–14331.
- [41] G. Li, P. Vassilev, M. Sanchez-Sanchez, J. Lercher, E. J. M. Hensen and E. A. Pidko, *J. Catal.*, 2016, **338**, 305–312.
- [42] G. V. Nizova, G. Süß-Fink and G. B. Shul'pin, *Chem. Commun.*, 1997, 397–398.
- [43] G. B. Shulpin and G. V. Nizova, *React. Kinet. Catal. Lett.*, 1992, **48**, 333–338.
- [44] G. Süß-Fink, G. V. Nizova, S. Stanislas and G. B. Shul'Pin, *J. Mol. Catal. A Chem.*, 1998, **130**, 163–170.
- [45] J. J. Margitan, F. Kaufman and J. G. Anderson, *Geophys. Res. Lett.*, 1974, **1**, 80–81.
- [46] X. Liu, Y. Ryabenkova and M. Conte, *Phys. Chem. Chem. Phys.*, 2015, **17**, 715–731.
- [47] R. Banerjee, Y. Proshlyakov, J. D. Lipscomb and D. A. Proshlyakov, *Nature*, 2015, **518**, 431–434.
- [48] S. Friedle, E. Reisner and S. J. Lippard, *Chem. Soc. Rev.*, 2010, **39**, 2768–2779.
- [49] H. R. B. Derek and D. Doller, *Acc. Chem. Res.*, 1992, **25**, 504–512.
- [50] S. S. Stahl, J. A. Labinger and J. E. Bercaw, *Angew. Chem. Int. Ed.*, 1998, **37**, 2180–2192.
- [51] R. Periana, D. Taube, E. Evitt, D. Löffler, P. Wentreck, G. Voss and T. Masuda, *Science*, 1993, **259**, 340–343.

- [52] R. Periana, D. Taube, S. Gamble, H. Taube, T. Satoh and H. Fujii, *Science*, 1998, **280**, 560–564.
- [53] J. K. Edwards, B. Solsona, E. Ntainjua N, A. F. Carley, A. A. Herzing, C. J. Kiely and G. J. Hutchings, *Science*, 2009, **323**, 1037–1041.
- [54] I. Moreno, N. F. Dummer, J. K. Edwards, M. Alhumaimess, M. Sankar, R. Sanz, P. Pizarro, D. P. Serrano and G. J. Hutchings, *Catal. Sci. Technol.*, 2013, **3**, 2425–2434.
- [55] C. Hammond, M. M. Forde, M. H. Ab Rahim, A. Thetford, Q. He, R. L. Jenkins, N. Dimitratos, J. A. Lopez-Sanchez, N. F. Dummer, D. M. Murphy, A. F. Carley, S. H. Taylor, D. J. Willock, E. E. Stangland, J. Kang, H. Hagen, C. J. Kiely and G. J. Hutchings, *Angew. Chem. Int. Ed.*, 2012, **51**, 5129–5133.
- [56] C. Hammond, R. L. Jenkins, N. Dimitratos, J. A. Lopez-Sanchez, M. H. Ab Rahim, M. M. Forde, A. Thetford, D. M. Murphy, H. Hagen, E. E. Stangland, J. M. Moulijn, S. H. Taylor, D. J. Willock and G. J. Hutchings, *Chem. Eur. J.*, 2012, **18**, 15735–15745.
- [57] C. Hammond, N. Dimitratos, J. A. Lopez-Sanchez, R. L. Jenkins, G. Whiting, S. A. Kondrat, M. H. Ab Rahim, M. M. Forde, A. Thetford, H. Hagen, E. E. Stangland, J. M. Moulijn, S. H. Taylor, D. J. Willock and G. J. Hutchings, *ACS Catal.*, 2013, **3**, 1835–1844.
- [58] M. V. Parfenov, E. V. Starokon, L. V. Pirutko and G. I. Panov, *J. Catal.*, 2014, **318**, 14–21.
- [59] P. P. Knops-Gerrits and W. A. Goddard III, *J. Mol. Catal. A: Chem.*, 2001, **166**, 135–145.
- [60] D. J. Xiao, E. D. Bloch, J. A. Mason, W. L. Queen, M. R. Hudson, N. Planas, J. Borycz, A. L. Dzubak, P. Verma, K. Lee, F. Bonino, V. Crocellà, J. Yano, S. Bordiga, D. G. Truhlar, L. Gagliardi, C. M. Brown and J. R. Long, *Nature Chem.*, 2014, **6**, 590–595.
- [61] W. A. Bone and R. V. Wheeler, *J. Chem. Soc., Trans.*, 1902, **81**, 535–549.
- [62] M. H. Groothaert, P. J. Smeets, B. F. Sels, P. A. Jacobs and R. A. Schoonheydt, *J. Am. Chem. Soc.*, 2005, **127**, 1394–1395.
- [63] J. S. Woertink, P. J. Smeets, M. H. Groothaert, M. A. Vance, B. F. Sels, R. A. Schoonheydt and E. I. Solomon, *Proc. Natl. Acad. Sci. U. S. A.*, 2009, **106**, 18908–18913.
- [64] K. A. Dubkov, V. I. Sobolev and G. I. Panov, *Kinet. Catal.*, 1998, **39**, 72–79.
- [65] G. I. Panov, V. I. Sobolev, K. A. Dubkov, V. N. Parmon, N. S. Ovanesyan, A. E. Shilov and A. A. Shteinman, *React. Kinet. Catal. Lett.*, 1997, **61**, 251–258.
- [66] N. V. Beznis, B. M. Weckhuysen and J. H. Bitter, *Catal. Lett.*, 2010, **136**, 52–56.
- [67] J. Shan, W. Huang, L. Nguyen, Y. Yu, S. Zhang, Y. Li, A. I. Frenkel and F. Tao, *Langmuir*, 2014, **30**, 8558–8569.
- [68] J. Xu, A. Zheng, X. Wang, G. Qi, J. Su, J. Du, Z. Gan, J. Wu, W. Wang and F. Deng, *Chem. Sci.*, 2012, **3**, 2932–2940.
- [69] A. Oda, H. Torigoe, A. Itadani, T. Ohkubo, T. Yumura, H. Kobayashi and Y. Kuroda, *J. Phys. Chem. C*, 2013, **117**, 19525–19534.
- [70] V. I. Sobolev, K. A. Dubkov, O. V. Panna and G. I. Panov, *Catal. Today*, 1995, **24**, 251–252.

- [71] A. R. Kulkarni, Z.-J. Zhao, S. Siahrostami, J. K. Nørskov and F. Studt, *Catal. Sci. Technol.*, 2018, **8**, 114–123.
- [72] Z. Gao, H. Kim, Q. Sun, P. C. Stair and W. M. H. Sachtler, *J. Phys. Chem. B*, 2001, **105**, 6186–6190.
- [73] E. M. Alayon, M. Nachtegaal, M. Ranocchiari and J. A. Van Bokhoven, *Chem. Commun.*, 2012, **48**, 404–406.
- [74] S. Grundner, M. A. C. Markovits, G. Li, M. Tromp, E. A. Pidko, E. J. M. Hensen, A. Jentys, M. Sanchez-Sanchez and J. A. Lercher, *Nat. Commun.*, 2015, **6**, 7546.
- [75] P. J. Smeets, M. H. Groothaert and R. A. Schoonheydt, *Catal. Today*, 2005, **110**, 303–309.
- [76] M. J. Wulfers, S. Teketel, B. Ipek and R. F. Lobo, *Chem. Commun.*, 2015, **51**, 4447–4450.
- [77] K. Narsimhan, K. Iyoki, K. Dinh and Y. Román-Leshkov, *ACS Cent. Sci.*, 2016, **2**, 424–429.
- [78] C. Hammond, N. Dimitratos, R. L. Jenkins, J. A. Lopez-Sanchez, S. A. Kondrat, M. Hasbi Ab Rahim, M. M. Forde, A. Thetford, S. H. Taylor, H. Hagen, E. E. Stangland, J. H. Kang, J. M. Moulijn, D. J. Willock and G. J. Hutchings, *ACS Catal.*, 2013, **3**, 689–699.
- [79] C. Hammond, I. Hermans and N. Dimitratos, *ChemCatChem*, 2015, **7**, 434–440.
- [80] J. Weitkamp, *Solid State Ion.*, 2000, **131**, 175–188.
- [81] G. Li, E. A. Pidko, R. A. Van Santen, Z. Feng, C. Li and E. J. M. Hensen, *J. Catal.*, 2011, **284**, 194–206.
- [82] P. J. Smeets, J. S. Woertink, B. F. Sels, E. I. Solomon and R. A. Schoonheydt, *Inorg. Chem.*, 2010, **49**, 3573–3583.
- [83] S. Brandenberger, O. Kröcher, A. Tissler and R. Althoff, *Appl. Catal., A*, 2010, **373**, 168–175.
- [84] R. Palkovits, M. Antonietti, P. Kuhn, A. Thomas and F. Schüth, *Angew. Chem. Int. Ed.*, 2009, **48**, 6909–6912.
- [85] K. Sakaushi and M. Antonietti, *Acc. Chem. Res.*, 2015, **48**, 1591–1600.
- [86] M. Soorholtz, R. J. White, T. Zimmermann, M. Titirici, M. Antonietti, R. Palkovits and F. Schüth, *Chem. Commun.*, 2013, **49**, 240–242.
- [87] H.-C. Zhou, J. R. Long and O. M. Yaghi, *Chem. Rev.*, 2012, **112**, 673–674.
- [88] M. Zhao, S. Ou and C.-D. Wu, *Acc. Chem. Res.*, 2014, **47**, 1199–1207.
- [89] L. E. Kreno, K. Leong, O. K. Farha, M. Allendorf, R. P. Van Duyne and J. T. Hupp, *Chem. Rev.*, 2012, **112**, 1105–1125.
- [90] Y. Cui, Y. Yue, G. Qian and B. Chen, *Chem. Rev.*, 2012, **112**, 1126–1162.
- [91] A. Corma, H. García and F. X. Llabrés I Xamena, *Chem. Rev.*, 2010, **110**, 4606–4655.
- [92] B. Li, M. Chrzanowski, Y. Zhang and S. Ma, *Coord. Chem. Rev.*, 2016, **307**, 106–129.
- [93] L. Wang, Y. Han, X. Feng, J. Zhou, P. Qi and B. Wang, *Coord. Chem. Rev.*, 2016, **307**, 361–381.
- [94] J. Liu, L. Chen, H. Cui, J. Zhang, L. Zhang and C.-Y. Su, *Chem. Soc. Rev.*, 2014, **43**, 6011–6061.

- [95] J.-R. Li, J. Sculley and H.-C. Zhou, *Chem. Rev.*, 2012, **112**, 869–932.
- [96] T. Ikuno, J. Zheng, A. Vjunov, M. Sanchez-Sanchez, M. A. Ortuño, D. R. Pahls, J. L. Fulton, D. M. Camaioni, Z. Li, D. Ray, B. L. Mehdi, N. D. Browning, O. K. Farha, J. T. Hupp, C. J. Cramer, L. Gagliardi and J. A. Lercher, *J. Am. Chem. Soc.*, 2017, **139**, 10294–10301.
- [97] D. Osadchii, A. Olivos Suarez, A. Szécsényi, G. Li, M. Nasalevich, A. Dugulan, P. Serra-Crespo, E. Hensen, S. Veber, M. Fedin, G. Sankar, E. Pidko and J. Gascon, *ACS Catal.*, 2018, **8**, 5542–5548.
- [98] M. Boudart, *Adv. Catal.*, 1969, **20**, 153–166.
- [99] M. Boudart and M. A. McDonald, *J. Phys. Chem.*, 1984, **88**, 2185–2195.
- [100] J. S. J. Hargreaves, G. J. Hutchings, R. W. Joyner and C. J. Kiely, *J. Catal.*, 1992, **135**, 576–595.
- [101] S. K. Meher and G. Ranga Rao, *J. Colloid Interf. Sci.*, 2012, **373**, 46–56.
- [102] P. Lv, Z. Lu, S. Li, D. Ma, W. Zhang, Y. Zhang and Z. Yang, *RSC Adv.*, 2016, **6**, 104388–104397.
- [103] A. J. Medford, A. Vojvodic, J. S. Hummelshøj, J. Voss, F. Abild-Pedersen, F. Studt, T. Bligaard, A. Nilsson and J. K. Nørskov, *J. Catal.*, 2015, **328**, 36–42.
- [104] G. Cheng, X. Zhang, L. W. Chung, L. Xu and Y. Wu, *J. Am. Chem. Soc.*, 2015, **137**, 1706–1725.
- [105] T. Sperger, I. A. Sanhueza and F. Schoenebeck, *Acc. Chem. Res.*, 2016, **49**, 1311–1319.
- [106] T. Sperger, I. A. Sanhueza, I. Kalvet and F. Schoenebeck, *Chem. Rev.*, 2015, **115**, 9532–9586.
- [107] V. Van Speybroeck, K. Hemelsoet, L. Joos, M. Waroquier, R. G. Bell and C. R. A. Catlow, *Chem. Soc. Rev.*, 2015, **44**, 7044–7111.
- [108] E. A. Pidko, *ACS Catal.*, 2017, **7**, 4230–4234.
- [109] K. D. Vogiatzis, M. V. Polynski, J. K. Kirkland, J. Townsend, A. Hashemi, C. Liu and E. A. Pidko, *Chem. Rev.*, 2019, **119**, 2453–2523.
- [110] J. P. Perdew, K. Burke and M. Ernzerhof, *Phys. Rev. Lett.*, 1996, **77**, 3865–3868.
- [111] A. D. Becke, *Phys. Rev. A: At. Mol. Opt. Phys.*, 1988, **38**, 3098–3100.
- [112] C. Lee, W. Yang and R. G. Parr, *Phys. Rev. B: Condens. Matter*, 1988, **37**, 785–789.
- [113] J. Tao, J. P. Perdew, V. N. Staroverov and G. E. Scuseria, *Phys. Rev. Lett.*, 2003, **91**, year.
- [114] Y. Zhao and D. G. Truhlar, *J. Chem. Phys.*, 2006, **125**, year.
- [115] Y. Zhao and D. G. Truhlar, *Theor. Chem. Acc.*, 2008, **119**, 525.
- [116] A. D. Becke, *J. Chem. Phys.*, 1993, **98**, 5648–5652.
- [117] C. Adamo and V. Barone, *J. Chem. Phys.*, 1999, **110**, 6158–6170.
- [118] Y. Zhao, B. J. Lynch and D. G. Truhlar, *J. Phys. Chem. A*, 2004, **108**, 4786–4791.
- [119] M. G. Medvedev, I. S. Bushmarinov, J. Sun, J. P. Perdew and K. A. Lyssenko, *Science*, 2017, **355**, year.

- [120] K. R. Brorsen, Y. Yang, M. V. Pak and S. Hammes-Schiffer, *J. Phys. Chem. Lett.*, 2017, **8**, 2076–2081.
- [121] S. Grimme, *J. Comput. Chem.*, 2004, **25**, 1463–1473.
- [122] E. R. Johnson and A. D. Becke, *J. Chem. Phys.*, 2006, **124**, year.
- [123] F. Neese, D. G. Liakos and S. Ye, *J. Biol. Inorg. Chem.*, 2011, **16**, 821–829.
- [124] P. G. Szalay, T. Müller, G. Gidofalvi, H. Lischka and R. Shepard, *Chem. Rev.*, 2012, **112**, 108–181.
- [125] J. Olsen, B. O. Roos, P. Jørgensen and H. J. A. Jensen, *J. Chem. Phys.*, 1988, **89**, 2185–2192.
- [126] G. K. Chan and S. Sharma, *Annu. Rev. Phys. Chem.*, 2011, **62**, 465–481.
- [127] K. Andersson, P. Malmqvist and B. O. Roos, *J. Chem. Phys.*, 1992, **96**, 1218–1226.

2

METHANE OXIDATION OVER FE-ZSM-5 ZEOLITE – THEORY OF C-H BOND ACTIVATION

Periodic DFT calculations were carried out to investigate the mechanism of methane oxidation with H_2O_2 over the defined Fe sites in Fe/ZSM-5 zeolite. The initial Fe site is modelled as a $[(H_2O)_2-Fe(III)-(\mu O)_2-Fe(III)-(H_2O)_2]^{2+}$ extra-framework cluster deposited in the zeolite pore charge-compensated by two anionic lattice sites. The activation of this cluster with H_2O_2 gives rise to the formation of a variety of Fe(III)-oxo and Fe(IV)-oxo complexes potentially reactive towards methane dissociation. These sites are all able to promote the first C-H bond cleavage in methane by following three possible reaction mechanisms, namely, the (a) heterolytic and (b) homolytic methane dissociation as well as Fenton-type involving free OH radicals as the catalytic species. The C-H activation step is followed by the formation of MeOH and MeOOH and the regeneration of the active site. The Fenton-type path is found to proceed with the lowest activation barrier. Although the barriers for the alternative heterolytic and homolytic pathways are found to be somewhat higher, they are still quite favourable and expected to be feasible under reaction conditions, resulting ultimately in MeOH and MeOOH products. H_2O_2 oxidant competes with CH_4 substrate for the same sites. Since the oxidation of H_2O_2 to O_2 and two $[H^+]$ is energetically more favourable than the C-H oxo-functionalization, the overall efficiency of the latter target process remains low.

This chapter is based on the following publication: Á. Szécsényi, G. Li, J. Gascon, and E. A. Pidko, Mechanistic complexity of methane oxidation with H_2O_2 by single-site Fe/ZSM-5 catalyst, *ACS Catalysis*, **8** (2018) 7961-7972.

2.1. INTRODUCTION

As elaborated in Chapter 1, two principal C-H activation mechanisms providing a path towards selective methane activation are usually distinguished that are (1) the heterolytic and (2) homolytic reaction mechanisms (Figure 2.1) [1, 2]. In the former case, the C-H bond is activated over an acid-base pair to form an anionic alkyl group stabilized by the acid (often a metal cation) and a proton accepted by the base part of the active site. Note that the heterolytic C-H cleavage is not accompanied by any redox processes within the active site. The actual oxidation of the alkyl moiety should then take place at the subsequent steps of the overall catalytic process. In the homolytic mechanism, the C-H bond breaks with the formation of two radical species – the alkyl radical and a formally H radical. The H radical represents a transient species that is readily accepted by the basic moiety of the active site, which is at the same time reduced with $1 e^-$. The subsequent rebound of the CH_3 radical completes the two-electron reduction process and yields the oxidized organic product or surface-bound intermediate. Given the fact that homolytic C-H activation commonly yield a “free” alkyl radical, while the energy losses due to the cleavage of a strong C-H bond come predominantly from the single-electron reduction of the active complex accompanied by its protonation, the basicity of the proton-accepting site (B) – that is basically the strength of the resulting B-H bond - has been recognized as one of the critical parameters defining the overall reactivity of a catalyst towards homolytic C-H activation [3, 4]. The direct relationships between this parameter and the computed barriers for C-H activation have been demonstrated in the recent studies by Nørskov and Studt [5] *et al.* for a wide class of potential heterogeneous catalysts.

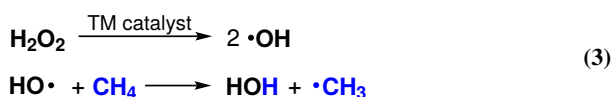
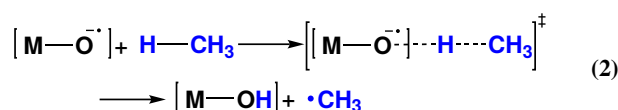
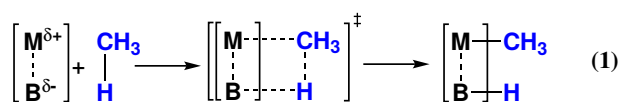


Figure 2.1: Potential mechanistic pathways for C-H bond cleavage. (1) heterolytic (2) homolytic (3) Fenton-type activation investigated in this paper.

In the chemistry of iron [6], the preference for the particular C-H activation mechanism is usually defined by the oxidation state of the Fe site, its coordination environment and nature of the ligands [1]. Heterolytic C-H cleavage (Figure 2.1 (1)) is commonly observed over the lower-valent Fe sites (e.g. 3+ and 2+) conjugated with a strong base site. The homolytic C-H dissociation (Figure 2.1 (2)) is more typical for higher valent Fe sites that feature more covalent type of bonding and facilitate the oxidative activation of the substrate coupled with the reduction of Fe. In addition to these two very generic reaction channels, scientists distinguish one more mechanism specific to Fe chemistry that is the Fenton-type mechanism of C-H activation (Figure 2.1 (3)). Although formally this mechanism can be regarded as a sub-type of the homolytic C-H bond dissociation (2), it is commonly considered separately in view of the secondary role the Fe-site plays in it. In the Fenton chemistry, iron ions are initiating the radical oxidation paths by producing free OH radical species, which activate C-H bonds [7, 8]. In the context of selective methane oxo-functionalization, the Fenton-type reactions have been explored in the works by the group of Shulpin [9–11] who demonstrated that in the presence of Fe(II) ions methane can be oxidized with H_2O_2 and O_2 to produce MeOOH as the main product. Similar chemistry has recently been proposed by Hutchings [12] and co-workers to govern the methane oxidation by Pd nanoparticles.

In many scientific studies only one type of activation is investigated. For example, the structure-activity relation derived by Nørskov [4] *et al.* is valid only under the assumption of homolytic C-H bond activation. However, there are DFT studies that propose the heterolytic methane dissociation over Cu and Fe clusters deposited in zeolites [13–15]. In a complex system such as transition-metal exchanged zeolites, different clusters can be found [16] which might promote diverse types of C-H bond activation. In this chapter we aim to investigate how the different Fe clusters influence the type and energetics of C-H bond cleavage. For this we analysed this reaction step over numerous clusters created from binuclear Fe(III)-oxo with H_2O_2 based on the catalytic system of Hutchings [17] *et al.*, presented in Chapter 1.

Most theoretical work focuses on the rate determining C-H bond activation step, but here we also present the whole catalytic cycle including the formation of the active site, the C-H bond activation, product formation followed by the regeneration of the initial site. All three previously introduced potential reaction mechanisms were considered for methane activation. The comprehensive description of the reaction network provides us with atomic level insights into this immensely complicated heterogeneous catalytic process.

2.2. MODEL AND SIMULATION DETAILS

THE spin polarized periodic DFT calculations were carried out with the Vienna *Ab Initio* Simulation Package (VASP) [18–21]. PBE exchange-correlation functional [22, 23] was used together with the plane wave basis set with a cut-off energy of 450 eV and the projector augmented wave (PAW) method [24, 25]. To account for the van der Waals interactions, the semi-empirical Grimme’s dispersion correction with Becke-Jonson damping (DFT-D3(BJ)) method [26] was used. A Gaussian smearing of the population of partial occupancies with a width of 0.05 eV was used during iterative diagonalization of the Kohn-Sham Hamiltonian. Brillouin zone sampling was restricted to the Gamma point [27]. Convergence was assumed to be reached when the force on each atoms was below 0.04 eV \AA^{-1} .

To locate the transition states the nudged elastic band method (NEB) [28] was applied. The maximum energy geometry along the reaction path generated by the NEB method was further optimized using a quasi-Newton algorithm. In this procedure, only the extra-framework atoms, and relevant framework atoms were relaxed. Vibrational frequencies were calculated using the finite difference method (0.02 Å atomic displacements) as implemented in VASP. Transition state showed a single imaginary frequency corresponding to the reaction path.

As an initial active site model, a binuclear Fe cluster coordinated by framework oxygen atoms, extra-framework μ -oxoes and water molecules at its first coordination shell with a total coordination number of six for each iron centre (octahedral environment) $[(\text{H}_2\text{O})_2\text{-Fe(III)-}(\mu\text{O})_2\text{-Fe(III)-}(\text{H}_2\text{O})_2]^{2+}$ is taken into consideration. The cluster is placed over the 8-member ring of the zeolite. Two Si atoms of the ring is substituted with Al in the T7 and T12 sites (Figure 2.2). The unit cell lattice parameters are optimized, and are fixed throughout the calculations ($a = 20.1$, $b = 19.8$, $c = 13.2$, $\alpha = \beta = \gamma = 90^\circ$). We based our assumption on the initial site on the DFT study of Li [16] *et al.*, which indicates this cluster as the most stable one among mono-, bi- and tetra-nuclear species containing Fe(II) and Fe(III) ions in oxidative aqueous environment. This is in agreement with the experimental and computational results of Hutchings [17] *et al.*, who concluded with high uncertainty an $[(\text{H}_2\text{O})(\text{HO})\text{-Fe-}(\mu\text{OH})_2\text{-Fe-(OH)(H}_2\text{O})]^{2+}$ cluster as the representative species of their system. This cluster can be obtained from the previously described one by two H^+ -transfer from the H_2O molecules to the bridging O atoms, which is a very facile reaction, and does not change the stability of the cluster significantly as we demonstrate it in our calculations.

The octahedral environment may change during the course of the reaction, for

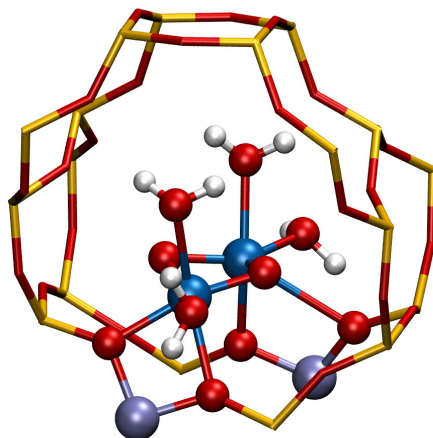


Figure 2.2: The initial $[(\text{H}_2\text{O})_2-\text{Fe}(\text{III})-(\mu\text{O})_2-\text{Fe}(\text{III})-(\text{H}_2\text{O})_2]^{2+}$ model placed in the ZSM5 zeolite pore. The rest of the atoms in the periodic unit cell are omitted from the picture for the sake of visual clarity. (Si: yellow, Al: purple, Fe: blue, O:red, H: white)

example one or both Fe atoms decoordinate from one of the framework O atoms. Due to the high number of structures this is not elaborated in the text.

All possible spin states ($S = 0, 1, 2, 3, 4, 5$) were considered for the initial Fe cluster. DFT calculations point to the $S = 3$ state as the most stable one. However, in this state one H_2O molecule decoordinates from the Fe and forms a H bond with another H_2O molecule providing thus an artificial stabilization to the overall system. The release of H_2O is triggered by the change of spin state, which results in different orbital energies, the change of ligand field and therefore the preferred geometry of the Fe complex. A similar effect is observed for the $S = 4$ state. The second most stable configuration is the antiferromagnetically coupled $S = 0$ state (broken symmetry singlet). Spin density analysis shows that the absolute value of spin assigned to each atom is similar to those in the $S = 5$ state. As it was shown previously that the antiferromagnetic coupling does not significantly influence the reactivity in the case of O bridged Fe dimers [29], for the reactivity analysis, we focused on the ferromagnetically coupled high spin electronic configurations rather than the antiferromagnetically coupled $S = 0$ state. The extensive justification for this simplification has been provided by Baerends [30] *et al.*. The preferred high spin state changes in the course of the reaction with the oxidation state of the Fe cluster and the formation of radicals.

In this study we base our mechanistic analysis on the discussion of relative electronic energies only, while the entropic effects are considered to have only a minor effect on the reaction profiles. This conclusion is supported by a series of test calculations.

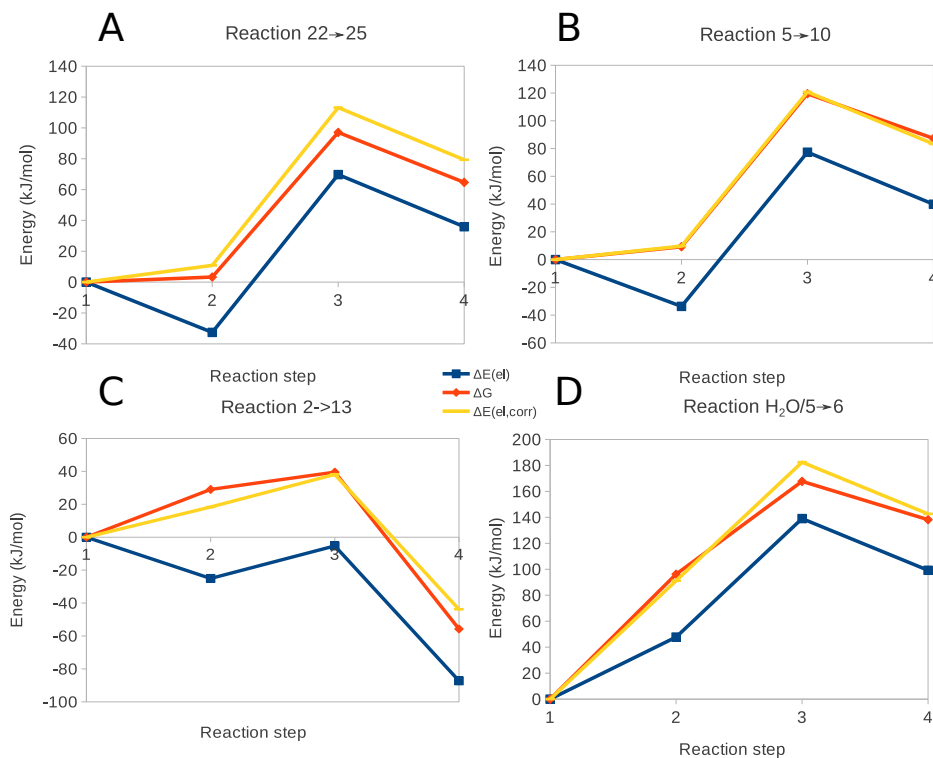


Figure 2.3: Reaction energy diagram of reaction A) 22→25, B) 5→10, C) 2→13, D) $\text{H}_2\text{O}/5 \rightarrow 6$ showing the electronic ($\Delta E(\text{el})$), Gibbs free (ΔG) and electronic +43 kJ/mol ($\Delta E(\text{el,corr})$) energy. The reaction steps are: 1) active site + gas phase methane, 2) active site + adsorbed methane, 3) TS of C-H bond dissociation, 4) active site + CH_3 group

Entropic effects are significant for the thermodynamics of the adsorption and desorption steps. However it was found that the relative entropy contribution of the reaction steps between already adsorbed species is minor, also in zeolites [31]. Recent works successfully employ different approximation schemes allowing extrapolating the free energy contributions among varied classes of materials [4, 32]. By examining the work of Brogaard and Olsbye [31] we can conclude that the relative Gibbs free energy (ΔG) can be reasonably well approximated by correcting the relative electronic energy $\Delta E(\text{el})$ with $\Delta G - \Delta E(\text{el})$ of the adsorption step. To demonstrate this simplification is valid to our system we also performed frequency analysis on four C-H bond reaction steps to calculate the Gibbs free energies within the harmonic approximation. Frequency analysis of the stationary points was performed by means of the finite difference method as implemented in VASP. Small displacements (0.02 Å) were used to estimate the numerical Hessian matrix. The analysis only includes the atoms

of the active site and adsorbate(s). The temperature was 50°C consistent with the experiments. The average of $\Delta G - \Delta E(\text{el})$ of the methane adsorption step was found to be 43 kJ/mol. The corrected electronic energy was computed the following way: $\Delta E(\text{el,corr}) = \Delta E(\text{el}) + x * 43 \text{ kJ/mol}$, where x is the number of the previously adsorbed methane molecules (0 for the first structure and 1 for the rest). The presented results in Figure 2.3 demonstrate, that the $\Delta E(\text{el,corr})$ approximates ΔG reasonably well, which means that the entropic effect is uniform for all reactions. Consequently the reaction profile changes the same way, which means that the relative electronic energy diagram is suitable to qualitatively discuss reaction mechanisms and compare reaction pathways.

In the course of the reaction, H_2O molecules leave the Fe sites and new H_2O molecules are formed (e.g. upon the decomposition of H_2O_2) that are not connected to the Fe atoms. These molecules form a hydrogen-bond network connecting the O- and H-sites associated with the cluster and the zeolite lattice. These networks can very easily rearrange upon methane adsorption and/or transformations without affecting the electronic properties of the reactive Fe species but influencing the overall energy of the system. As a result, we observed that the barrier heights and reaction energies for elementary steps can be quite substantially affected by the positions of these uncoordinated H_2O ($E(\text{H-bond in water}) = \sim 20 \text{ kJ/mol}$). Extensive analysis of the different isomeric structures involved in similar reaction steps evidences that this is an artefact of the model. In the actual aqueous media these effects would have been counterbalanced by the presence of bulk H_2O molecules. However, the comprehensive sampling required for such an extensive model is in conflict with the goals of the current study. Therefore, we neglected the respective effects and always removed non-coordinated physically adsorbed H_2O molecules from the unit cell after their formation. The resulting desorption energy of H_2O molecules are not discussed in the article, but they are shown on the reaction energy diagrams (e.g. reaction step $2x\text{H}_2\text{O}/5 \rightarrow 5$ in Figure 2.13).

The numbering of the structures in the paper is not presented in a sequential order but follows individual reaction paths from the beginning to the formation of CH_3OH or CH_3OOH (as summarized in Figures 2.5 and 2.6). Conformational isomers and CH_4 adsorbed in different positions of the same active site are marked with ν after the name of the structure. H_2O in front of the name of the structure indicates uncoordinated H_2O molecule which will be removed in a later step of the reaction.

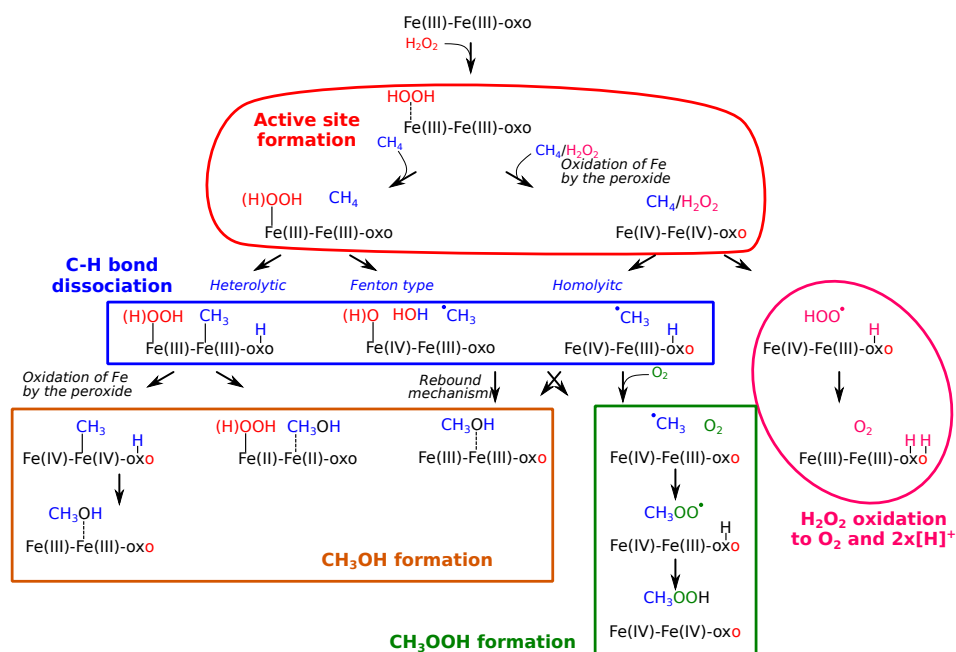


Figure 2.4: Schematic representation of the reaction network and most important steps underlying the oxidation of methane with H_2O_2 over Fe/ZSM-5 zeolite. The detailed description of the structures can be found in the supporting information.

2.3. RESULTS AND DISCUSSION

THE schematic representation of the favourable reaction mechanisms identified in our study is shown in Figure 2.4. The detailed structures can be found in Figure 2.5 and Figure 2.6. The active Fe(III) and Fe(IV) sites are formed by the adsorption and dissociation of H_2O_2 . The reorganization of the H ions results in different active sites. Our calculations show that Fe(III) species catalyse the heterolytic and the Fenton-type activation, while Fe(IV) species facilitate the homolytic activation of methane. The Fe clusters are grouped based on the average formal oxidation state. For example if one Fe atom is formally +2, while the other is in +4 oxidation state the average is +3, and the cluster is considered an Fe(III) cluster.

From Fe(III) species, methanol can be formed via the combination of the methyl group and an OH group before or after the oxidation of the cluster by the peroxo ligand. In the cases of homolytic and Fenton-type mechanisms, a methyl radical is formed, which can further transform to CH_3OH via the rebound mechanism or to CH_3OOH via the reaction with O_2 (inevitably formed by a parallel H_2O_2 decomposition process) and the abstraction of a H atom from the active site. Fe(IV) sites are the active species for both the homolytic dissociation of methane and the decomposition of H_2O_2 to O_2 and $[\text{H}^+]$ ions. In the next sections we provide a detailed description of each reaction

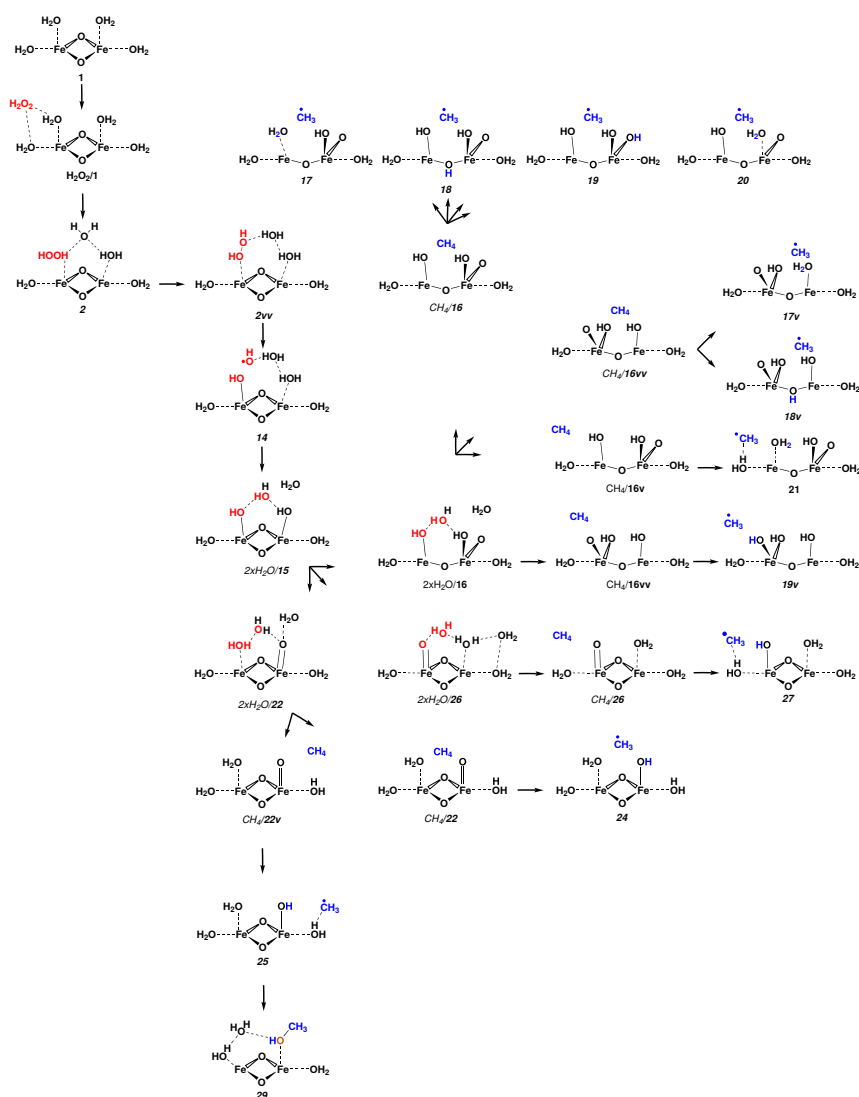


Figure 2.6: Schematic representation of the other part of the reaction network. It shows the homolytic C-H bond activation paths and the MeOH formation.

step.

2.3.1. ACTIVE SITE FORMATION

The first step of the reaction is the formation of the active site. All investigated pathways (Figure 2.7) start with the adsorption of H_2O_2 in the zeolite pore ($\text{H}_2\text{O}_2/\text{I}$) and its subsequent coordination to the active site, where it substitutes one H_2O molecule (2).

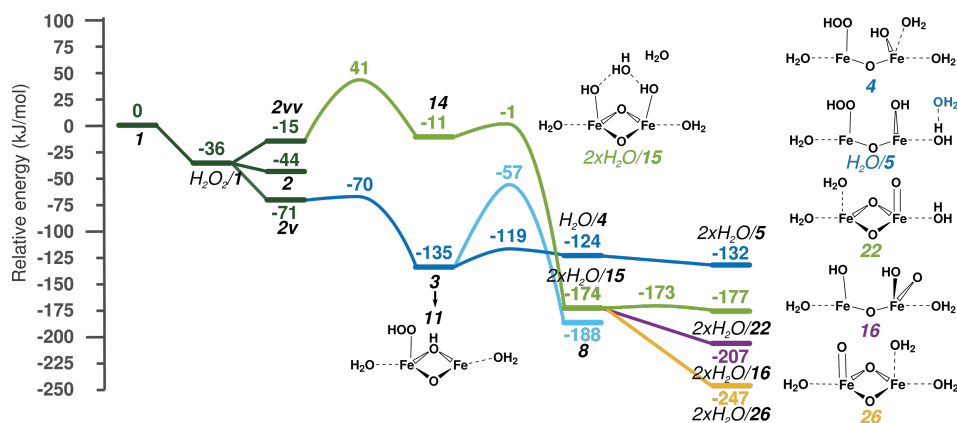


Figure 2.7: Potential reaction pathways for the active site formation as the reaction of the Fe cluster with H_2O_2 and the schematic representations of the key intermediates.

These steps are exothermic by -44 kJ/mol. The conformational isomers of **2v** and **2vv** shown on Figure 2.7 are formed by the rotation of the non-coordinated H_2O molecule and H_2O_2 . The difference in energy between these structures is an artefact of the model resulting from the rearrangement of H bonds as described in the Model and Simulation details section. This structural rearrangement is necessary to adequately probe the alternative reaction pathways for the subsequent steps involving the H_2O molecule as a proton-mediator. From this stage, two alternative reaction channels can be distinguished resulting in an active site, namely, (1) the direct oxidation of both Fe(III) centres to Fe(IV) via the homolytic cleavage of the peroxide moiety or (2) the deprotonation of H_2O_2 to form an Fe-bound peroxo-ligand and leaving the formal oxidation state of the iron ions unchanged.

The first path proceeds with a barrier of only 56 kJ/mol and yields a transient OH radical (**14**) that readily subtracts a H atom from a neighbouring coordinated H_2O ($E^\ddagger = 10$ kJ/mol) resulting in $2x\text{H}_2\text{O}/15$. The isomerization of this species by proton reshuffling gives $2x\text{H}_2\text{O}/22$ ($\Delta E = -3$ kJ/mol) and $2x\text{H}_2\text{O}/26$ ($\Delta E = -73$ kJ/mol). Such a water-assisted H transfer is a very facile reaction that in the case of $2x\text{H}_2\text{O}/15 \rightarrow 2x\text{H}_2\text{O}/22$ step shows a barrier of 1 kJ/mol. Since we expect the activation barrier for similar H-bonding rearrangements to be in the same order of magnitude, the transition states were not located in other cases. This type of reaction for ferryl ion formation was considered earlier by Baerends *et al.* [33, 34]. An alternative path of $2x\text{H}_2\text{O}/15 \rightarrow 2x\text{H}_2\text{O}/16$ leads to the cleavage of one Fe- μO bonds ($\Delta E = -33$ kJ/mol). The diamond shape of the Fe-oxo cluster transforms to a near linear Fe-O-Fe species and a terminal O is formed. Transition state energy was found to be low for this type of reaction as described in the next section at reaction **3** \rightarrow $\text{H}_2\text{O}/4$.

The second path starts with the deprotonation of H_2O_2 by the bridging O site to form a bridging OH group and a terminal OOH ligand (**3**). The non-coordinating H_2O molecule facilitates this reaction via a proton shuttling mechanism. Next, the Fe- μ OH bond breaks with the activation barrier of only 16 kJ/mol to form an activated intermediate $H_2O/4$, which is a near-linear Fe-O-Fe cluster with a terminal OH ligand. This reaction is similar to the previously described $2xH_2O/15 \rightarrow 2xH_2O/16$ transformation. The activation barrier of other Fe- μ O bond cleavage is expected to be in the same range in the other similar reactions and it is significantly lower than that of the rate determining step, therefore the activation barriers of similar steps were not calculated for other cases.

In the next reaction steps H_2O is decoordinated from the Fe centre. This is necessary, because during the heterolytic dissociation the formation of an Fe-C bond occurs. Since the complex is originally in octahedral coordination, this would not be possible without the removal of one ligand. We decided to decouple the H_2O decoordination from the CH_4 activation because otherwise the energy change resulting from the forming H bonds and the Fe-O bond breaking would artificially be included in the reaction and transition state energies of the C-H bond dissociation. In reaction $H_2O/4 \rightarrow 2xH_2O/5$ ($\Delta E = 9$ kJ/mol) one H_2O molecule leaves the Fe atom. Removing one H_2O molecule from $2xH_2O/5$ results in $H_2O/5$ (shown in Figure 2.7) and by removing the second uncoordinated H_2O molecule **5** is obtained. In this case the Fe atom where the H_2O was removed from has only five ligands. This will be the Fe atom which will form the Fe-C bond. We are going to focus on this Fe atom further in this paragraph. The removal of two H_2O molecules, one coordinated and one uncoordinated, from structure **3** results in structure **11**, which also has a five-coordinated Fe atom. The difference between **11** and **5** is that the Fe in **11** has one ligand that moves freely, the other four, the framework and the bridging O atoms, are in fixed positions, while the Fe atom of **5** has two ligands that are rather flexible, these are an H_2O molecule and an OH ligand. This difference leads to different structures. The Fe atom of **11** is in a square pyramid geometry, while the Fe of **5** is closer to a trigonal bipyramidal geometry.

The first pathway is thermodynamically more favourable than the second, while the second has lower reaction barriers, thus kinetically more favourable. However, if we inspect the structures more closely, we realize that by cleaving the peroxo bond of **3** (\rightarrow **8**) ($\Delta E = -53$ kJ/mol; $E^\ddagger = 78$ kJ/mol) and reshuffling the protons of **8**, the structures of the first pathway can be obtained. This indicates that the occurrence of all the previously described structures is feasible.

To decrease the influence of the fluctuating H bonds, the H_2O molecules not coordi-

nated to the Fe were removed (*vide supra*). This way the structures shown in Figure 2.7: **4**, **5**, **11**, **16**, **22** and **26**, were obtained. These are the active sites applied in the subsequent C-H bond activation steps. After removing the extra water molecules the difference in energy between **15**, **16**, **22** and **26** decreases from 127 kJ/mol to 23 kJ/mol. Their order of stability also changes, **16** becomes the most stable species among them. This energy difference is rather small. In the next section we considered the active site and the gas phase methane for all reactions as reference point to enable the direct assessment of their reactivity.

2.3.2. C-H BOND ACTIVATION

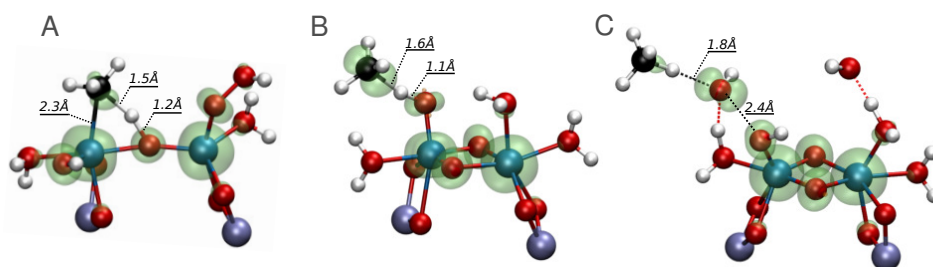


Figure 2.8: Transition state typical for A) heterolytic dissociation, reaction **5**→**9**, B) homolytic dissociation, reaction **26**→**27**, C) Fenton-type dissociation, reaction **2**→**13**. The isosurface represents the spin density. Colour coding: (Al: purple, Fe: blue, O:red, C: black, H: white. The clusters shown here are part of a periodic model containing the unit cell of ZSM-5 zeolite, the Fe cluster and the reactants.

The next step of the reaction is the C-H bond cleavage of methane. The previously described Fe(III) and Fe(IV) complexes were selected to act as active sites in the reaction. As it can be seen in Figure 2.4 Fe(III) complexes catalyse the heterolytic and Fenton-type, while Fe(IV) complexes promote the homolytic oxidation of methane. Figure 2.8 shows an example transition state of each case. The isosurface represents the spin density. Figure 2.8 A is a representative of the heterolytic dissociation (**5**→**9**). The bridging O subtracts the H from the CH₄, and the CH₃ ligand is already connected to the Fe in the transition state, which means that the Fe orbitals participate in the reaction. The lack of spin density around the C indicates that there are no unpaired electrons on the C orbitals, and this is indeed a heterolytic dissociation. Figure 2.8 B shows the transition state of reaction **26**→**27** of homolytic C-H bond dissociation. In this case the terminal O accepts the H atom and CH₃ radical is formed. The C-H bond distance is smaller than the H-O bond distance implying a late transition state. This is typical for the terminal O, however in other type of O atoms (bridging O or OH ligand) this is not necessary the situation. The spin density isosurface shows that the C has more α than β electrons indicative of a radical reaction. Part C of Figure 2.8 shows

the transition state of a Fenton-type C-H bond dissociation (**2**→**13**). The spin density accumulates around the forming OH radical which cleaves the C-H bond. This is also a radical reaction.

2

In the following sections we present the detailed cases of each type of CH₄ activation.

HETEROLYTIC ACTIVATION

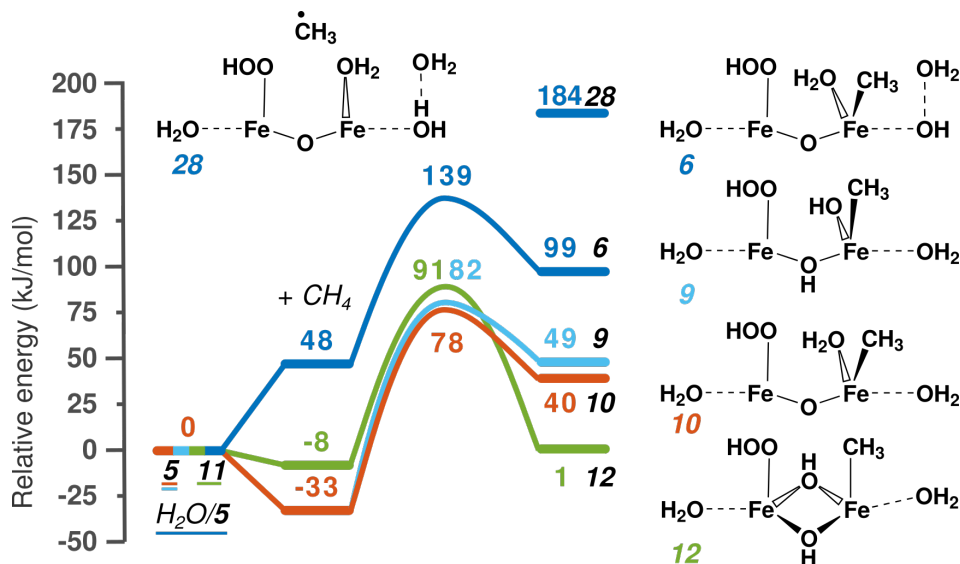


Figure 2.9: Reaction energy diagram of the heterolytic C-H bond cleavage of methane. The reference point is the active site and gas phase methane. The first step is methane adsorption in the zeolite pore, followed by the heterolytic dissociation of the first C-H bond of methane, and the formation of an Fe-CH₃ moiety an OH ligand, or water depending on the nature of the proton-accepting site.

The reaction energy diagram of the heterolytic activation is shown in Figure 2.9. The reference point is the active site and gas phase methane. At first methane is adsorbed in the zeolite pore, which is followed by the heterolytic dissociation of the first C-H bond of CH₄ and the formation of a CH₃ group and an OH ligand or H₂O. For this reaction to occur Fe needs to have an empty coordination site to accommodate the CH₃ group. Hence one ($2xH_2O/4 \rightarrow 5$ and $H_2O/5$ and $3 \rightarrow 11$) H₂O ligand was decoordinated from one of the Fe atoms during the formation of the active site as described in the previous section.

The first possibility is the reaction $H_2O/5 \rightarrow 6$ (dark blue line). It starts with the CH₄ adsorption in the zeolite pore. Since the Fe site is not located in the main channel there is not enough space for the methane to coordinate favourably to the active site. The confinement of the framework and the cluster results in repulsive forces around

the methane. This entails a positive adsorption energy and a relatively high reaction energy (99 kJ/mol) and reaction barrier (139 kJ/mol).

Reaction **5**→**9** (light blue) and **5**→**10** (orange) show the reaction over the same cluster as $H_2O/5$, but with one less H_2O molecule around the cluster. Methane is adsorbed at a different position, resulting in a negative adsorption energy. The difference between the two reactions is the activating O. In reaction **5**→**9** methane is activated by a bridging O ($\Delta E = 49$ kJ/mol, $E^\ddagger = 82$ kJ/mol), while in case of reaction **5**→**10** methane is activated by the terminal OH group ($\Delta E = 40$ kJ/mol, $E^\ddagger = 78$ kJ/mol). Since both the reaction barrier and energy are very similar this indicates that the type of O does not influence significantly the reactivity.

Next, we compare the performance of two active sites **5** and **11**. As described previously these two structures have an Fe atom with five ligands in different geometry. The comparison of paths **5**→**9** and **11**→**12** evidences that this difference in geometry does not have an effect on the reaction barrier (91 vs 82 kJ/mol respectively), however the formation of the octahedral environment greatly stabilizes structure **12** (reaction energy of 49 vs 1 kJ/mol).

It is interesting to take the adsorbed methane as the reference point for our comparison. The qualitative picture for **5**→**9**, **5**→**10** and **11**→**12** does not change remarkably. However reaction $H_2O/5$ →**6** will have much lower reaction barrier and energy, so that it becomes the most favourable path. When confinement plays a role the adsorption has to be taken into account.

As mentioned earlier heterolytic activation occurs on Fe(III) sites. On Figure 2.9 structure **28** is the result of homolytic dissociation over $H_2O/5$. The OH group of **5** accepts a H atom and a CH_3 radical is formed. The reaction energy is 85 kJ/mol higher compared to the formation of intermediate **6**, where instead of CH_3 radical a CH_3 ligand is formed. This is most likely due to the fact that homolytic dissociation entails the reduction of the Fe site, in this case to Fe(II) state, while there is no formal oxidation state change for heterolytic dissociation.

HOMOLYTIC ACTIVATION

The reaction energy diagrams of homolytic C-H cleavage are shown in Figure 2.10. Methane is adsorbed in the zeolite followed by its homolytic dissociation and the formation of a CH_3 radical and an OH ligand or H_2O connected to Fe. The formal oxidation state of Fe in the active cluster is +4, which means that the high spin state is 8/2. During the reaction one Fe is reduced to +3 while C is formally oxidized. The highest possible spin state becomes 10/2 (Fe(III)-Fe(IV) and CH_3 radical), however it

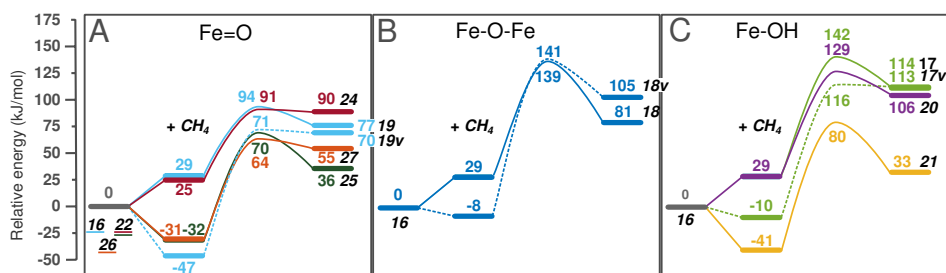


Figure 2.10: Reaction energy diagram of the homolytic C-H bond cleavage of methane. The reference point is the active site and gas phase methane. The first step is methane adsorption in the zeolite pore followed by the homolytic dissociation of the first C-H bond of methane, and the formation of a methyl radical and an OH ligand, or water. The same coloured lines represent reaction pathways where the cluster and the H-accepting oxygen is the same, but the position of adsorbed methane is different.

can happen that the CH_3 radical is antiferromagnetically coupled with the Fe cluster, and the more stable spin state remains 8/2 at the end of this reaction step. Figure 2.10 summarizes the results obtained for the most stable configurations.

In Figure 2.10 the reaction is grouped based on the type of the O ligand that abstract the H from CH_4 : A) terminal, B) bridging or C) OH group. The lowest reaction barrier over terminal O and OH are similar ($22 \rightarrow 27$ and $16 \rightarrow 21$; $E^\ddagger = 64$ and 80 kJ/mol respectively), however the reaction barrier over the bridging O is relatively high ($E^\ddagger = 139$ kJ/mol). This is the result of the position of the Fe cluster, which is not located in the main channel, but in a somewhat confined position. The bridging O is not easily accessible. The same reaction modelled in a different position in the main channel resulted in a lower adsorption (-43 kJ/mol), reaction barrier (69 kJ/mol) and reaction energy (48 kJ/mol), which are comparable to the best values obtained for Fe=O and Fe-OH (transition state structure shown in Figure 2.11). In general this means that Fe=O, Fe-OH and Fe- μ O-Fe oxygens are all able to activate methane.

The same trend can be observed here as in the case of the heterolytic dissociation. The positive adsorption energy decreases the intrinsic barriers and reaction energies (reference point is the active site with adsorbed methane), however compared to the original reference point (gas phase methane and zeolite) the reactions with positive adsorption energy are less exothermic and have higher barriers. This is emphasized by the same colour reaction pathways, which represent routes where the activating O and the Fe cluster are the same, but the methane is adsorbed in a different position in the zeolite. An example is the case of $16 \rightarrow 19$ and $16 \rightarrow 19v$ (light blue on Figure 2.10 A). In the first case methane adsorbs above the cluster with a positive adsorption energy, while in the second case methane adsorbs in the main channel next to the cluster and accesses the terminal O from there. In the first case the intrinsic activation energy is a mere 65 kJ/mol, while in the second case it is 118 kJ/mol, however if we take the gas

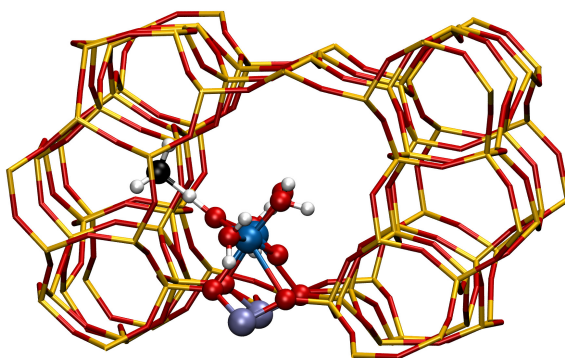


Figure 2.11: Transition state structure of homolytic dissociation of methane over a binuclear Fe(IV)-oxo complex placed in the main channel of the zeolite.

phase methane as reference, the second reaction becomes more favourable with a reaction barrier of 71 kJ/mol vs 94 kJ/mol.

FENTON-TYPE ACTIVATION

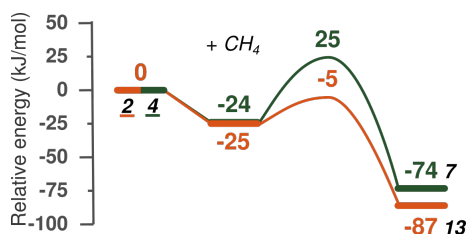


Figure 2.12: Reaction energy diagram of the Fenton-type C-H bond cleavage of methane. The reference point is the active site and gas phase methane. The first step is the methane adsorption in the zeolite pore, followed by the homolytic dissociation of the peroxy bond, formation of OH radical and the dissociation of the first C-H bond of methane, and the formation of a methyl radical and water molecule at the same step.

Fenton-type activation, as described earlier, is a type of homolytic C-H bond dissociation. The important distinction from the previously presented homolytic dissociation is that the role of the transition metal catalyst is to produce the active OH radicals. Here we present two possibilities for this type of reaction of which reaction energy diagrams shown in Figure 2.12. The active sites are structure **2** and **4**, already introduced in the previous section. **2** is formed by coordinating of H₂O₂ to Fe, while **4** is formed by the deprotonation of **2** and the consecutive cleavage of the Fe-μOH group (Figure 2.7). In the transition states the CH₄ is effectively intact and an OH radical is formed. The reaction can be viewed as a redox reaction, in which the O atoms of H₂O₂ oxidise C in methane and Fe of the active site. The reaction yields CH₃ radical, H₂O molecule and Fe(IV)Fe(III) complex. The Fenton-type methane activation is a highly favourable process (ΔE = -74 and -87 kJ/mol) proceeding with barriers of 25 and -5 kJ/mol (Figure

2.12).

The lowest activation energy and thermodynamic favourability belongs to the Fenton-type activation. In general Fenton-type reaction is undesired, because it is very difficult to control and this path is thought to decrease the selectivity of the overall process. The lowest reaction and activation energies of the heterolytic and homolytic dissociation pathways are comparable, which implies that both mechanisms are effectively possible, and all type of O ligands can potentially act as H acceptors providing a favourable reaction channel for CH_4 activation.

2.3.3. CLOSING THE REACTION CYCLE

METHANOL FORMATION AFTER HETEROLYTIC METHANE ACTIVATION

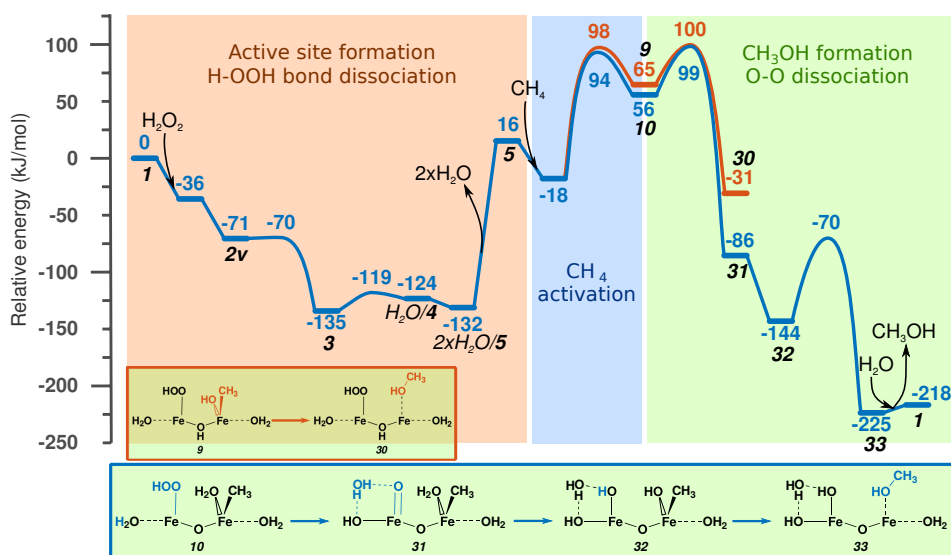


Figure 2.13: Reaction energy diagram of methane to methanol formation including the formation of the active site, heterolytic C-H bond activation, the formation of CH_3OH and the active site regeneration.

The heterolytic mechanism of C-H activation is seldom considered for the selective oxidation process, because the subsequent CH_3OH formation would require a dual-site reductive elimination process. Figure 2.13 shows the full catalytic cycle through intermediate **10** and **9**. It starts with the activation of the binuclear Fe(III) site by H_2O_2 to obtain $2x\text{H}_2\text{O}/5$ active site. The physically adsorbed water is then removed, as explained in the Model and simulation details section. This step results in a 148 kJ/mol energy loss of the model system. This is an artificial increase in the overall energy, however it is necessary to show it here to keep the reference point constant throughout

the reaction energy diagram. The same is true for the reaction step $2xH_2O/22 \rightarrow 22$ in Figure 2.14. The desorption step is followed by the adsorption and heterolytic dissociation of CH_4 . To form methanol the recombination of the CH_3 and an OH ligand is needed. This decreases the formal oxidation state of Fe(III)Fe(III) by 2 resulting in an Fe(II)Fe(II) structure. This is shown with orange line in the Figure 2.13, where **9** is transformed to **30** with a barrier of 35 kJ/mol and -96 kJ/mol reaction energy. To regenerate the catalyst the dissociation of the peroxo bond and the rearrangement of H ions are needed. These steps are not calculated here, previous calculations indicate that the peroxo bond dissociation proceeds with a barrier of ~40-70 kJ/mol, and the H atom transfer is almost barrierless.

The other possibility is the oxidation of the cluster prior to the formation of MeOH. This route is indicated by a blue line in Figure 2.13. The activation barrier for the peroxo bond (**10**→**31**) cleavage is 44 kJ/mol. The H atom transfer to form **32** provides a 58 kJ/mol energy gain, which can be explained by the formation of Fe(IV)Fe(IV) cluster from a formally Fe(V)Fe(III) intermediate. In the next step MeOH is formed (**33**) with a barrier of 74 kJ/mol that is needed to reduce the Fe atoms. After the desorption of MeOH, the rearrangement of H atoms and the formation of a bridging O the initial Fe(III)-oxo cluster takes place. As described earlier, all these steps proceed with a low reaction barrier.

These data suggest that there is no energetic preference in the order of MeOH formation and the oxidation of the Fe cluster defined.

METHANOL FORMATION AFTER HOMOLYTIC AND FENTON-TYPE ACTIVATION

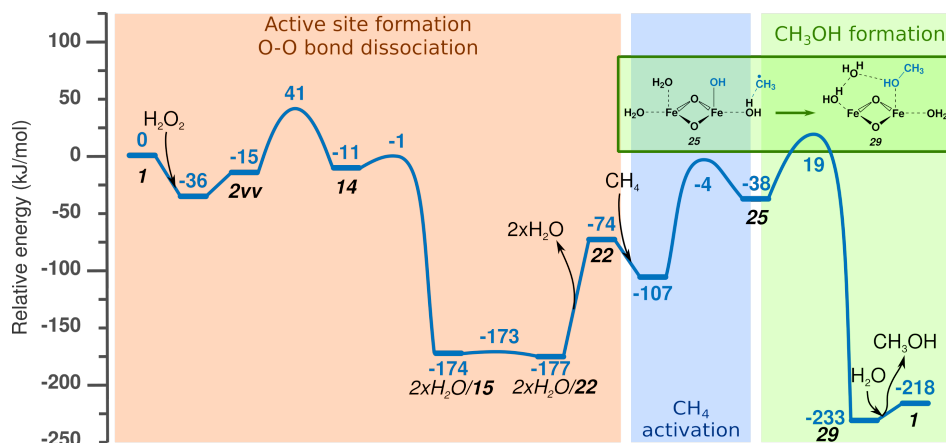


Figure 2.14: Reaction energy diagram of methane to methanol formation including the formation of the active site, homolytic C-H bond activation, the formation of CH_3OH and the active site regeneration.

The structures obtained after both the homolytic and Fenton-type pathways are similar in nature: they contain a CH_3 radical and an Fe(III)Fe(IV) cluster. Figure 2.14 shows the formation of methanol from structure **25**, which is the result of the combination of the CH_3 radical with an OH group of the Fe cluster. The reaction step requires 57 kJ/mol activation energy, and it has a reaction energy of -195 kJ/mol. With the substitution of the methanol by one water molecule we obtain the initial structure **1**.

METHYL-HYDROPEROXIDE FORMATION AND H_2O_2 DECOMPOSITION

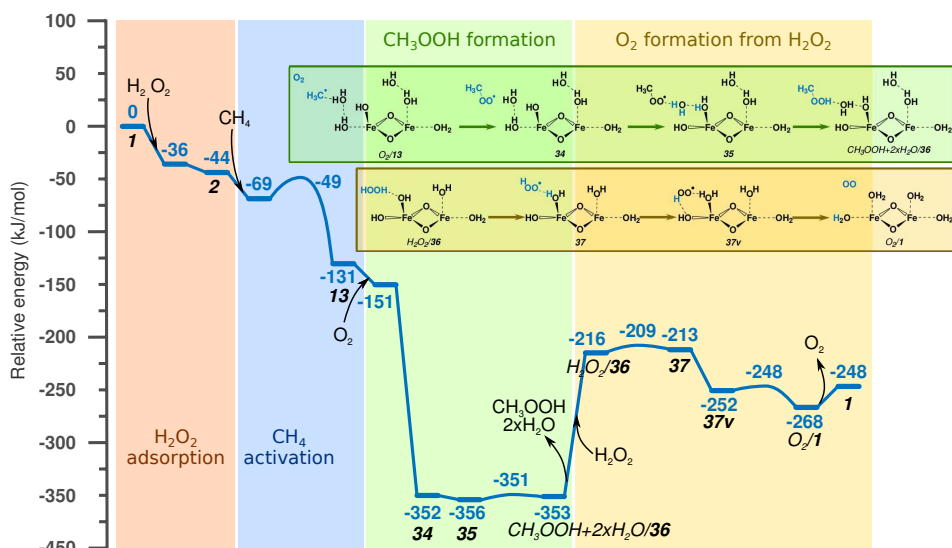


Figure 2.15: Reaction energy diagram of methane to CH_3OOH formation including the formation of the active site, Fenton-type C-H bond activation, the formation of CH_3OOH and the active site regeneration by H_2O_2 decomposition to O_2

If CH_3 radicals are present in the liquid phase, the formation of MeOOH is also possible. A potential pathway is illustrated on Figure 2.15. CH_3OOH formation starts with structure **13** where a CH_3 radical is formed via the Fenton-type homolytic dissociation of methane. The first step of the reaction is the adsorption of O_2 in the zeolite. O_2 is present in water, and it is also formed during the side reaction of H_2O_2 decomposition to H_2O and O_2 . The O_2 and CH_3 radical favourably combines to form an MeOO radical (**34**) with an energy gain of -201 kJ/mol. In the next step there is a H transfer between the Fe-OH and Fe- OH_2 ligands (**35**) for the H atoms to get into more favourable position for the water assisted H transfer to MeOO to yield MeOOH ($\text{CH}_3\text{OOH}+2x\text{H}_2\text{O}/36$). As expected this reaction has only a few kJ/mol activation barrier, and is thermodynamically neutral. Compared to MeOH , the formation of

MeOOH is thermodynamically similar ($\Delta E(O_2/13 \rightarrow CH_3OOH + 2xH_2O/36) = -202$ kJ/mol vs $\Delta E(25 \rightarrow 29) = -195$ kJ/mol). The limiting factor is the O_2 concentration in solution compared to the Fe-OH groups or framework O atoms close to the sites of formation of CH_3 radicals.

To regenerate the initial site, complex **36** needs to be reduced. There are two reducing agents in the system: CH_4 and H_2O_2 . It means that the active site might cleave a second C-H bond, or oxidise H_2O_2 to two $[H^+]$ ions and an O_2 molecule. The latter option is illustrated in Figure 2.15. Starting from $CH_3OOH + 2xH_2O/36$, MeOOH and two uncoordinated H_2O molecules are desorbed, and H_2O_2 is adsorbed. The first step is the abstraction of one H atom from the H_2O_2 molecule and the formation of an OOH radical (**37**). The second H atom is then abstracted after the rearrangement of the OOH radical, which comes with -39 kJ/mol energy gain due to the formation of a H-bonding interaction (**37v**). The reaction yields the initial site (O_2/I). The total reaction energy of O_2 formation from H_2O_2 is -52 kJ/mol and the activation barrier of both H atom abstractions is less than 10 kJ/mol.

Both the $H_2O_2 \rightarrow O_2 + 2[H^+]$ and the $CH_4 \rightarrow CH_3 + [H]$ reactions occur on the same Fe(IV)-oxo species. This means that H_2O_2 and CH_4 are competing for the same sites. Since the activation barrier of H_2O_2 oxidation is significantly lower than the barrier of the C-H bond dissociation and usually H_2O_2 concentration is significantly higher than that of methane, the dissociation of H_2O_2 will be favoured over methane. This renders the usage of H_2O_2 impractical for methane activation in combination with high valent Fe-oxo catalysts.

The total reaction energy of methanol and methyl hydroperoxide formation on Figure 2.13, 2.14 and 2.15 are not directly comparable due to the removal of the physically adsorbed H_2O molecules in Figure 2.13 and 2.14, and the adsorption of O_2 in Figure 2.15. We can however make an estimation for example from Figure 2.14 by subtracting the desorption energy of the previously removed H_2O molecules ($\Delta E = 103$ kJ/mol) and adding the adsorption energy of O_2 ($\Delta E = -20$ kJ/mol). This gives: $\Delta E(I \rightarrow 2xH_2O + O_2/29) \approx -233 - 123 = -356$ kJ/mol, which is comparable to the reaction energy for the alternative reaction channel $\Delta E(I \rightarrow CH_3OOH + 2xH_2O/36) = -353$ kJ/mol. However the calculations indicate that the formation of MeOOH is kinetically more favourable than the formation of MeOH (following the Fenton-type or homolytic C-H bond dissociation) as the direct rebound of CH_3 radical with an OH group proceeds with a barrier of $E^\ddagger \sim 60$ kJ/mol, while the recombination of the CH_3 radical with an O_2 molecule is a barrierless reaction and the only barrier on the path to methyl hydroperoxide is associated with the H atom abstraction and our calculations predict

it to be very small ($E^\ddagger = 5$ kJ/mol). Comparison with experimental data is difficult due to the complexity of the reaction network and the potential decomposition of MeOOH to MeOH [17] and to $\text{H}_2\text{COH}_2\text{CO}$ [10] and *in situ* analysis of the reaction mixture is not available. A batch reaction study performed by Hutchings [17] *et al.* shows that at the beginning of the reaction the selectivity towards MeOOH is high (~60%), and it gradually decreases during the course of the reaction. This supports the kinetic preference of the MeOOH formation over MeOH.

2.4. CONCLUSIONS

DIFFERENT reaction paths for the selective methane oxidation over a binuclear Fe site deposited in ZSM-5 zeolite were studied by periodic DFT calculations. The whole reaction cycle was investigated, which includes the formation of the active site, CH_4 activation, product formation and the regeneration of the initial site. Special attention was donated to the rate determining C-H bond dissociation step, the possibility of multiple mechanisms, and the influence of the different active sites on them was investigated. These were (1) heterolytic, (2) homolytic and (3) Fenton-type activation.

This study demonstrates that the system cannot be reduced to a single-site single-cycle concept. Even with the simplification to a single-type of Fe cluster at a given position of the zeolite framework the formation of multiple types of active sites are possible catalysing three mechanistically different C-H bond activations.

The possibility of the formation of different Fe(III) and Fe(IV) clusters upon reaction with H_2O_2 was demonstrated. These sites were proven to be catalytically active. Fe(III) was established to promote the heterolytic and Fenton-type reaction, while Fe(IV) the homolytic.

We found that the geometry of the Fe complex significantly influences the reaction energy, but not the barrier of the heterolytic C-H bond activation. The calculations indicate, that the type of activating O (Fe=O, Fe- μ O-Fe or Fe-OH) is unimportant from energetic point of view for both type of activation. We also found that confinement of the zeolite has a significant effect on the reaction step.

Methanol can be formed following all types of C-H bond activation via the recombination of CH_3 and an OH ligand reducing the active site. If the C-H bond was previously heterolytically cleaved, this step can either precede or follow the oxidation of the active site by the peroxo bond cleavage. After homolytic and Fenton-type dissociation this reduction step restores the initial oxidation state of the active site. MeOOH can be

obtained from the reaction of CH_3 radical and O_2 molecule followed by the abstraction of a H atom from the active site. After this step the Fe site is in the oxidized form available for further CH_4 oxidation.

Since the reaction is accompanied by the excessive consumption of H_2O_2 , its decomposition was also investigated. We found that the same Fe(IV)-oxo sites promote both the oxidation of H_2O_2 and CH_4 . The first reaction will be dominant as the activation barrier for the O-H bond cleavage is significantly lower than for C-H bond. This is why we propose H_2O_2 to be unsuitable oxidant in combination with high valent Fe clusters.

REFERENCES

- [1] A. E. Shilov and G. B. Shul'pin, *Chem. Rev.*, 1997, **97**, 2879–2932.
- [2] C. Copéret, *Chem. Rev.*, 2010, **110**, 656–680.
- [3] J. M. Mayer, *Acc. Chem. Res.*, 2011, **44**, 36–46.
- [4] A. A. Latimer, A. R. Kulkarni, H. Aljama, J. H. Montoya, J. S. Yoo, C. Tsai, F. Abild-Pedersen, F. Studt and J. K. Nørskov, *Nat. Mater.*, 2017, **16**, 225–229.
- [5] H. Aljama, J. K. Nørskov and F. Abild-Pedersen, *J. Phys. Chem. C*, 2017, **121**, 16440–16446.
- [6] *Iron Catalysis: Fundamentals and Applications.*, ed. B. Plietker, WILEY-VCH Verlag GmbH & Co. KGaA, Weinheim, 2008.
- [7] J. J. Pignatello, E. Oliveros and A. MacKay, 2006, **36**, 1–84.
- [8] O. Pestovsky, S. Stoian, E. L. Bominaar, X. Shan, E. Münck, L. Que Jr. and A. Bakac, *Angew. Chem. Int. Ed.*, 2005, **44**, 6871–6874.
- [9] G. B. Shulpin and G. V. Nizova, *React. Kinet. Catal. Lett.*, 1992, **48**, 333–338.
- [10] G. V. Nizova, G. Süss-Fink and G. B. Shul'pin, *Chem. Commun.*, 1997, 397–398.
- [11] G. Süss-Fink, G. V. Nizova, S. Stanislas and G. B. Shul'Pin, *J. Mol. Catal. A Chem.*, 1998, **130**, 163–170.
- [12] N. Agarwal, S. J. Freakley, R. U. McVicker, S. M. Althahban, N. Dimitratos, Q. He, D. J. Morgan, R. L. Jenkins, D. J. Willock, S. H. Taylor, C. J. Kiely and G. J. Hutchings, *Science*, 2017, **358**, 223–227.
- [13] K. Yoshizawa, Y. Shiota, T. Yumura and T. Yamabe, *J. Phys. Chem. B*, 2000, **104**, 734–740.
- [14] M. F. Fellah and I. Onal, *J. Phys. Chem. C*, 2010, **114**, 3042–3051.
- [15] B. D. Montejo-Valencia, Y. J. Pagán-Torres, M. M. Martínez-Iñesta and M. C. Curet-Arana, *ACS Catal.*, 2017, **7**, 6719–6728.
- [16] G. Li, E. A. Pidko, R. A. Van Santen, C. Li and E. J. M. Hensen, *J. Phys. Chem. C*, 2013, **117**, 413–426.
- [17] C. Hammond, M. M. Forde, M. H. Ab Rahim, A. Thetford, Q. He, R. L. Jenkins, N. Dimitratos, J. A. Lopez-Sanchez, N. F. Dummer, D. M. Murphy, A. F. Carley, S. H. Taylor, D. J. Willock, E. E. Stangland, J. Kang, H. Hagen, C. J. Kiely and G. J. Hutchings, *Angew. Chem. Int. Ed.*, 2012, **51**, 5129–5133.
- [18] G. Kresse and J. Hafner, *Phys. Rev. B*, 1993, **47**, 558–561.
- [19] G. Kresse and J. Hafner, *Phys. Rev. B*, 1994, **49**, 14251–14269.
- [20] G. Kresse and J. Furthmüller, *Phys. Rev. B Condens. Matter Mater. Phys.*, 1996, **54**, 11169–11186.
- [21] G. Kresse and J. Furthmüller, *Comput. Mater. Sci.*, 1996, **6**, 15–50.
- [22] J. P. Perdew, K. Burke and M. Ernzerhof, *Phys. Rev. Lett.*, 1996, **77**, 3865–3868.
- [23] J. P. Perdew, K. Burke and M. Ernzerhof, *Phys. Rev. Lett.*, 1997, **78**, 1396.
- [24] P. Blöchl, *Phys. Rev. B*, 1994, **50**, 17953–17979.

- [25] G. Kresse, *Phys. Rev. B Condens. Matter Mater. Phys.*, 1999, **59**, 1758–1775.
- [26] S. Grimme, J. Antony, S. Ehrlich and H. Krieg, *J. Chem. Phys.*, 2010, **132**, 154104.
- [27] H. J. Monkhorst and J. D. Pack, *Phys. Rev. B*, 1976, **13**, 5188–5192.
- [28] G. Mills, H. Jónsson and G. K. Schenter, *Surf. Sci.*, 1995, **324**, 305–337.
- [29] N. Hansen, A. Heyden, A. T. Bell and F. J. Keil, *J. Phys. Chem. C*, 2007, **111**, 2092–2101.
- [30] P. Belanzoni, L. Bernasconi and E. J. Baerends, *J. Phys. Chem. A*, 2009, **113**, 11926–11937.
- [31] R. Y. Brogaard and U. Olsbye, *ACS Catal.*, 2016, **6**, 1205–1214.
- [32] E. A. Pidko and R. A. Van Santen, *J. Phys. Chem. C*, 2009, **113**, 4246–4249.
- [33] B. Ensing Jr., F. Buda, P. Blöchl and E. J. Baerends, *Angew. Chem. Int. Ed.*, 2001, **40**, 2893–2895.
- [34] F. Buda, B. Ensing, M. C. M. Gribnau and E. J. Baerends, *Chem. Eur. J.*, 2001, **7**, 2775–2783.

3

METHANE OXIDATION OVER FE-MIL-53(Al) – ANALYSIS OF OVEROXIDATION AND H₂O₂ DECOMPOSITION PATHWAYS

Reaction paths underlying the catalytic oxidation of methane with H₂O₂ over Fe-MIL-53(Al) metal-organic framework were studied by periodic DFT calculations. Not only the activation of methane, but the full reaction network was considered, which includes the formation of the active site, the overoxidation of methane to CO₂ and the decomposition of H₂O₂ to H₂O and O₂. Calculations indicate, that the activation barrier for the initial activation of the Fe sites upon reaction with H₂O₂ is comparable to that of the subsequent C-H activation and also of the reaction steps involved in the undesirable overoxidation processes. The pronounced selectivity of the oxidation reaction over MIL-53(Al,Fe) towards the target mono-oxygenated CH₃OH and CH₃OOH products is attributed to the limited coordination freedom of the Fe species encapsulated in the extended octahedral [AlO₆] structure-forming chains, which effectively prevents the direct overoxidation paths prior to product desorption from the active sites. Importantly, our computational analysis reveals that the active sites for the desired methane oxidation are able to much more efficiently promote the direct catalytic H₂O₂ decomposition reaction, rendering thus the current combination of the active site and the reactants undesirable for the perspective methane valorization process.

This chapter is based on the following publications: Á. Szécsényi, G. Li, J. Gascon, and E. A. Pidko, Unraveling reaction networks behind the catalytic oxidation of methane with H₂O₂ over a mixed-metal MIL-53(Al,Fe) MOF catalyst, *Chemical Science*, **9** (2018) 6765-6773.; D. Osadchii, A. I. Olivos-Suarez, Á. Szécsényi, G. Li, M. A. Nasalevich, A. I. Dugulan, P. Serra-Crespo, E. J. M. Hensen, S. L. Veber, M. V. Fedin, G. Sankar, E. A. Pidko, and J. Gascon, Isolated Fe sites in Metal Organic Framework catalyze the direct conversion of methane to methanol, *ACS Catalysis*, **8** (2018) 5542-5548.

3.1. INTRODUCTION

DESPITE the impressive progress made in the last decade in understanding the fundamentals of C-H activation and revealing crucial structure-activity relationships for this pivotal reaction step, there is much less insight into the mechanistic factors that influence other steps of the catalytic methane oxo-functionalization cycle as well as the numerous competing reaction channels that do not determine the rate of the target methane activation but all contribute potentially to the decreased selectivity of the target process. In particular, the formation of the actual reaction centre capable of C-H cleavage and, related, the activation of the oxidant molecule are much less understood than the C-H dissociation step. Given the crucial role of these secondary processes for the overall efficiency of the catalytic methane oxidation, a systematic approach to the mechanistic analysis of the underlying reaction networks is highly desirable.

An inspiration to solving the selectivity problem in methane oxidation can be obtained from Nature. Methanotropic bacteria evolved to promote this reaction with a high efficiency[1]. They utilize very effective and complex enzymatic systems, called methane monooxygenases (MMO) to ensure a high selectivity of the methane oxidation process. The natural systems prevent the overoxidation reactions by providing a steric hindrance to the CH₃OH product formed at the MMO active site. The catalytic ensemble of MMOs contains Fe or Cu centres that activate molecular O₂ to create the highly reactive oxygen species capable of cleaving the C-H bonds in methane. Indeed, O₂ is the greenest, cheapest, most abundant and desirable oxidant for any industrial oxidation process. However the controlled utilization of O₂ for a selective chemo-catalytic oxidation mediated by transition metal complexes is very challenging. Such an oxidation process is fundamentally hampered by (a) the need to transfer 4 electrons to O₂ molecule and (b) the need to change the spin configuration of the system from triplet to singlet along the reaction[2] as it is elaborated in Chapter 1. That is why even the MMO systems show only a limited efficiency in terms of O₂ utilization, from which only one oxygen atom is incorporated into the CH₃OH product, while the other one is consumed to form H₂O by stoichiometric co-reductants NADH and FADH₂. These reactants supply electrons and protons necessary for the overall biological process to proceed under very mild conditions.

In chemo-catalysis, zeolites are often regarded as the synthetic mimics to enzymatic systems. Besides the nature of the metal and the type of oxidant, the topology of the confinement matrix, the nuclearity of the intra-zeolite active sites and the oxidation state of the reactive metal centres were found to be important factors affecting the activity and selectivity of the zeolite-based oxidation catalysts[3–5]. In the context of

the chemo-catalytic conceptual mimic of the enzymatic process, the development of an integrated catalyst system employing different co-reductants including H_2 to promote the activation of O_2 oxidant has been discussed in the literature[6]. However, the performance of such integrated systems for methane oxofunctionalization fell short for industrial application. To circumvent the problem of simultaneous use of the stoichiometric oxidant and reductant for methane oxidation, it was proposed to split the partial reduction of O_2 and the CH_4 oxidation steps and utilize H_2O_2 as the partially reduced oxidant in the latter step [7, 8]. Such a process has been realized experimentally by Hutchings[9] *et al* as it is elaborately described in Chapter 1, just as the main limitations of transition metal-containing zeolite-based catalysts, and why metal-organic frameworks are potential alternatives.

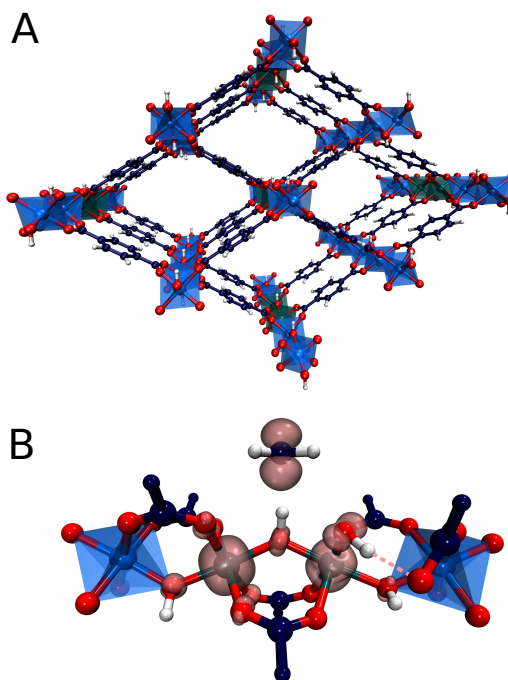


Figure 3.1: A) Fe_2 -MIL-53(Al) metal organic framework, containing dimeric Fe species substituting Al ions in the Al-O chain. B) Methyl radical formed upon C-H bond cleavage of methane by the bridging oxygen of the active site. Spin density is visualized at the isosurface of 0.1.

Recently, we reported that the introduction of isolated Fe species into the well-defined inorganic structure of an Al-terephthalate-based MOF gives rise to a MIL-53(Fe,Al) mixed-metal catalyst showing a high activity and selectivity in the oxidation of methane to methanol with H_2O_2 [10]. The parent MIL-53(Al) microporous MOF

matrix is made up of $[\text{AlO}_6]$ octahedral chains connected by 1,4-benzodicarboxylic acid struts to form well-defined 1D channels (Figure 3.1). The catalytic function can be introduced to this material by creating well-dispersed Fe sites inside these inorganic structure-forming chains. The extensive characterization of the catalysts revealed the predominant speciation of the reactive Fe as dimeric (Fe_2 -MIL-53(Al)) and monomeric (Fe_1 -MIL-53(Al)) complexes isomorphously substituting Al ions in the MIL-53 crystalline lattice. Such Fe sites are placed in a unique octahedral weak ligand field environment that is expected to be favourable for the C-H bond activation in methane[11, 12]. The isolated nature of the Fe sites in MIL-53(Fe,Al) is crucial for the structural stability of the material towards the oxidizing aqueous environment of the catalytic reaction.

The selectivity of the catalytic reaction did not exceed 85% due to overoxidation processes. Furthermore, the overall efficiency of the catalytic system towards methane oxidation was found to be limited by the competing direct H_2O_2 decomposition reaction to H_2O and O_2 . Therefore, to improve the efficiency and selectivity of the methane oxidation process, a control over these competing secondary reaction channels is needed, which cannot be achieved without a detailed understanding of the underlying mechanistic characteristics.

In this chapter we present the results of a comprehensive computational analysis of the reaction paths behind methane oxidation with H_2O_2 over MIL-53(Fe,Al) catalyst. The computational results presented here indicate promising routes for the optimization of the title selective oxidation process.

3.2. COMPUTATIONAL DETAILS

THE spin polarized periodic DFT calculations were carried out using the Vienna Ab Initio Simulation Package (VASP[13–16], version 5.3.5). PBE exchange-correlation functional[17, 18], plane wave basis set with a cut-off energy of 400 eV and the projector augmented wave (PAW) method[19, 20] were applied. To account for the van der Waals interactions Grimme's dispersion correction with Becke-Jonson damping (DFT-D3(BJ))[21] method was used. A Gaussian smearing of the population of partial occupancies with a width of 0.05 eV was used during iterative diagonalization of the Kohn-Sham Hamiltonian. Brillouin zone sampling was restricted to the Gamma point[22]. We have previously successfully employed this methodology for studying various zeolite-catalysed processes including chemical transformations in spin-polarized systems[23–25]. Convergence was assumed to be reached when the force on each atoms was below 0.04 eV Å⁻¹. Geometry optimization was completed for all considered spin states.

During the calculations, the supercell approach was applied, which means that the basic unit cell is multiplied by an integer, in this case 3 times to the x direction. The supercell catalyst model contained 228 atoms. Firstly, the lattice vectors of MIL-53(Al) were optimized, they were obtained to be orthogonal: $a = 20.917 \text{ \AA}$, $b = 17.808 \text{ \AA}$, $c = 12.216 \text{ \AA}$. To obtain the models of $\text{Fe}_1\text{-MIL-53(Al)}$ and $\text{Fe}_2\text{-MIL-53(Al)}$ one or two neighbouring Al atoms were substituted with Fe respectively. The geometries of the catalyst models as well as all the related intermediates and transition states were fully optimized with the cell parameters fixed to the values determined for the parent Al-form of MIL-53.

To locate the transition state structures, the nudged elastic band method (NEB)[26] was used. The maximum energy geometry along the reaction path generated by the NEB method was further optimized using a quasi-Newton algorithm. In this procedure, only the extra-framework atoms, and relevant framework atoms were relaxed. Vibrational frequencies were calculated using the finite difference method (0.02 \AA atomic displacements) as implemented in VASP. Transition state showed a single imaginary frequency corresponding to the reaction path.

Table 3.1: Relative energies of different spin states of structure 1. $S = 0$ is the antiferromagnetically coupled high spin state.

Spin state	ΔE (kJ/mol)
0	0
1	44
2	94
3	45
4	40
5	10

Dimeric Fe species substituting framework Al atoms were considered as the sites for methane oxidation. In line with the experimental results[10], DFT predicts the antiferromagnetically coupled high spin (AHS) state ($S = 0$) for the Fe pair to be the most stable one (Table 3.1). The ferromagnetic high spin (HS) configuration ($S = 5$) is however only 10 kJ/mol higher in energy. Spin density analysis shows that the absolute value of spin assigned to each atom in the $S = 0$ state is similar to those in the $S = 5$ state (for details see Table 3.2. The other intermediate spin states have a higher energy than $S = 5$ state (Table 3.1). In view of the difficulties in convergence of the antiferromagnetically coupled HS systems and given that according to Baerends[27] *et al.* a weak exchange coupling does not influence the chemical reactivity significantly, the reaction network analysis was further carried out over the HS potential energy

Table 3.2: The partial charge (calculated with the AIMS method) and the spin density of different spin states of the atoms of the active site of structure 1. O is the bridging oxygen, and H is the hydrogen atom connected to it.

	spin state	partial charge	spin
Fe1	0	1.75	4.02
	3	1.73	4.01
	4	1.61	2.80
	5	1.76	4.07
Fe2	0	1.74	-4.02
	3	1.49	1.15
	4	1.73	4.00
	5	1.76	4.07
O	0	-1.12	0.00
	3	-1.06	0.12
	4	-1.07	0.08
	5	-1.17	0.23
H	0	0.64	0.00
	3	0.60	0.00
	4	0.61	0.00
	5	0.64	0.01

Table 3.3: Spin densities of the Fe atoms of different spin states of different intermediates, and the relative energies of the structures compared to the S = 0 state. All structures are geometry optimized.

		S = 0	S = 5	S = 4
1	Fe1	4.02	4.07	2.80
	Fe2	-4.02	4.07	4.00
	ΔE	0	10	40
2	Fe1	4.01	4.02	
	Fe2	-3.97	4.07	
	ΔE	0	11	35
CH ₄ /3	Fe1	-3.04	3.20	3.16
	Fe2	3.02	3.97	3.17
	ΔE	0	95	18
4	Fe1	3.13	3.24	1.85
	Fe2	-3.96	4.02	4.01
	ΔE	0	13	6

surface. For further confirmation of the validity of this simplification we calculated the AHS state of several intermediates. The relative energies and spin densities are shown in Table 3.3. In this work we report relative electronic energies for elementary steps and activation energies computed as the difference of electronic energy of the computed structures.

3.3. RESULTS AND DISCUSSION

THE different conversion paths and competing cycles for methane and H_2O_2 conversion over Fe-MIL-53(Al) considered in this study are summarized in Figure 3.2. The oxidation cycles start with the catalyst activation (Figure 3.3 A) upon which the initial Fe(III)- μOH -Fe(III) site (**1**) is oxidized with H_2O_2 to form an Fe(IV)- μO -Fe(IV)-OH complex (**3**). This intermediate serves as the active site in all subsequent oxidation reactions (Cycle I, Figure 3.2) as well as in the competing H_2O_2 decomposition path (Cycle II, Figure 3.2). Cycle I depicts a sequential oxidation of methane to CO_2 with the intermediate formation of methanol, formaldehyde, formic acid or carbon monoxide. Each of the oxidation steps within the cycle involves the regeneration of the active complex (**3**) or a similar site (such as **8** or **15**) via oxidation with H_2O_2 . We identified two alternative reaction channels for both the methanol and formaldehyde oxidations with distinctly different reaction mechanism and intermediate products. Below we will first discuss the computational results obtained for each of the individual conversion steps and then use these data to analyse how the complete oxidation network operates and how it can be used to tailor the selectivity of methane oxo-functionalization process.

3.3.1. FORMATION OF THE ACTIVE SITE

The molecular mechanism of the active species generation and the respective DFT-computed energy diagram are summarized in Figure 3.3. The oxidation of the initial Fe(III) dimer with H_2O_2 starts with the physisorption of H_2O_2 in the pores of the MOF near the Fe centres ($\text{H}_2\text{O}_2/\mathbf{1}$). To proceed further along the reaction path, the coordination environment of the Fe centre has to be opened to allow for H_2O_2 coordination and activation. The intrusion of H_2O_2 can take place either via the cleavage of a bond with the bridging O (Fe- μO -Fe) (**2b**) or with the carboxylate linker O (Fe-OCRO) (**2**). Both reactions are thermodynamically unfavourable and show reaction energies of 79 and 49 kJ/mol ($E^\ddagger(\text{TS1}) = 77$ kJ/mol), respectively. The reaction $\text{H}_2\text{O}_2/\mathbf{1} \rightarrow \mathbf{2}$ is more favourable than reaction $\text{H}_2\text{O}_2/\mathbf{1} \rightarrow \mathbf{2b}$ rendering it more likely to occur during the catalytic process. The resulting coordinatively unsaturated Fe site promotes the coordination and the dissociation of H_2O_2 that is converted to an OH ligand bound to an Fe atom and a transient OH radical that readily abstracts an H atom from a bridging hydroxyl group to form an H_2O molecule during the same elementary reaction step ($\Delta E = -42$ kJ/mol, $E^\ddagger(\text{TS2}) = 34$ kJ/mol) ($\text{H}_2\text{O}/\mathbf{3}$). During this redox reaction step the oxygen atoms of H_2O_2 are reduced, while the Fe(III) sites are oxidized. Partial charge and spin density analysis (Table 3.4) indicates the equality of the two Fe(IV) centres. With the oxidation state of Fe the HS state also changes from $S = 5$ to $S = 4$, the spin-crossing transition takes place after the transition state (**TS2**). This step is

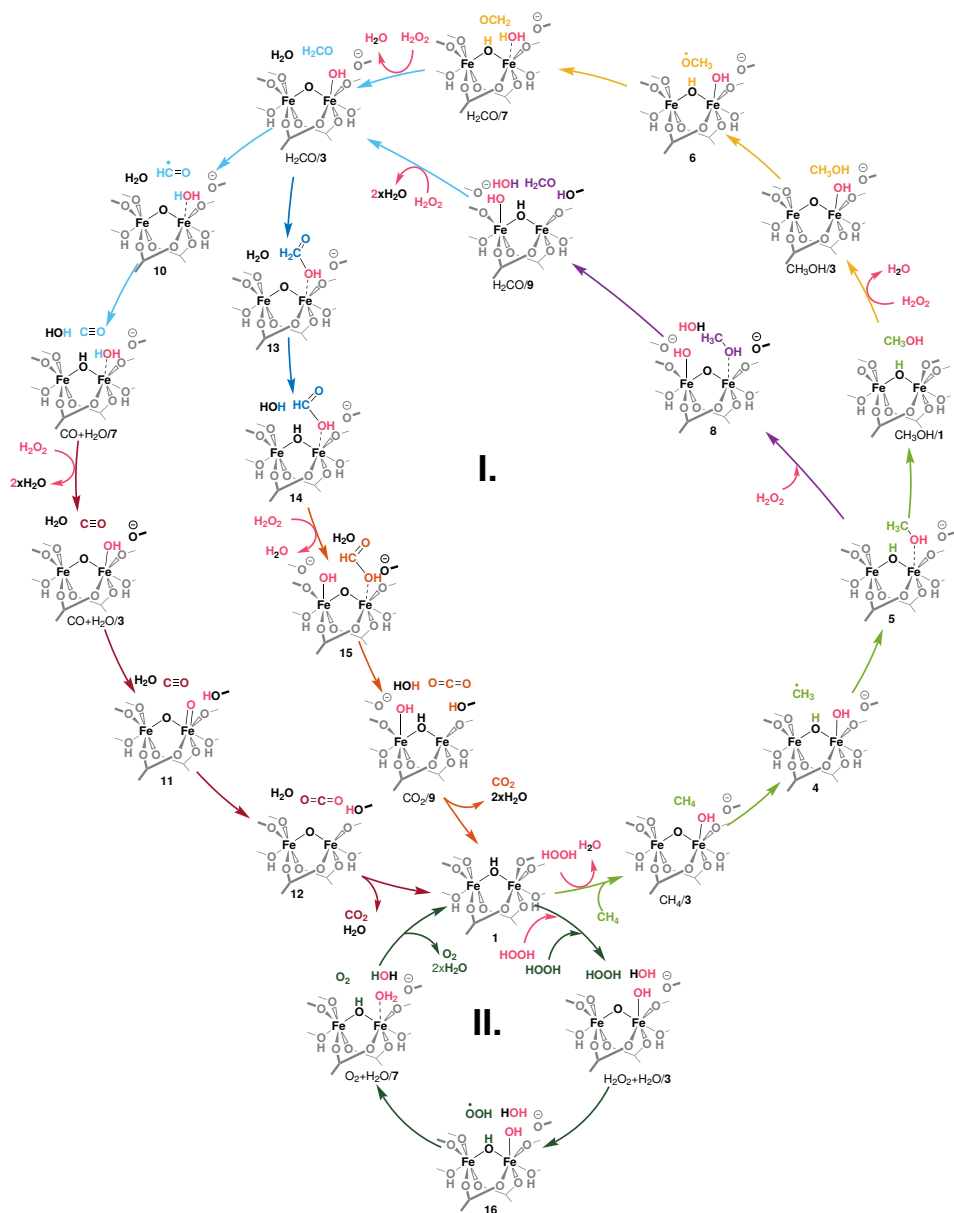


Figure 3.2: Reaction networks underlying the liquid phase methane oxidation with H₂O₂ by Fe₂ sites in MIL-53. The formation of the catalytic species **3** - the reaction of the reduced site **1** with H₂O₂ - is detailed on Figure 3.3 A. Cycle I. shows the oxidation of methanol to CO₂. Each colour indicates an oxidation step: light green: CH₄ → CH₃OH, yellow and purple: CH₃OH → CH₂O, light blue: CH₂O → CO, dark blue: CH₂O → HCOOH, brown: CO → CO₂, orange: HCOOH → CO₂. Cycle II. depicts the oxidation of a second H₂O₂ to O₂ and and formation of H₂O. All oxidation reactions occur over the same active site (**3**).

exothermic with the calculated $\Delta E = -42$ kJ/mol, which effectively compensates for the energy losses associated with the initial Fe-OCRO cleavage step making the overall

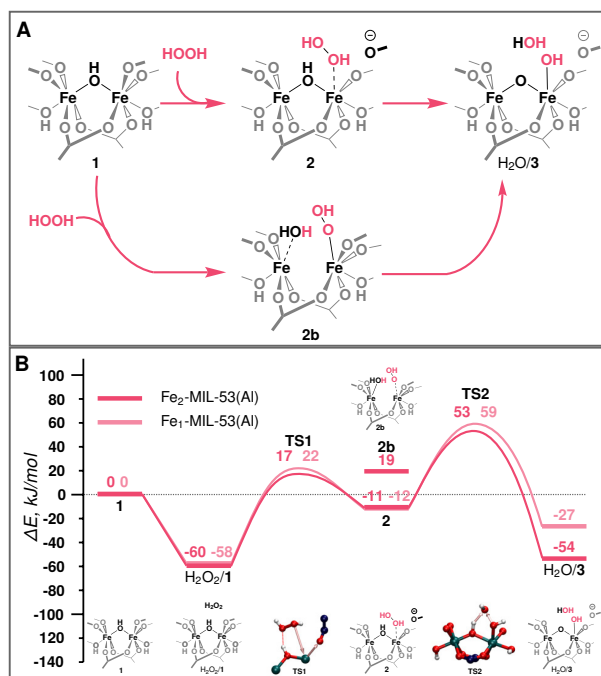


Figure 3.3: A) Schematic representation and B) reaction energy diagram of the formation of the active site over binuclear and mononuclear Fe species.

activation sequence thermodynamically neutral ($\Delta E(\text{H}_2\text{O}_2/1 \rightarrow \text{H}_2\text{O}/3) = 6 \text{ kJ/mol}$).

Table 3.4: Partial charge and spin density of Fe atoms in structure $\text{H}_2\text{O}/3$ ($S = 4$ spin state).

	Partial charge	Spin density
Fe1	1.71	3.15
Fe2	1.71	3.16

The increase of the number of Fe atoms in the reactive ensemble may result in a compromised stability of the framework towards the reactive environment. The Fe-rich structure has more sites potentially participating in the reaction with H_2O_2 that give rise to the formation of defect sites more susceptible to hydrolysis and further decomposition. This has been confirmed experimentally by showing that the pure MIL-53(Fe) samples disintegrate in the presence of H_2O_2 , while when sufficient site-isolation of Fe ions in MIL-53(Fe,Al) materials is ensured, no Fe leaching was observed[10].

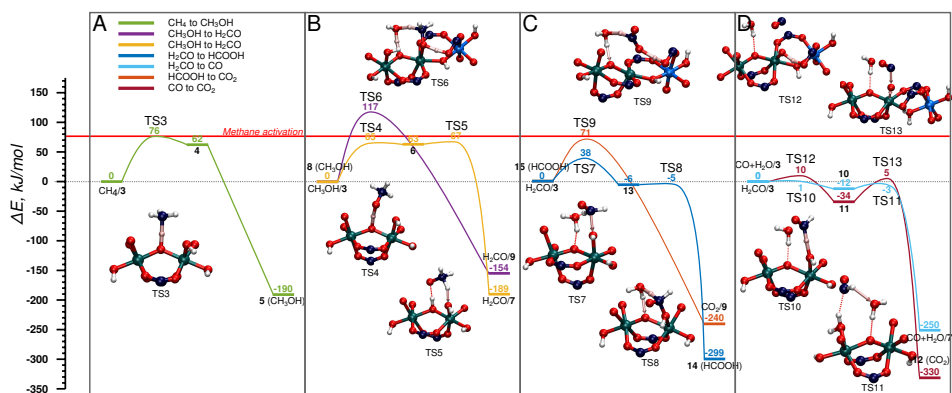


Figure 3.4: Energy diagram of cycle I, schematic representation is shown in Figure 3.2. A: CH₄ → CH₃OH, B: CH₃OH → CH₂O in two steps (yellow) and in one step (purple), C: H₂CO → HCOOH (dark blue), and its consecutive oxidation to CO₂ (orange), D: CH₂O → CO (light blue) and its consecutive oxidation to CO₂ (brown). The reference point for all reactions is the active site and the adsorbed molecule as represented in Figure 3.2.

3.3.2. METHANE OXIDATION AND OVEROXIDATION (CYCLE I)

The oxidized species **3** efficiently promotes methane to methanol oxidation[10]. The adsorbed methane is activated via a homolytic C-H cleavage over the bridging O centre to yield a bridging hydroxyl group and a CH₃ radical weakly coupled with the paramagnetic Fe dimer (**4**). The CH₃ radical formation is endothermic by 62 kJ/mol and proceeds with a barrier of only 76 kJ/mol. Upon the C-H cleavage step one proton and one electron are transferred from the methane to the active site and the cluster is reduced to Fe(IV)-Fe(III). Next, the CH₃ radical recombines with the neighbouring OH group to form a methanol molecule. The radical recombination is accompanied by the reduction of the second Fe(IV) atom to Fe(III) obtaining the initial oxidation state of the cluster (**5**). The release of methanol into the MIL-53 channels regenerates the initial closed Fe dimer site (CH₃OH/**1**).

Next CH₃OH is oxidized to H₂CO. The reaction involves an abstraction of two H atoms that can either occur concurrently, in which case methanol stays adsorbed on the Fe site, while it is being oxidized again by H₂O₂, or consecutively, which means that the methanol encounters another active site in the MOF (Figure 3.4 B). In the concurrent case (purple) (E[‡](TS6) = 117 kJ/mol) the transfer of three H atoms takes place simultaneously: one C-H bond of CH₃OH dissociates, and the carboxylic O accepts the H atom. At the same time, the OH group of CH₃OH is also deprotonated by the bridging O with an H₂O molecule acting as a H atom shuttle. Co-adsorbed water molecule accepts a H atom from methanol and simultaneously transfers one of its own to the bridging O (H₂CO/**9**). In the alternative path (yellow path in Figure 3.4 B), the methanol is converted to CH₂O in two steps via a CH₃O radical intermediate.

This reaction proceeds via an outer-sphere mechanism, in which CH_3OH is not coordinated to the Fe centres during the reaction. At first the O-H bond is cleaved by the bridging O ($E^\ddagger(\text{TS4}) = 65 \text{ kJ/mol}$) and the CH_3O radical is formed (**6**). It is followed by an almost barrierless ($E^\ddagger(\text{TS5}) = 4 \text{ kJ/mol}$) C-H bond dissociation by a neighbouring Fe-OH moiety to form a coordinated H_2O molecule and formaldehyde ($\text{H}_2\text{CO}/7$). We previously showed, that the release of methanol to the MOF pore and the regeneration of the original site (reaction **5** \rightarrow $\text{CH}_3\text{OH}/1$) is a thermodynamically favourable reaction (shown on Figure 3.5. A). This together with a relatively high activation barrier predicted for the one-step mechanism suggest that the conversion of methanol to formaldehyde should take place on an Fe site different from the one where it was originally formed.

In the next step H_2CO is oxidized to CO_2 . The oxidation can proceed via HCOOH (Figure 3.4 C) or CO (Figure 3.4 D) intermediate. The former $\text{H}_2\text{CO} \rightarrow \text{HCOOH}$ route ($\text{H}_2\text{CO}/3 \rightarrow 14$) is a two-step process (Figure 3.4 C), in which first an H_2COOH complex is formed by the addition of H_2CO to an OH group of the active site (**13**) ($E^\ddagger(\text{TS7}) = 38 \text{ kJ/mol}$) in a slightly exothermic reaction followed by the almost barrierless ($E^\ddagger(\text{TS8}) = 1 \text{ kJ/mol}$) water assisted C-H bond dissociation yielding HCOOH (**14**). HCOOH is then oxidized to CO_2 (**15** \rightarrow $\text{CO}_2/9$) in a one-step water assisted transfer of two H atoms to a carboxylic linker O and the bridging O centre ($E^\ddagger(\text{TS9}) = 71 \text{ kJ/mol}$).

The other path to convert H_2CO to CO_2 proceeds via CO as an intermediate and it is shown in Figure 3.4 D. This path starts with the oxidation of H_2CO to CO ($\text{H}_2\text{CO}/3 \rightarrow \text{CO} + \text{H}_2\text{O}/7$) by a two-step H-abstraction process. The first H atom is accepted by the OH group ($E^\ddagger(\text{TS10}) = 1 \text{ kJ/mol}$) forming H_2O and CHO radical (**10**). The second transition state ($E^\ddagger(\text{TS11}) = 12 \text{ kJ/mol}$) is associated with the rotation of the HCO radical around the C-O axis, which is followed by the cleavage of the C-H bond. The nearby H_2O molecule acts as an H shuttle accepting the H atom and donating its own to the bridging O site ($\text{CO} + \text{H}_2\text{O}/7$). CO is further oxidized to CO_2 via $\text{CO} + \text{H}_2\text{O}/3 \rightarrow 12$. In the first step, a H atom is transferred from the OH group to the carboxylate ligand to form a terminal oxo-species (**11**) in a slightly exothermic reaction ($E^\ddagger(\text{TS12}) = 10 \text{ kJ/mol}$). The terminal O-site acts then as the oxidizing centre to convert CO to CO_2 (**12**) ($E^\ddagger(\text{TS13}) = 39 \text{ kJ/mol}$).

These reactions in terms of proton and electron transfer can be classified into 1) 2 H atom transfer from the molecule to the active site ($\text{CH}_3\text{OH} \rightarrow \text{CH}_2\text{O}$, $\text{CH}_2\text{O} \rightarrow \text{CO}$, $\text{HCOOH} \rightarrow \text{CO}_2$), 2) 1 H atom transfer to the active site and an OH group from the active site to the reactant ($\text{CH}_4 \rightarrow \text{CH}_3\text{OH}$, $\text{CH}_2\text{O} \rightarrow \text{HCOOH}$) or 3) O atom transfer from the active site ($\text{CO} \rightarrow \text{CO}_2$). The formal oxidation state of C increases by two with

each step from -4 of CH₄ to +4 of CO₂. This requires the reduction of 4 H₂O₂ molecules. The reduction of the H₂O₂ and the oxidation of the (oxygenated) hydrocarbons is decoupled with the help of the Fe site. Fe(III) is oxidized by the H₂O₂ to Fe(IV) which is reduced again by the hydrocarbon to Fe(III). With the oxidation state of the Fe cluster the HS state also changes: Fe(III) dimer is in S = 5, while Fe(IV) dimer is in the S = 4 HS state.

3

The calculations indicate, that it is not likely that the methane is overoxidized while being adsorbed to the active site, as the release of methanol to the MOF pore and the regeneration of the initial Fe cluster is strongly favourable thermodynamically. Therefore, we propose that the further transformation of methanol should take place on an active site different from that where it was originally formed. Furthermore, the comparison of the computed energetics for the overoxidation steps suggests that the oxidation of CH₃OH and HCOOH proceeds with activation barriers similar to that of the initial methane activation despite the considerably lower C-H bond energies in the former molecules. This provides a fundamental possibility to obtain methanol as the kinetic product with a good selectivity. The low activation energies predicted for CH₂O and CO conversions indicate a very short life-time of these intermediates in line with the experimental observations[10].

3.3.3. H₂O₂ DECOMPOSITION (CYCLE II) VS CH₄ OXIDATION

When H₂O₂ is used as the oxidant, the target methane oxidation process is inevitably accompanied by the direct decomposition of H₂O₂. The computed reaction energy diagrams for this process are shown in Figure 3.5 A.

After the formation of the active site (H₂O/3,) a second H₂O₂ molecule is adsorbed in the pore of MOF catalyst (H₂O₂+H₂O/3). This is followed by the deprotonation of H₂O₂ by the bridging O site to form an OOH radical intermediate (**16**) (ΔE = -43 kJ/mol, E[‡](TS14) = 14 kJ/mol). The radical reacts then with an Fe-OH moiety to form molecular O₂ (O₂+H₂O/7) (ΔE = -83 kJ/mol, E[‡](TS15) = 1 kJ/mol). The active site is regenerated by the decoordination of an H₂O ligand and the formation of the Fe-OCRO bond (O₂+H₂O/1) (ΔE = -16 kJ/mol, E[‡](TS16) = 45 kJ/mol). During the course of the reaction the oxidation state of Fe and O atoms changes in two steps. Each step has a different HS state. The HS of the oxidized active site **3** is S = 4. After **TS14** Fe(III)-Fe(IV) cluster and a radical is formed, HS state of **16** becomes S = 5. In the next step O₂ is formed, and Fe is further reduced to Fe(III)-Fe(III) (O₂+H₂O/7). The HS state of the Fe(III)-Fe(III) cluster is S = 5, however the total spin of the system will be S = 6 due to the triplet state of the molecular oxygen product.

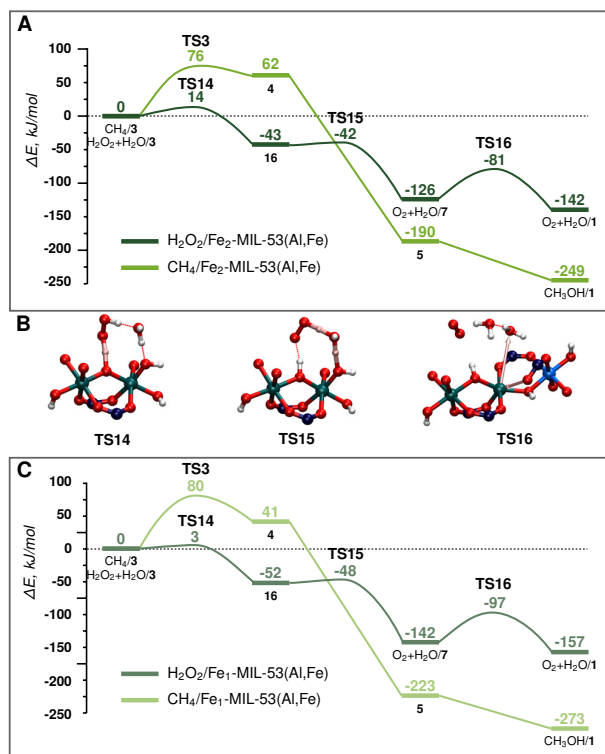


Figure 3.5: Energy diagram of H₂O₂ decomposition towards O₂ (dark green) and CH₄ oxidation towards CH₃OH (light green) over A: Fe₂-MIL-53(Al) and C: Fe₁-MIL-53(Al). B shows the transition states for part A H₂O₂ decomposition. The reference point is the active site and the adsorbed H₂O₂ or CH₄ molecule as represented in Figure 3.2.

The same active site (3) promotes the oxidation of both CH₄ and H₂O₂. To facilitate the comparison of the two paths, both energy diagrams are shown in Figure 3.5 A. Although thermodynamically the formation of CH₃OH is preferred, the undesirable H₂O₂ decomposition proceeds with a barrier of more than 60 kJ/mol lower than the C-H bond activation. This implies that the conversion of H₂O₂ is strongly kinetically favoured over the methane activation. The latter path can in principle be promoted at a lower concentration of hydrogen peroxide. However, H₂O₂ is necessary to generate the active site for methane oxidation, and the barrier for the active site formation is similar to that determined for CH₄ activation, suggesting that this selectivity enhancement will always be achieved at the expense of the decreased reaction rate.

3.3.4. MONONUCLEAR FE SITES

Characterization of the catalyst suggests that a considerable portion of the Fe sites in the mixed-metal MIL-53(Fe,Al) catalyst are monomeric complexes. The main difference between the monomeric and dimeric Fe sites is in the formal oxidation

state. The reduction of H₂O₂ requires two electrons from the Fe centre. This implies that such a reaction over the dimeric species will oxidise both Fe sites to +4 state, while for the monomeric site, the oxidized Fe is in the +5 state (light pink line of Figure 3.3 B). The formation of the mononuclear +5 species is thermodynamically less favourable than the oxidation of the binuclear cluster ($\Delta E(\mathbf{3}\text{-monomer}) - \Delta E(\mathbf{3}\text{-dimer}) = 27 \text{ kJ/mol}$). Nevertheless, the mononuclear Fe site still provides favourable reaction channels for the active site formation and the oxidation of methane to methanol (energy diagram in Figure 3.3 B, and Figure 3.5 C). Importantly, we find here that this mononuclear site also promotes the H₂O₂ decomposition. The associated two H-abstraction process in this case proceeds with less than 4 kJ/mol activation barrier each, following the same trend as that described for the binuclear active site above.

These results indicate that the behaviour of the mononuclear Fe site in MIL-53 structure is similar to that of the binuclear Fe clusters. This implies that the coordination sphere (geometry and quality of the ligands) of the Fe has a more significant influence on the reactivity than the nuclearity of the complex.

3.4. CONCLUSIONS

THE conversion of methane to methanol over mixed metal Fe-MIL-53(Al) catalyst was investigated by periodic DFT calculations. Other than the most important C-H bond activation step the whole catalytic cycle was explored and different reaction paths were identified for the formation of the active site and the overoxidation of methane towards CO₂. An important side reaction, the decomposition of H₂O₂ to O₂ and H₂O was investigated. The reactivity of mononuclear and binuclear Fe species was compared. As expected the calculations reveal a highly complex reaction network with many possibilities. Our main findings can be outlined as follows.

(i) Methanol can be yielded with good selectivity as kinetic product of the reaction, as the consecutive oxidation of methane has a high activation barrier, and the desorption of methanol and the regeneration of the initial Fe site is thermodynamically favourable.

(ii) The first C-H bond dissociation of methane is only one of the rate determining steps. The reaction barrier that leads to the active site formation, the O-H bond dissociation of CH₃OH and the conversion of HCOOH is in the same order of magnitude. The oxidation of H₂CO and CO has a low reaction barrier indicating that these intermediates have a low concentration in the reaction mixture in line with experiments.

(iii) The same active site (3) promotes the oxidation of both CH_4 and H_2O_2 . The conversion of H_2O_2 is favoured over CH_4 as the reaction barrier of the former reaction is over 60 kJ/mol lower. This renders H_2O_2 unsuitable for methane oxidation in combination with Fe complexes.

(iv) The activity of mononuclear and binuclear sites were compared. The calculations indicate that despite monomeric species go through formal oxidation state of +5 in the reaction, while dimeric species are only oxidized until formal oxidation state +4, the activity of the species are comparable, and they promote the same reaction steps.

REFERENCES

- [1] D. Park and J. Lee, *Korean J. Chem. Eng.*, 2013, **30**, 977–987.
- [2] X. Liu, Y. Ryabenkova and M. Conte, *Phys. Chem. Chem. Phys.*, 2015, **17**, 715–731.
- [3] A. R. Kulkarni, Z.-J. Zhao, S. Siahrostami, J. K. Nørskov and F. Studt, *Catal. Sci. Technol.*, 2018, **8**, 114–123.
- [4] M. H. Mahyuddin, A. Staykov, Y. Shiota, M. Miyanishi and K. Yoshizawa, *ACS Catal.*, 2017, **7**, 3741–3751.
- [5] T. Z. H. Gani and H. J. Kulik, *ACS Catal.*, 2018, **8**, 975–986.
- [6] K. Otsuka and Y. Wang, *Appl. Catal., A*, 2001, **222**, 145–161.
- [7] G. B. Shulpin and G. V. Nizova, *React. Kinet. Catal. Lett.*, 1992, **48**, 333–338.
- [8] J. K. Edwards, B. Solsona, E. Ntainjua N, A. F. Carley, A. A. Herzing, C. J. Kiely and G. J. Hutchings, *Science*, 2009, **323**, 1037–1041.
- [9] C. Hammond, N. Dimitratos, J. A. Lopez-Sanchez, R. L. Jenkins, G. Whiting, S. A. Kondrat, M. H. Ab Rahim, M. M. Forde, A. Thetford, H. Hagen, E. E. Stangland, J. M. Moulijn, S. H. Taylor, D. J. Willock and G. J. Hutchings, *ACS Catal.*, 2013, **3**, 1835–1844.
- [10] D. Osadchii, A. Olivos Suarez, A. Szécsényi, G. Li, M. Nasalevich, A. Dugulan, P. Serra-Crespo, E. Hensen, S. Veber, M. Fedin, G. Sankar, E. Pidko and J. Gascon, *ACS Catal.*, 2018, **8**, 5542–5548.
- [11] A. Kazaryan and E. Baerends, *ACS Catal.*, 2015, **5**, 1475–1488.
- [12] G. Gopakumar, P. Belanzoni and E. Baerends, *Inorg. Chem.*, 2012, **51**, 63–75.
- [13] G. Kresse and J. Hafner, *Phys. Rev. B*, 1993, **47**, 558–561.
- [14] G. Kresse and J. Hafner, *Phys. Rev. B*, 1994, **49**, 14251–14269.
- [15] G. Kresse and J. Furthmüller, *Phys. Rev. B Condens. Matter Mater. Phys.*, 1996, **54**, 11169–11186.
- [16] G. Kresse and J. Furthmüller, *Comput. Mater. Sci.*, 1996, **6**, 15–50.
- [17] J. P. Perdew, K. Burke and M. Ernzerhof, *Phys. Rev. Lett.*, 1996, **77**, 3865–3868.
- [18] J. P. Perdew, K. Burke and M. Ernzerhof, *Phys. Rev. Lett.*, 1997, **78**, 1396.
- [19] P. Blöchl, *Phys. Rev. B*, 1994, **50**, 17953–17979.
- [20] G. Kresse, *Phys. Rev. B Condens. Matter Mater. Phys.*, 1999, **59**, 1758–1775.
- [21] S. Grimme, J. Antony, S. Ehrlich and H. Krieg, *J. Chem. Phys.*, 2010, **132**, 154104.
- [22] H. J. Monkhorst and J. D. Pack, *Phys. Rev. B*, 1976, **13**, 5188–5192.
- [23] C. Liu, G. Li, E. J. M. Hensen and E. A. Pidko, *J. Catal.*, 2016, **344**, 570–577.
- [24] G. Li, P. Vassilev, M. Sanchez-Sanchez, J. Lercher, E. J. M. Hensen and E. A. Pidko, *J. Catal.*, 2016, **338**, 305–312.
- [25] G. Li, E. A. Pidko, R. A. Van Santen, Z. Feng, C. Li and E. J. M. Hensen, *J. Catal.*, 2011, **284**, 194–206.
- [26] G. Mills, H. Jónsson and G. K. Schenter, *Surf. Sci.*, 1995, **324**, 305–337.
- [27] P. Belanzoni, L. Bernasconi and E. J. Baerends, *J. Phys. Chem. A*, 2009, **113**, 11926–11937.

4

SECONDARY EFFECTS IN METHANE ACTIVATION OVER FE-ZSM-5

Linear energy scaling laws connect the kinetic and thermodynamic parameters of key elementary steps for heterogeneously catalysed reactions over defined active sites on open surfaces. Such scaling laws provide a framework for a rapid computational activity screening of families of new catalysts, but they also effectively impose a fundamental limit on the theoretically attainable activity. Understanding the limits of applicability of the linear scaling laws is therefore crucial for the development of predictive models in catalysis. In this work, we investigate computationally the role of secondary effects such as confinement, flexibility and multifunctionality of the active site on the reactivity of well-defined Fe complexes in ZSM-5 zeolite towards methane oxofunctionalization. The computed C-H activation barriers over Fe-sites at different locations inside the zeolite pores generally follow the associated reaction enthalpies and the hydrogen affinities of the active site, reflecting the O-H bond strength. Nevertheless, despite the close similarity of the geometries and intrinsic reactivities of the considered active sites, substantial deviations from these linear scaling relations are apparent from the DFT calculations. We identify three major factors behind these deviations, namely, (1) confinement effects due to zeolite micropores, (2) coordinative flexibility of the active site, and (3) multifunctionality. The latter two phenomena impact the mechanism of the catalytic reaction by providing a cooperative reaction channel for the substrate activation or by enabling the stabilizing of the intrazeolite complex along the reaction path. These computational findings point to the need for the formulation of multidimensional property-activity relationships accounting for both the intrinsic chemistry of the reactive ensembles and secondary effects due to their environmental and dynamic characteristics.

4.1. INTRODUCTION

THE development of predictive models to guide and facilitate the discovery and optimization of catalysts for important chemical applications has been a central problem in catalysis research for decades [1]. The identification of representative equilibrium states that could be used as performance descriptors under the non-equilibrium conditions is one of the corner stones of modern catalysis research. Such descriptors reflect the intrinsic chemistry of the catalytic site and may be related to structural features [2], electronic properties [3] or thermodynamics [4]. Impressive progress has been made in the last decade in the development of universal scaling relationships that correlate linearly the barriers of elementary reaction steps with the binding or adsorption energies for key intermediates through Brønsted–Evans–Polányi (BEP) relationships [5–7]. Such linear relationships facilitate greatly the *in silico* search for an optimal catalyst and enable practical applications of machine learning algorithms in computational catalysis [8, 9] by significantly reducing the number of independent parameters that determine catalytic reactivity. Scaling relations provide a theoretical framework for constructing volcano plots from first principles and therefore put fundamental limits on the maximum achievable activity or selectivity for a particular catalyst class [10, 11].

A representative example of the universal scaling relationship is the linear correlation between the activation barrier for homolytic methane C-H bond activation and hydrogen affinity. The latter thermodynamic descriptor holds for various solid catalysts, ranging from transition metal surfaces to zeolites and oxides [12]. This correlation could allow for the large-scale computational screening of materials to identify new heterogeneous catalysts capable of efficiently promoting the oxidation of methane to methanol. Such a catalytic process could revolutionize the natural gas industry by providing a practical means for the one-site liquefaction and valorisation of small-scale remote sources [13–15]. A similar correlation between the reactivity of zeolites towards homolytic methane C-H bond cleavage and spin-density of the active oxygen site was also proposed for Cu/ZSM-5 zeolite [16, 17]. Snurr et al extended the linear scaling relationship to metal-organic framework (MOF) based catalysts and pointed out that the reactivity for methane C-H bond activation has a uniform correlation with the formation energy of the active oxygen site in 60 different MOF structures [18]. Despite the clear generality of these relationships provided by the major impact of the intrinsic chemistry of the active site on the reactivity, substantial deviations from the general trends of up to 70 kJ/mol could be seen in the reported general trends. Understanding the origin of these deviations may providedesign principles allowing to circumvent the associated fundamental limitations on the catalyst activity [19–22].

Secondary interactions with the active site environment are well known to affect the shape of the potential energy surface corresponding to the reaction and product states and thus provide a mechanism to break the primary scaling relations. These interactions are particularly important for catalytic reactions in microporous materials such as MOFs [23, 24] and zeolites [25–27]. Fe-containing zeolite and MOF systems are among the most promising catalysts for the selective C-H oxidation and their multinuclear cationic Fe-oxo/hydroxo complexes are often regarded as synthetic mimics of the methane monooxygenase enzyme [28–30]. In this study we investigate in detail how variations in the local environment of such binuclear Fe(IV) clusters deposited in the ZSM-5 zeolite matrix affect their reactivity towards homolytic C-H activation in methane. A detailed analysis of the factors leading to the deviation from the linear relationships was carried out. As a result, we identify the mechanisms that can be utilized in catalyst design towards enhanced reactivity beyond the fundamental limits of the scaling relations.

4.2. COMPUTATIONAL DETAILS

THE spin polarized periodic DFT calculations were carried out with the Vienna Ab Initio Simulation Package (VASP 5.3.5) [31, 32]. PBE exchange-correlation functional [33] was used together with the plane wave basis set with a kinetic energy cut-off of 450 eV and the projector augmented wave (PAW) method [34]. To account for the van der Waals interactions, the semiempirical Grimme's dispersion correction with Becke-Jonson damping (DFT-D3(BJ)) method was used [35]. A Gaussian smearing of the population of partial occupancies with a width of 0.05 eV was used during iterative diagonalization of the Kohn-Sham Hamiltonian. Brillouin zone sampling was restricted to the Gamma point. Convergence was assumed to be reached when the force on each atom was below 0.04 eV \AA^{-1} . The unit cell lattice parameters were optimized and fixed throughout the calculations ($a = 20.1 \text{ \AA}$, $b = 19.8 \text{ \AA}$, $c = 13.2 \text{ \AA}$, $\alpha = \beta = \gamma = 90^\circ$).

To locate the transition states, the climbing image nudged elastic band method (CI-NEB) [36] was applied. The maximum energy geometry along the reaction path generated by the NEB method was further optimized using a quasi-Newton algorithm. In this procedure, only the extra-framework atoms, and relevant framework atoms were relaxed. Vibrational frequencies were calculated using the finite difference method (0.02 \AA atomic displacements) as implemented in VASP. Transition state showed a single imaginary frequency corresponding to the reaction path.

The outer surface of the zeolite was simulated by using a periodic slab model. One unit cell of the zeolite was chosen, that was truncated in the z direction along the

ab surface. All terminal dangling O atoms were substituted with H atoms. A 20 Å vacuum was placed between the sheets of zeolite which is considered enough to have negligible interaction between the surface species and the next sheet of zeolite. Only Gamma point was used to sample the Brillouin zone.

All data analysis and discussion in this work have been done based on the relative electronic energies. This decision is elaborated on in the supporting information, where a series of test calculations for Gibbs free energy is presented. It was found that Gibbs free energy does not change the relative energies significantly. The calculations were carried out at the high spin (HS) potential energy surface. Although the most stable spin state is the antiferromagnetically coupled high spin state (AHS), it has been demonstrated that the reactivity of O-bridged Fe complexes is similar in the HS and AHS states [37]. An extensive justification was provided by Baerends et al [38].

4

4.3. RESULTS AND DISCUSSION

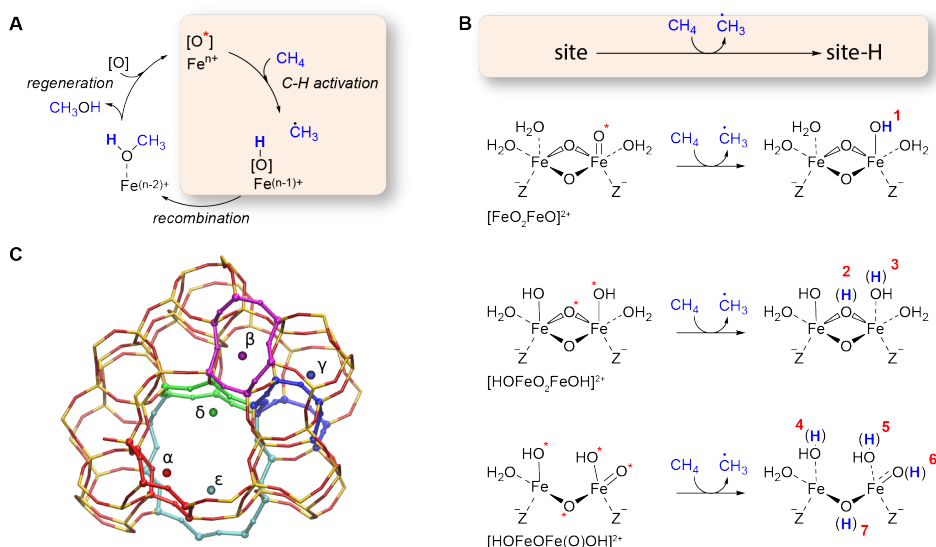


Figure 4.1: (A) The key steps of the catalytic oxo-functionalization of methanol over an oxygenated iron site representing (B) the three binuclear Fe catalytic sites ('site') featuring reactive oxygen sites (indicated with *) able to initiate the homolytic C-H cleavage in methane resulting in a $\cdot\text{CH}_3$ species and a partially reduced complex ('site-H'). The cationic di-Fe complex can be stabilized at (C) different extra-framework positions in the pores of ZSM-5 featuring versatile coordination and confinement environment.

THE rebound mechanism of methane oxidation by a Fe-O moiety is depicted in Figure 4.1. In this work we specifically focus on the first step of the catalytic cycle, the homolytic C-H bond activation over representative binuclear Fe sites (Figure 4.1 B).

The reactive sites in Fe/ZSM-5 take form of extra-framework binuclear Fe(IV) μ -oxo-bridged complexes with an octahedral coordination environment of the iron centres completed by the lattice oxygen, extra-framework terminal oxo and hydroxo- ligands and water molecules. The formation of such complexes upon oxidation of the stable $[(\text{H}_2\text{O})_2\text{-Fe(III)-}(\mu\text{-O})_2\text{-Fe(III)-}(\text{H}_2\text{O})_2]^{2+}$ precursors (Figure 2.2) with H_2O_2 has been discussed in detail in Chapter 2. Note that each of the clusters presents a number of reactive oxygen centres suitable to initiate the homolytic C-H cleavage. The reactive oxygens considered explicitly in this study are denoted with an asterisk (*) and Arabic numerals in Figure 4.1 B. The binuclear clusters were accommodated inside the ZSM-5 pores at different extra-framework positions (Figure 4.1 C) with varied confinement and coordination properties. The α and δ sites are the 6 member-ring (MR) units located along the main channel of ZSM-5 and the ϵ site represents a cation position across it. The β and γ sites are, respectively the 6MR and 8MR rings on the wall of the sinusoidal channel. Besides these intra-zeolite cation sites, open site models (site o) were included in our analysis to simulate a less confined environment of the binuclear Fe sites located at the outer surface of the zeolite. The combination of the Arabic numeral indicating the proton-accepting site of the di-Fe cluster and the Greek symbol for the position in the zeolite are used to differentiate the reactive models studied here. For some sites, we identified several alternative reaction channels with different energetics starting from different adsorption configurations of methane. These reaction channels are distinguished by a * symbol(s) in the notation of the active site. The local optimized geometries of all reactive sites studied in this work are summarized in Figure 4.2.

Despite binuclear Fe sites can initiate different mechanisms of C-H activation, in this study we specifically focused on the homolytic C-H cleavage / radical rebound mechanism widely accepted as the dominant path in methane to methanol oxidation by zeolite-based and generally site-isolated heterogeneous catalysts [39, 40]. A simplified reaction energy profile, state and energy definitions used in this study are schematically summarized in Figure 4.3 A. The reference state is the non-interacting active site in the periodic zeolite model and a free methane molecule in the gas-phase (*site*). The reactions start from the state *site*+ CH_4 representing an adsorption complex of methane at the zeolite active site, from which the C-H bond cleavage via a homolytic transition state (*TS*) can take place to form a $1e^-$ reduced di-Fe complex and a $\cdot\text{CH}_3$ species (*site*- $\text{H}^+\cdot\text{CH}_3$). The catalytic process proceeds further via the recombination of the partially reduced *site* and the radical to form methanol or a grafted methoxy species [10a]. This recombination step is chemically independent of the initial C-H activation and therefore is not considered in this study devoted to the analysis of the secondary effects on the energy scaling relations for homolytic C-H activation. The

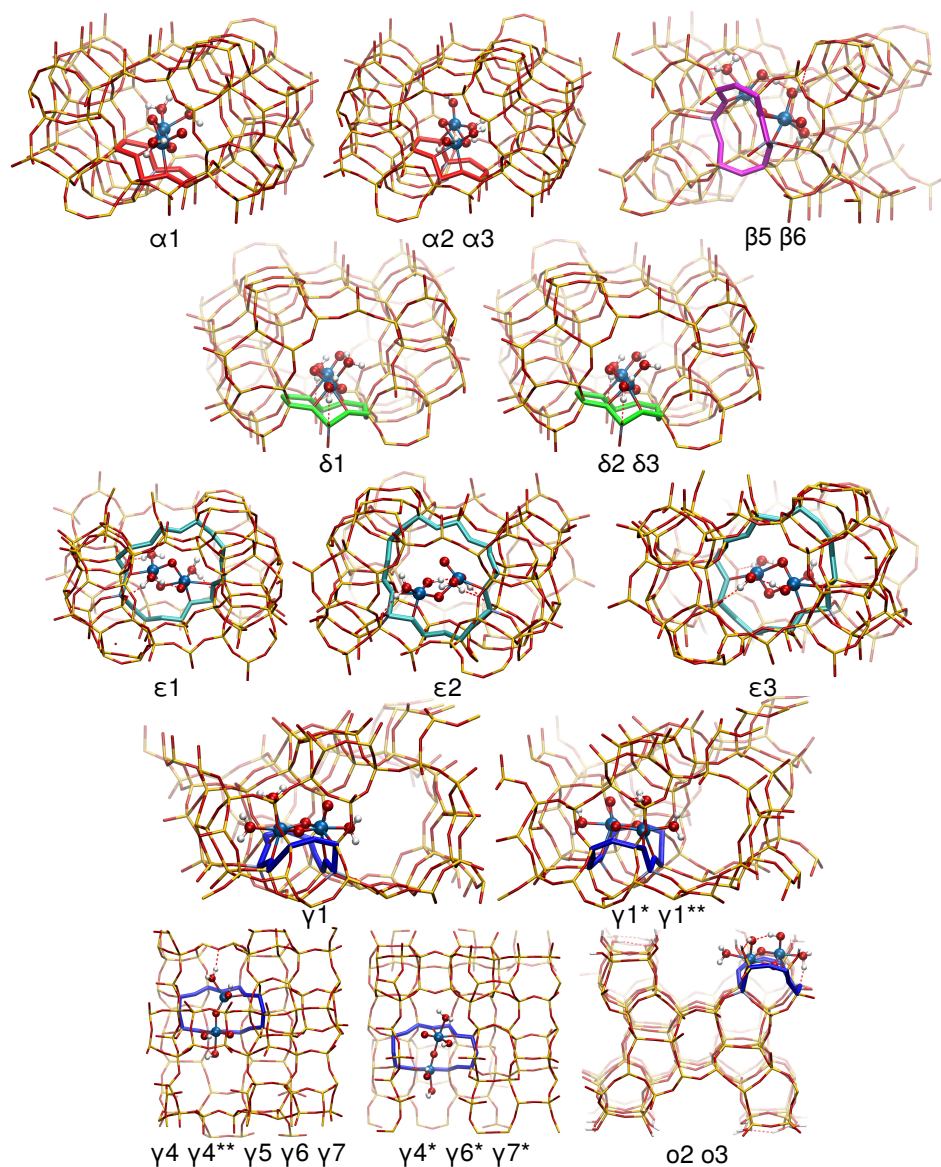


Figure 4.2: Site of all reaction of this chapter and the unit cell of ZSM-5 zeolite. The colours correspond to the colours of Figure 4.1 C. α , δ and ϵ sites are positioned in the main channel, while β and γ sites are located in the sinusoidal channel. In each ring two Si atoms are exchanged to Al.

thermodynamic cycle however can be established between the product of homolytic C-H cleavage ($site-H^+ \cdot CH_3$) and the H-affinity of the active site, which is formed upon the desorption of a $\cdot CH_3$ radical. Such a configuration can be formed when radical recombination takes place at a distant site leaving behind the reduced Fe complex ($site-H$). Below we refer to both $site-H^+ \cdot CH_3$ and $site-H$ as the final states (FSs) of the

methane activation reaction.

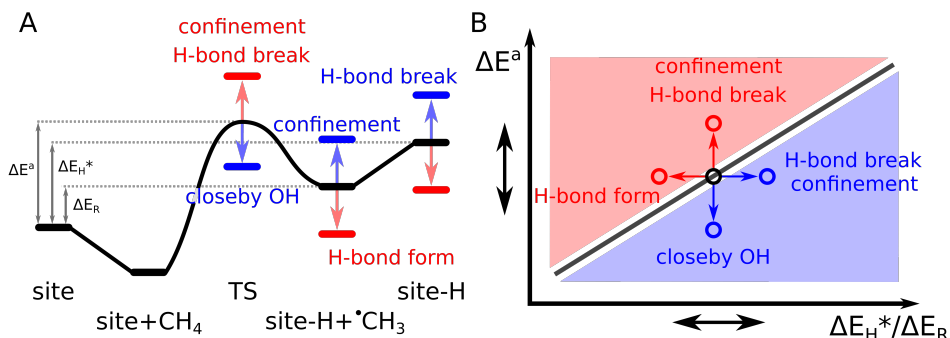


Figure 4.3: Generalized (A) energy diagram and (B) linear energy relationships ($\Delta E^a - \Delta E_R$ and $\Delta E^a - \Delta E_H$) for the rebound mechanism of CH_4 with schematic indication of the influence of the secondary effects on the energetics of the individual states and the associated deviations from the fundamental scaling laws. Negative deviations due to *TS* destabilization or *FS* stabilization are shown in red, while blue colour is used to indicate effects resulting in lower *TS* energies and relatively higher energies of *FS* giving rise to the apparently higher reactivity of the active site than predicted by the idealized energy scaling relationship.

Following the above definition of the main states, we define the reaction energy ΔE_R , apparent activation energy (ΔE^a), and H-affinity (ΔE_H) as

$$\Delta E_R = E(\text{site} - \text{H} + \cdot\text{CH}_3) - E(\text{site}) - E(\text{CH}_4) \quad (4.1)$$

$$\Delta E^a = E(\text{TS}) - E(\text{site}) - E(\text{CH}_4) \quad (4.2)$$

$$\Delta E_H^* = E(\text{site} - \text{H}) - E(\text{site}) + E(\cdot\text{CH}_3) - E(\text{CH}_4) \quad (4.3)$$

$$\Delta E_H = E(\text{site} - \text{H}) - E(\text{site}) + \frac{1}{4}E(\text{O}_2) - \frac{1}{2}E(\text{H}_2\text{O}) \quad (4.4)$$

where $E(\text{H}_2\text{O})$, $E(\text{O}_2)$, $E(\text{CH}_4)$ and $E(\cdot\text{CH}_3)$ are the DFT-computed energies of the respective molecules in the gas phase. Although the H-affinity ΔE_H^* given by equation 4.3 can directly be related to the thermodynamic cycles of the investigated process, as shown in Figure 4.1 A, in the discussion below a generalized H-affinity ΔE_H defined in ref.[8] and given with (4.4) will be used as a descriptor to facilitate the comparison between the current results and those reported in the literature. The two parameters differ by a constant corresponding to the energy difference in the molecular reference states. The slope of the fundamental $\Delta E^a - \Delta E_H$ and $\Delta E^a - \Delta E_H^*$ relationships should therefore be the same and any deviation from it is not influenced by the choice of the

equation.

Figures 4.4A and B show the relationships between the computed values of ΔE^a and the reaction energies (ΔE_R) and hydrogen affinities (ΔE_H), respectively, with the corresponding linear fits. The ΔE_R descriptor accounts for (de)stabilization of both $\cdot CH_3$ and H-[O] reactive species forming in the *TS* resulting in a better linearity of the respective ΔE^a - ΔE_R correlation ($R^2 = 0.754$, Figure 4.4 A) compared to the more general ΔE^a - ΔE_H relationship ($R^2 = 0.422$, Figure 4.4 B). The mean absolute errors (MAE) for both correlations are comparable (13 and 17 kJ/mol, respectively) and are of the same magnitude as the MAE of 11 kJ/mol obtained for a much larger dataset in reference [8]. Despite having similar slopes (0.75 and 0.79, respectively) indicating the fundamental nature of the ΔE^a - ΔE_H correlation, a 16 kJ/mol shift in the intercept is observed compared to the scaling law reported in reference [8]. It is most likely due to the different exchange-correlation functionals employed. Figure 4.4 indicates that the current correlation established for Fe-ZSM-5 zeolite also holds for a related Fe-MIL-53(Al) metal organic framework (MOF) catalytic system [41].

The results in Figure 4.4 A reveal substantial deviations of the computed activation barriers from the linear ΔE^a - ΔE_R trend. For example, significantly (deviation > 15 kJ/mol) lower reactivity is predicted for $\alpha 3$, $\epsilon 3$, $\gamma 7$, and $\gamma 7^*$ sites, while the $\gamma 1$, $\gamma 6^*$ and $\gamma 1^*$ sites are predicted to be substantially more reactive than could be deduced from the idealized ΔE^a - ΔE_R scaling relationship. The deviations of the computed activation energies from those estimated based on the ΔE^a - ΔE_H correlation are much more substantial. Such direct relationships between the thermodynamic and kinetic parameters generally hold for reactive systems characterized by similar shapes of the potential energy surfaces (PES), i.e. for the systems with well-defined reactive centres, which intrinsic chemistry determines the chemical behaviour. The secondary interactions in a multi-site and/or confined environment of the reactive complexes in zeolite pores can impact significantly the involved PES giving rise to notable deviations from the energy scaling relationships.

In the current case we note that effects such as secondary hydrogen bonding interactions at the di-Fe site and specific confinement of the activated complexes exerted by the zeolite pores are the main causes for the observed deviations from the idealized energy trends. The stabilizing and destabilizing effects associated with these secondary interactions are summarized schematically in Figure 4.3. The stabilization of the *TS* and the destabilization of the product state employed in a particular correlation (i.e. *site-H+* $\cdot CH_3$ for ΔE^a - ΔE_R and *site-H* for ΔE^a - ΔE_H) results in a favourable deviation from the linear scaling (a lower activation energy), whereas the destabilization of the *TS* and the stabilization of the product state has an opposite effect on the activation

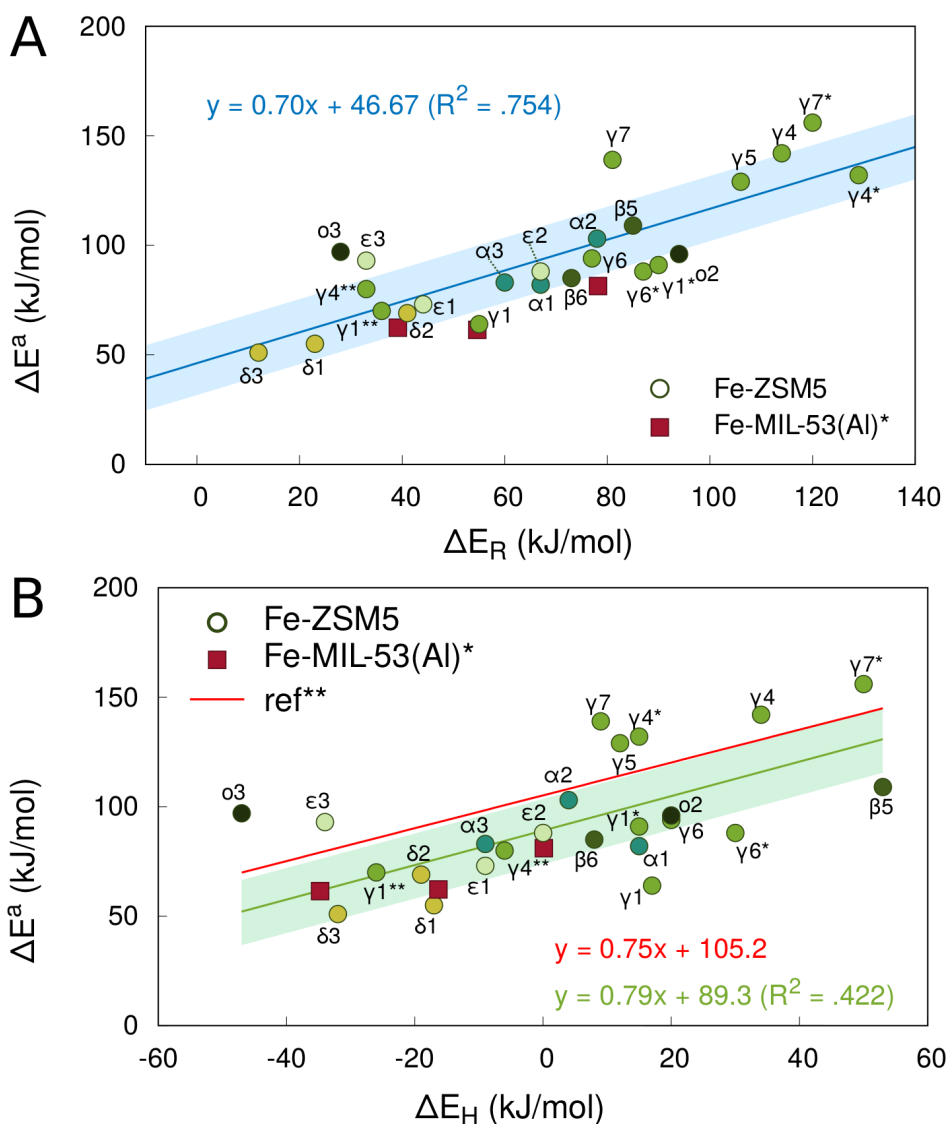


Figure 4.4: The computed correlations between the computed kinetic (ΔE^a) and thermodynamic ((A) ΔE_R and (B) ΔE_H) parameters of methane activation by binuclear Fe sites in ZSM-5 zeolite (circles) and Fe-MIL-53 MOF (squares). The trend lines shown in the graph provide liner fits for the datasets with ± 15 kJ/mol shown with shaded areas.

energy. Our calculations point to two main factors, namely the confinement and H-bonding rearrangement, causing the deviations of the predicted reactivity from the idealized scaling law reflecting the intrinsic reactivity of the localized catalytic site. The results of a semi-quantitative analysis of the nature and impact of these factors and their more specific contributions are summarized in Table 4.1. Below we

will discuss in detail the impact of each of the factors on the predicted reactivity of zeolite-stabilized di-Fe complexes in homolytic C-H activation of methane.

Table 4.1: Semi-quantitative analysis of the main secondary interactions due to confinement, flexibility and multifunctionality of the active site on methane activation and the associated deviations (in kJ/mol) from the fundamental linear energy relationships. The occurrence of the particular effect for the given reaction is indicated with a + sign. The direction of the deviation is indicated using the colour code as defined in Figure 4.3. [a] Confinement effects in the transition state are quantified by considering the number of atoms η_A, TS of the zeolite within a 3.5 Å sphere neighbouring the C centre, while in the *FS* state it is quantified with η_A, FS , which is the distance between the C of the methyl radical and the subtracted H atom in Å. [b] The effects of active site flexibility on the reaction mechanism in the current system are associated with the rearrangement of the H-bond networks in the course of the reaction such as the H-bond cleavage in the *TS* and H-bond stabilization of the *FS* and *site-H*, manifesting themselves in, respectively, $\Delta E^a - \Delta E_R$ and $\Delta E^a - \Delta E_H$ correlations. [c] The presence of different functional groups within the active centre allow for an alternative OH-cooperative mechanism of methane activation.

Reaction	Confinement[a]		Flexibility[b] and Multifunctionality[c]				Energy deviation (kJ/mol) from	
	η_A, TS	η_A, FS	H-bond break. @ TS	H-bond form. @ 'site-H+' · CH ₃ '	H-bond form. @ 'site-H'	OH-cooperativity	$\Delta E^a - \Delta E_R$	$\Delta E^a - \Delta E_H$
$\alpha 1$	- (2)	- (2.2)	-	-	-	-	-11	-19
$\alpha 2$	- (7)	- (2.3)	-	-	-	-	1	10
$\alpha 3$	- (3)	- (2.1)	-	-	-	-	-6	1
$\beta 5$	- (5)	- (2.2)	-	-	+	-	3	-22
$\beta 6$	- (5)	- (2.1)	-	-	+	+	-13	-10
$\gamma 1$	- (4)	- (2.1)	-	-	-	+	-21	-38
$\gamma 1^*$	+ (13)	+ (1.6)	-	-	-	-	-19	-10
$\gamma 1^{**}$	- (5)	- (2.0)	-	+	-	+	-2	1
$\gamma 4$	+ (12)	- (1.9)	-	-	-	-	16	26
$\gamma 4^*$	+ (8)	+ (1.8)	-	-	+	-	-5	31
$\gamma 4^{**}$	- (6)	- (2.0)	-	+	-	+	10	-5
$\gamma 5$	+ (11)	+ (1.8)	-	-	+	-	8	31
$\gamma 6$	+ (12)	- (1.9)	-	-	-	+	-7	-11
$\gamma 6^*$	- (6)	- (2.1)	-	-	-	+	-19	-25
$\gamma 7$	+ (12)	- (2.1)	-	-	-	-	36	43
$\gamma 7^*$	+ (9)	- (2.1)	-	-	-	-	25	28
$\delta 1$	- (3)	- (2.0)	-	-	-	+	-8	-21
$\delta 2$	- (1)	- (1.9)	-	-	-	-	-11	-5
$\delta 3$	- (2)	- (2.1)	-	-	-	-	-4	-13
$\epsilon 1$	- (5)	- (2.4)	-	-	-	-	-4	-9
$\epsilon 2$	- (1)	- (2.2)	-	-	-	-	-6	-2
$\epsilon 3$	- (5)	- (2.5)	+	-	-	-	24	31
$\sigma 2$	- (4)	- (1.9)	-	-	+	+	-16	-9
$\sigma 3$	- (3)	- (2.1)	+	-	-	-	30	44

Confinement effects due to the constraints of the zeolite micropores can manifest in destabilization of (i) the *TS* and (ii) the product *site-H+* · CH₃ states. The former scenario is realized when the zeolite walls exert geometrical constraints to CH₄ approaching the reactive O-centre, resulting in the effective destabilization of the transition state. To establish a (semi-)quantitative descriptor for such a confinement effect, we consider the number of atoms excluding the H atoms of methane (η_A, TS , Table 4.1) from the zeolite lattice and reaction centre within 3.5 Å from the C atom of CH₄ fragment. We note that the number of atoms close to the reactive moiety in the *TS* reflects the decreased accessibility of the active site by CH₄ and is generally associated

with a higher reaction barrier.

An illustrative example of this destabilization mechanism is the *TS* for the $\gamma 6$ site and *TS*- $\gamma 4^*$ shown in Figure 4.5 A and C. Both structures have 12 neighbouring atoms within 3.5 Å from the reactive C atom. In these geometries, the rigid zeolite framework prevents CH₄ from approaching the active O-site from the optimal angle thus increasing the activation barrier. We identify that *TS* confinement is the sole factor giving rise to the pronounced deviations from the linear scaling relationships for the sites $\gamma 4$, $\gamma 7$ and $\gamma 7^*$, for which the C-H activation barriers are 16 to 43 kJ/mol higher than those predicted based on the ΔE^a - ΔE_R and ΔE^a - ΔE_H correlations.

However, the number of atoms in the vicinity of the active site cannot be viewed as a universal indicator for the unfavourable impact of zeolite confinement. Previous theoretical studies indicate a pronounced reactivity dependence for homolytic C-H cleavage on the angle at which the reactant approaches the reactive centre [42]. Depending on the Fe–O–HCH₃ angle, the reaction can proceed either via the σ -channel and involve the interaction with the Fe(*d_{z²}*)+O(*p_z*) orbital or via the commonly much less favourable π -channel, involving the interaction with the Fe(*d_{xz/yz}*)-O(*p_{x/y}*) orbital (additional explanation can be found in ref.[25] and in the Introduction in Figure 1.5). Restricted accessibility of the reactive oxygen centre due to confinement can flatten the associated PES and make the reactivity along the two channels comparable. On the other hand, an optimal angle of attack providing the favourable orbital overlap may still potentially be established despite the crowdedness at the active centre. The only active site showing such a favourable geometry is $\gamma 1^*$ (Figure 4.6), for which, despite having the highest $\eta_{A,TS}$ among the structures considered here, the activation energy shows a favourable deviation in both linear correlations.

The geometrical constraints on the *TS* also affect the energetics of the associated *site-H*+·CH₃ product state. The equilibrium distance between the ·CH₃ radical and the HO-moiety of the partially reduced site is ca. 2.0 Å in the absence of the geometrical constraints due to zeolite pores. The increased confinement limits the mobility of ·CH₃ resulting in shorter ·CH₃··HO distances and, accordingly, increased energy of the *site-H*+·CH₃ state. Such situations are encountered in, for example, sites $\gamma 4^*$ (Figure 4.5 C), $\gamma 1^*$ and $\gamma 5$ (Figure 4.7). Importantly, the reactivity deviations induced by the confinement-induced transition (*TS*) and product (*FS*) states destabilization are very different. The *TS* confinement gives rise to an unfavourable reactivity shift to the red zone, while the *FS* confinement, on contrary, places the reactive system into the blue zone (Figure 4.3 B). The mutual cancellation of these two effects is the main reason for the higher linearity of the ΔE^a - ΔE_R correlation. The ΔE^a - ΔE_H correlation

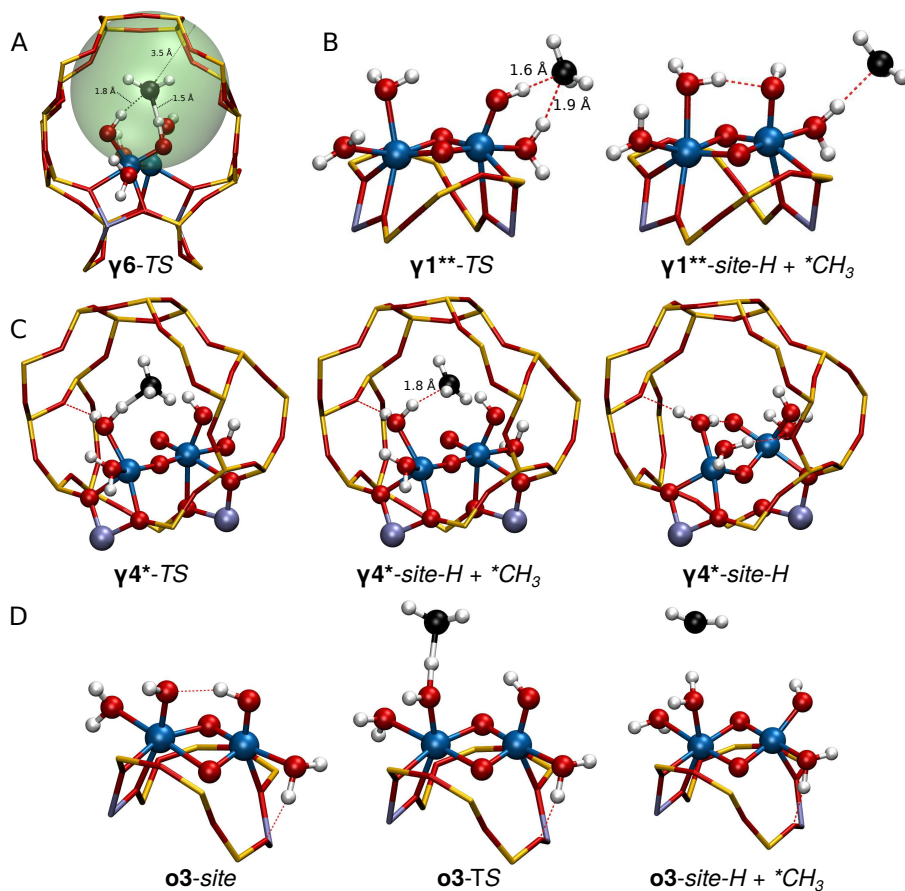
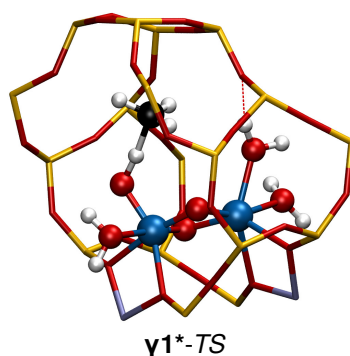
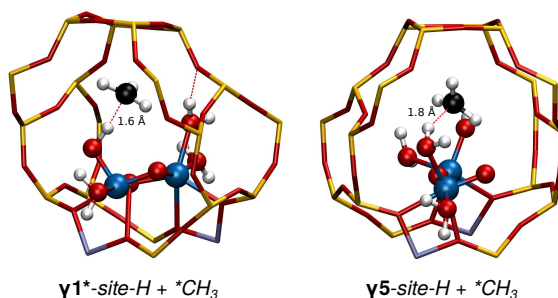


Figure 4.5: Representative cases for all identified deviation mechanisms. A) Local structure of the TS of methane C-H bond activation at the location of γ_6 . The green sphere indicates totally 12 atoms from framework and reaction centre distributed in the radius of 3.5 Å of the C atom indicating that the TS is confined. H-bonding interaction of TS with a close-by OH group is also highlighted. B) Steps of reaction γ_1^{**} . In the transition state there are two OH groups close to the forming CH_3 radical. There is an additional H bond present compared to TS stabilising this intermediate in *site-H* + CH_3 . C) Steps of reaction γ_4^* with a confined TS and a confined *site-H* + CH_3 where the H-C distance is 1.8 Å. In the reduced site-H the H subtracted from the methane rotates and forms an additional H bond with the terminal O of the other Fe ion thus stabilising site-H. D) Steps of reaction $\text{o}3$. In *site* there is a H-bond between the two OH ligands of Fe which breaks in the transition state.

does not account for the FS confinement and associated energy effects.

H-bonding rearrangement is, in the course of the reaction, another important factor affecting the shapes of the PES and giving rise to deviations from the linear energy scaling relationships. Calculations reveal that most reaction channels over the active sites featuring multiple OH ligands and coordinated H_2O involve the concomitant cleavage and formation of hydrogen bonds, which, depending on the specific situa-

Figure 4.6: Confined TS of reaction $\gamma 1^*$.Figure 4.7: Confined *site-H* + $\cdot CH_3$ of reaction $\gamma 1^*$ and $\gamma 5$.

tion, may give rise to both favourable and unfavourable deviations from the predicted reactivity. One can distinguish 4 scenarios of such H-bonding rearrangements: (i) H-bond cleavage at TS, (ii) H-bond stabilization of the FS, (iii) H-bond stabilization of the partially reduced state *site-H*, and (iv) OH/H₂O cooperative C-H cleavage.

Terminal hydroxyl ligands on the binuclear Fe complexes have been identified as the potential sites for homolytic C-H activation[21]. The formation of H-bonds between these ligands and neighbouring proton-donating/accepting sites provide an additional stabilization to the complex (see e.g. Figure 4.5 D). However, during the C-H activation process, these H-bonds need to be broken at the TS to allow for the favourable orbital overlap between the reacting species. The associated energy losses are not recovered in the product states. The loss of such favourable H-bond interaction during methane activation destabilizes both the TS and *site-H* + $\cdot CH_3$ states. The destabilization is much more pronounced in the TS state as indicated by the consistent negative deviation (by 24 - 44 kJ/mol into red zone) of the predicted reactivity for the sites featuring this effect ($\epsilon 3$ and $\mathbf{o}3$, Figure 4.5 D).

The partial reduction of the binuclear cationic complex upon reaction with methane can be also accompanied by the pronounced configurational changes in the binuclear

active site resulting in the formation of additional H-bonds between the terminal OH, O or H₂O ligands. This results in the stabilization of *site-H*+(\cdot CH₃) and shifts the reaction energy (ΔE_R) to the left-hand side of the BEP relationship (Figure 4.3, Table 4.1). Representative examples are the reactions at sites $\gamma 1^{**}$ and $\gamma 4^{**}$. The optimized *TS* and *site-H*+ \cdot CH₃ structures for $\gamma 1^{**}$ are shown in Figure 4.5 B. The reactive Fe complex in this case bears two μ -O ligands, three terminal H₂O and an oxo ligand. These ligands do not form intermolecular hydrogen bonds either in the pristine state *site* or in the *TS* state. Upon the reduction, the geometry of the cluster changes: most notably, the distance between the Fe centres decreases with the concomitant change in the relative configuration of the ligands so that an H-bonding can now be established between the newly formed Fe₁-OH and Fe₂-OH₂ moieties.

4

The geometry of the reduced site can further alter after the removal of the \cdot CH₃ radical (Table 4.1 column 6). This situation is illustrated in Figure 4.5 C with the optimized structures of *TS*, *site-H*+ \cdot CH₃ and *site-H* for reaction $\gamma 4^*$. The relaxation of the reduced di-Fe complex after the removal of steric constraints imposed by the weakly-bound \cdot CH₃ species may result in a substantial stabilization of the *site-H* reference state due to the formation of additional H-bonds. This effect is only apparent in the ΔE^a - ΔE_H correlation, where a deviation towards a red zone is commonly observed. As a result of these secondary interactions, lower values of H-affinity are computed for such sites, which, however, is not related to the increased reactivity of the hydrogen-accepting moiety. For the different active site locations considered in this study, this H-bonding stabilization effect was not observed independently without contributions from other (de)stabilization effects.

Multifunctionality of the active site can also cause deviations from the linear scaling relationship. Our DFT calculations suggest that the intrinsic reactivity of the Fe-O moieties towards the homolytic C-H dissociation can be influenced by the presence of vicinal OH and H₂O. Such a multifunctional environment allows for a more efficient stabilization of the \cdot CH₃ radical formed in the *TS* through secondary interactions with the OH/H₂O. This, in turn, leads to a pronounced lowering of the activation barrier for the reaction as compared to a hypothetical single-site mechanism (Table 4.1 column 7). Figures 4.6 A and B show the representative optimized structures of such cooperative *TS*s for $\gamma 6$ and $\gamma 1^{**}$. The interatomic distance for the “activated” C-H bond (OH \cdots CH₃, 1.5-1.6 Å) is comparable to that formed as a secondary interaction between the \cdot CH₃ radical and a vicinal OH moiety (1.8-1.9 Å). A substantial *TS* stabilization due to such a cooperative reaction mechanism is observed for the structures with secondary $r(\text{OH}\cdots\text{CH}_3) < 2.7$ Å. The examples where this effect is solely responsible for the deviations from the linear energy relations are the reactions $\gamma 1$, $\gamma 6^*$ and $\delta 1$

(Figure 4.8). This cooperative methane activation mechanism has an impact on both linear relationships resulting in computed activation barriers 8-38 kJ/mol lower than the ones predicted from the linear fits.

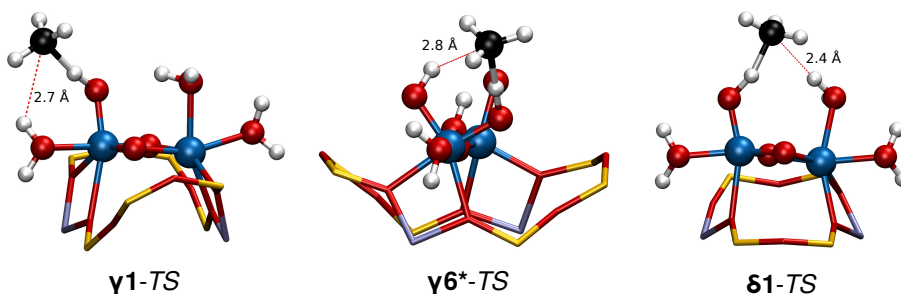


Figure 4.8: Transition states of reaction $\gamma 1$, $\gamma 6^*$, and $\delta 1$. The distance of the closest H atom is shown in the figure.

Importantly, all these effects can manifest themselves simultaneously. For example, the confinement of both *TS* and *site-H+·CH₃*, or the *TS* confinement and OH-cooperative methane activation mechanism can be encountered in the same system, and effectively cancel out or amplify the individual energy (de)stabilization effects. This can either give rise to the increased deviation from the trend line or, on contrary, to an apparent improvement of the linearity in the energy relation. For example, the *TS* and *site-H+·CH₃* confinement destabilize both the transition and the final state for $\gamma 4^*$ (Figure 4.5 C) and $\gamma 5$ (Figure 4.7), which reactivity perfectly follow the $\Delta E^a - \Delta E_R$ scaling trend. However, *site-H* for these configurations is additionally stabilized by H-bond, which causes substantial deviations in the $\Delta E^a - \Delta E_H$ relationship. For the sites $\gamma 1^{**}$ and $\gamma 4^{**}$ the opposing effects of OH-cooperativity and H-bond rearrangements during methane activation cancel each other out as is evident from the minimal deviation of the corresponding computed and expected energetics (Table 4.1).

4.4. CONCLUSIONS

FUNDAMENTAL reactivity theory implies that there is a relationship between thermodynamics and kinetics when the intrinsic chemistry of the active site is in charge of the activity. However, this study identifies that besides the intrinsic reactivity of the active site, there is a number of secondary effects present in microporous catalytic materials that can outweigh the intrinsic chemistry and break the scaling relationships. (i) The confinement of porous frameworks does have an effect on the reaction barrier. Confinement of the transition state limits the geometry flexibility, and thus increases the reaction barrier. (ii) H-bond breaking or forming leads to the

destabilization or stabilization of the reaction intermediates, moving the points in Figure 4.3 away from the scaling relationships. (iii) Direct stabilization of the transition state was observed when the interaction of a close-by OH group and the CH₃ radical was realized. This interaction lowers the energy of the transition state and breaks the scaling relations, which is proposed to be a practical strategy for catalyst design towards methane activation.

REFERENCES

- [1] J. Greeley, *Annu. Rev. Chem. Biomol.*, 2016, **7**, 605–635.
- [2] F. Calle-Vallejo, D. Loffreda, M. T. M. Koper and P. Sautet, *Nature Chem.*, 2015, **7**, 403–410.
- [3] H. Xin, A. Vojvodic, J. Voss, J. K. Nørskov and F. Abild-Pedersen, *Phys. Rev. B*, 2014, **89**, 115114.
- [4] N. Rezaei-Ghaleh, G. Parigi, A. Soranno, A. Holla, S. Becker, B. Schuler, C. Luchinat and M. Zweckstetter, *Angew. Chem. Int. Ed.*, 2018, **57**, 15262–15266.
- [5] M. A. Barteau, *Catal. Lett.*, 1991, **8**, 175–183.
- [6] A. Logadottir, T. H. Rod, J. K. Nørskov, B. Hammer, S. Dahl and C. J. H. Jacobsen, *J. Catal.*, 2001, **197**, 229–231.
- [7] J. K. Nørskov, T. Bligaard, A. Logadottir, S. Bahn, L. B. Hansen, M. Bollinger, H. Bengaard, B. Hammer, Z. Sljivancanin, M. Mavrikakis, Y. Xu, S. Dahl and C. J. H. Jacobsen, *J. Catal.*, 2002, **209**, 275–278.
- [8] K. Tran and Z. W. Ulissi, *Nature Catal.*, 2018, **1**, 696–703.
- [9] Z. W. Ulissi, A. J. Medford, T. Bligaard and J. K. Nørskov, *Nature Commun.*, 2017, **8**, 14621.
- [10] L. Grajciar, C. J. Heard, A. A. Bondarenko, M. V. Polynski, J. Meeprasert, E. A. Pidko and P. Nachtigall, *Chem. Soc. Rev.*, 2018, **47**, 8307–8348.
- [11] A. B. Laursen, R. B. Wexler, M. J. Whitaker, E. J. Izett, K. U. D. Calvino, S. Hwang, R. Rucker, H. Wang, J. Li, E. Garfunkel, M. Greenblatt, A. M. Rappe and G. C. Dismukes, *ACS Catal.*, 2018, **8**, 4408–4419.
- [12] A. A. Latimer, A. R. Kulkarni, H. Aljama, J. H. Montoya, J. S. Yoo, C. Tsai, F. Abild-Pedersen, F. Studt and J. K. Nørskov, *Nat. Mater.*, 2017, **16**, 225–229.
- [13] A. I. Olivos-Suarez, A. Szécsényi, E. J. M. Hensen, J. Ruiz-Martinez, E. A. Pidko and J. Gascon, *ACS Catal.*, 2016, **6**, 2965–2981.
- [14] J. Bao, G. Yang, Y. Yoneyama and N. Tsubaki, *ACS Catal.*, 2019, 3026–3053.
- [15] K. T. Dinh, M. M. Sullivan, P. Serna, R. J. Meyer, M. Dincă and Y. Román-Leshkov, *ACS Catal.*, 2018, **8**, 8306–8313.
- [16] G. Li, P. Vassilev, M. Sanchez-Sanchez, J. Lercher, E. J. M. Hensen and E. A. Pidko, *J. Catal.*, 2016, **338**, 305–312.
- [17] M. H. Mahyuddin, T. Tanaka, Y. Shiota, A. Staykov and K. Yoshizawa, *ACS Catal.*, 2018, **8**, 1500–1509.
- [18] A. S. Rosen, J. M. Notestein and R. Q. Snurr, *ACS Catal.*, 2018, **0**, 3576–3587.
- [19] G. Sun, Z. Zhao, R. Mu, S. Zha, L. Li, S. Chen, K. Zang, J. Luo, Z. Li, S. C. Purdy, A. J. Kropf, J. T. Miller, L. Zeng and J. Gong, *Nature Commun.*, 2018, **9**, year.
- [20] P. Mehta, P. Barboun, F. A. Herrera, J. Kim, P. Rumbach, D. B. Go, J. C. Hicks and W. F. Schneider, *Nature Catal.*, 2018, **1**, 269–275.
- [21] M. L. Pegis, C. F. Wise, B. Koronkiewicz and J. M. Mayer, *J. Am. Chem. Soc.*, 2017, **139**, 11000–11003.

- [22] T. Z. H. Gani and H. J. Kulik, *ACS Catal.*, 2018, **8**, 975–986.
- [23] L. Jiao, Y. Wang, H. . Jiang and Q. Xu, *Adv. Mater.*, 2018, **30**, year.
- [24] J. Gascon, A. Corma, F. Kapteijn and F. X. Llabrés I Xamena, *ACS Catal.*, 2014, **4**, 361–378.
- [25] M. John, K. Alexopoulos, M. . Reyniers and G. B. Marin, *ACS Catal.*, 2016, **6**, 4081–4094.
- [26] C. Liu, I. Tranca, R. A. Van Santen, E. J. M. Hensen and E. A. Pidko, *J. Phys. Chem. C*, 2017, **121**, 23520–23530.
- [27] T. Liang, J. Chen, Z. Qin, J. Li, P. Wang, S. Wang, G. Wang, M. Dong, W. Fan and J. Wang, *ACS Catal.*, 2016, **6**, 7311–7325.
- [28] G. I. Panov, A. K. Uriarte, M. A. Rodkin and V. I. Sobolev, *Catal. Today*, 1998, **41**, 365–385.
- [29] C. Hammond, M. M. Forde, M. H. Ab Rahim, A. Thetford, Q. He, R. L. Jenkins, N. Dimitratos, J. A. Lopez-Sanchez, N. F. Dummer, D. M. Murphy, A. F. Carley, S. H. Taylor, D. J. Willock, E. E. Stangland, J. Kang, H. Hagen, C. J. Kiely and G. J. Hutchings, *Angew. Chem. Int. Ed.*, 2012, **51**, 5129–5133.
- [30] D. Osadchii, A. Olivos Suarez, A. Szécsényi, G. Li, M. Nasalevich, A. Dugulan, P. Serra-Crespo, E. Hensen, S. Veber, M. Fedin, G. Sankar, E. Pidko and J. Gascon, *ACS Catal.*, 2018, **8**, 5542–5548.
- [31] G. Kresse and J. Furthmüller, *Phys. Rev. B Condens. Matter Mater. Phys.*, 1996, **54**, 11169–11186.
- [32] G. Kresse, *Phys. Rev. B Condens. Matter Mater. Phys.*, 1999, **59**, 1758–1775.
- [33] J. P. Perdew, K. Burke and M. Ernzerhof, *Phys. Rev. Lett.*, 1996, **77**, 3865–3868.
- [34] P. Blöchl, *Phys. Rev. B*, 1994, **50**, 17953–17979.
- [35] S. Grimme, J. Antony, S. Ehrlich and H. Krieg, *J. Chem. Phys.*, 2010, **132**, 154104.
- [36] G. Henkelman, B. P. Uberuaga and H. Jónsson, *J. Chem. Phys.*, 2000, **113**, 9901–9904.
- [37] A. Szécsényi, G. Li, J. Gascon and E. A. Pidko, *ACS Catal.*, 2018, **8**, 7961–7972.
- [38] P. Belanzoni, L. Bernasconi and E. J. Baerends, *J. Phys. Chem. A*, 2009, **113**, 11926–11937.
- [39] J. S. Woertink, P. J. Smeets, M. H. Groothaert, M. A. Vance, B. F. Sels, R. A. Schoonheydt and E. I. Solomon, *Proc. Natl. Acad. Sci. U. S. A.*, 2009, **106**, 18908–18913.
- [40] M. H. Ab Rahim, M. M. Forde, R. L. Jenkins, C. Hammond, Q. He, N. Dimitratos, J. A. Lopez-Sanchez, A. F. Carley, S. H. Taylor, D. J. Willock, D. M. Murphy, C. J. Kiely and G. J. Hutchings, *Angew. Chem. Int. Ed.*, 2013, **52**, 1280–1284.
- [41] A. Szécsényi, G. Li, J. Gascon and E. A. Pidko, *Chem. Sci.*, 2018, **9**, 6765–6773.
- [42] A. Kazaryan and E. Baerends, *ACS Catal.*, 2015, **5**, 1475–1488.

5

ANALYSIS OF C-H BOND ACTIVATION WITH MULTIREFERENCE CASSCF/CASPT2 METHOD

In this chapter the C-H bond activation of methane by binuclear iron-oxo clusters deposited in Fe-ZSM-5 was explored with quantum chemical methods. Three alternative reaction mechanisms, namely the homolytic and heterolytic C-H activation and the Fenton path were included in the analysis. The energetics of the reactions and electronic structures of the reaction intermediates were studied by five popular density functional methods (GGA: OPBE, PBE(D3-BJ); meta-GGA: M06L, MN15L; and hybrid: B3LYP functional), and with the multiconfigurational self-consistent field method followed by second order perturbation theory (CASSCF/CASPT2). Qualitatively similar performance is shown for all functionals. In case the intermediates can be described without multiconfigurational wave function, MN15L and M06L performs the best. Although all investigated functionals in such cases reproduce the energy trends derived using the higher-level wave function method, they underestimate the reaction barrier and energy. However, if it is necessary to employ multiconfigurational wave function, neither of the functionals perform satisfactorily. In these cases, DFT cannot describe the electronic configuration properly and therefore even when providing energetics in a satisfactory agreement the explanation behind the reactivity based on electronic structure is not valid. Besides the transferability of the functional to other complexes is not guaranteed.

5.1. INTRODUCTION

COMPUTATIONAL chemistry plays a crucial role in investigating mechanisms of catalytic reactions and identifying the preferable pathways. The ultimate goal of such studies is to be able to predict properties of catalysts that facilitate the reaction or enhance selectivity. Often structure-activity relations are set up with the help of computation chemistry calculations. Kohn-Sham density functional theory (KS-DFT) is routinely applied in these studies. The popularity of this method is due to its relatively low computational cost vs high method accuracy. This means that systems with hundreds of atoms can be modelled within reasonable timeframe with DFT. Post Hartree-Fock methods, are normally more accurate than DFT, however they scale much faster with the size of the system often strongly restricting the size of the system and is often limited to single point calculations. In the case of heterogeneous catalysts where the energy difference resulting from the secondary effects of the framework can be significant, sometimes outweighing the relative energy resulting from the intrinsic chemistry of bond-breaking and bond-formation, it is not possible to employ these methods, which most of the time are used only for benchmark purposes.

5

In methane conversion to methanol one of the most promising metal is iron [1–5]. Iron mostly forms highly open-shell complexes with degenerate or near-degenerate valence orbitals, which are difficult to describe by standard single-determinant KS-DFT [6]. Therefore, multireference calculations on single Fe sites have been conducted for benchmarking purposes. Pierloot and Vancoillie [7] considered three simple mononuclear Fe complexes with different ligand fields and compared the performance of three functionals with multiconfigurational self-consistent field method followed by second order perturbation theory (CASSCF/CASPT2), based on descriptors like energy difference between high and low spin state and geometry. They concluded that GGA functionals overstabilise the low-spin state, hybrid functional can predict the spin ladder correctly, depending on the extent of the exact exchange mixing, and there is no general rule for how much to apply. On the other hand DFT calculations predict accurate geometries, thus the higher level calculations might be used for single point energy calculations. Other studies were also performed to have a better insight into electronic structure of metal clusters, and reaction mechanisms. In a later study Pierloot and co-workers [8] investigated single site FeNO complexes with the previously mentioned methods. They focused on the comparison between spin densities calculated with DFT and CASSCF. They found that there are two dominant configurations for all structures and spin states that correspond to the Fe(II)–NO· and Fe(III)–NO[−] resonance structures. The spin population calculated by CASSCF is very much dependent on the spin state and ligand field, which has no cor-

relation with the contributions of the dominant configurations. The authors warned not to over-interpret spin densities as a measure of the oxidation state. They found the closest agreement between spin densities with the multireference results was achieved by non-hybrid DFT functionals. In this case the GGA OLYP and hybrid B3LYP functionals were found to perform best in terms of calculating the energy difference of the spin states. In another paper [9] for a different NiFe system they found B3LYP to fail, and the meta-GGA TPSS and the GGA PBE and BP86 give to best triplet-singlet energy difference. Xiao and Verma *et al.* [10, 11] explored ethane oxidation over an Fe(II) containing metal-organic framework. The electronic structure of the oxidized Fe(IV)O cluster, involved in methane oxidation, was thoroughly investigated by both DFT and CASSCF/CASPT2 methods revealing a multireference wave function to be necessary for the proper description of the active site. Neese *et al.* [12–15] described the electronic configuration of many Fe complexes and their spectroscopic properties and presented a commentary on correlated wave function methods in bioorganic chemistry [6]. Saik *et al.* [16] discuss the multiconfigurational treatment of heme-Fe systems, and Rulíšek and Srnc *et al.* [17] non-heme NHFe systems. There is a general consensus that a proper description of the electronic structure of mononuclear Fe complexes requires multireference wave functions and attempts to find a functional able to describe relative energies between either intermediates or spin states of the same complex are still ongoing.

Multinuclear Fe sites are however rarely discussed in the literature due to the size of the systems which require more orbitals and electrons to be considered than would be convenient. Calculations on binuclear Fe-Fe clusters were performed by Carlson *et al.* [18]. It was concluded that other than the 3d orbitals, a second shell of correlating 3d' orbitals of the Fe atoms are necessary for the correct description of the electronic structure and energy differences between different spin states. This is not the case for analogous Co-Co clusters. It was also found that GGA functionals capture at best the relative energies of spin states. In another study Morokuma *et al.* [19] employed density matrix renormalization group complete active space self-consistent field (DMRG-CASSCF) method to study magnetic coupling in dinuclear Fe and Cr complexes. DMRG allows the use of a large-size active space in multireference calculations, which makes it possible to handle an active space as large as 100 electrons on 100 orbitals. They found that DMRG-CASSCF with active spaces including the metal d orbitals, occupied bridging-ligand orbitals, and their virtual double shells already capture a major portion of the dynamic correlation effects, accurately reproducing the experimental magnetic coupling constant. Another DMRG-CASSCF study by Srnc *et al.* [20] investigated the reactivity of multiple binuclear Fe-oxo sites in the C-H bond dissociation of butane. The reaction and activation energies calculated by the

multireference (MR) method and different DFT functionals was compared. It was concluded that there is a large spread of reaction and activation energies, and DFT is unsuitable to give even quantitative results, as none of the tested DFT functionals could adequately predict the preferences toward various pathways (e.g. heterolytic vs homolytic C-H bond dissociation mechanisms). The authors stressed that although DMRG-CASSCF is not the "golden standard", it is expected to give the "right answers for the right reasons" because it properly describes highly multiconfigurational systems.

Multinuclear sites are considered among the most promising for designing methane oxidation catalysts. The computational investigation of such sites and reaction mechanisms are performed exclusively by DFT, a necessary sacrifice of method accuracy for model accuracy. Active multinuclear transition metal sites are presented by Ikuno *et al.* [21] applying Cu timers deposited on NU-1000 metal organic framework (MOF), Lercher *et al.* [22] recently presented a Cu-MOR zeolite with uniform trinuclear Cu sites and we present in Chapter 2-4 studies on binuclear Fe sites deposited in MIL-53 and ZSM-5 frameworks. Given the uncertainties of the performance of DFT methods towards the description of such systems, it is important to establish the borders of applicability of such methods for oxidation catalysis by multinuclear sites. In this chapter we focus on Fe-ZSM-5 zeolite which was studied experimentally by Hutchings *et al.* [5, 23, 24] in methane oxidation to methanol with H₂O₂ as oxidizing agent.

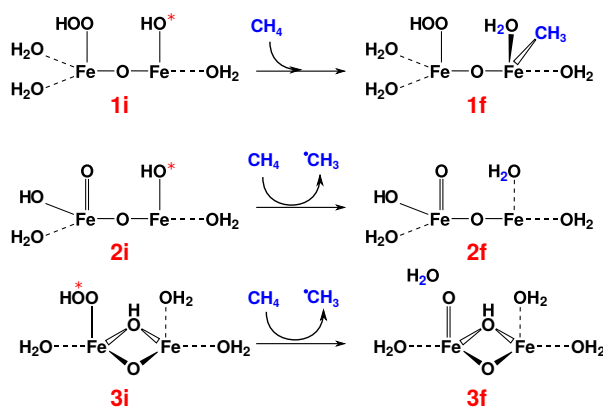


Figure 5.1: Schematic representation of the active site and the methane molecule and their reaction. (1) heterolytic, (2) homolytic dissociation, and (3) Fenton-type mechanism.

In this chapter we investigate two, mechanistically different types of activation: the heterolytic and homolytic dissociation of the C-H bond of methane. Additionally, a Fenton-type mechanism is investigated, which is a sub-class of homolytic disso-

ciation, where the transition metal cluster does not participate directly in the C-H bond dissociation but creates the reactive OH radical intermediate by cleaving the peroxy bond of H_2O_2 . The three mechanisms are presented in Figure 5.1. We present the description with the multireference CASSCF/CASPT2 method of the C-H bond cleavage over three different binuclear Fe clusters according to the three previously described reaction mechanisms. We also compare the results of the multireference calculations with five popular density functionals.

5.2. COMPUTATIONAL DETAILS

5.2.1. MODEL DEFINITION

THE dissociation of the first C-H bond of methane was modelled by periodic DFT calculations as described in Chapter 2. A binuclear Fe(III) cluster was deposited in ZSM-5 zeolite as counter ion for two framework Al ions in the T7 and T12 position. The Fe atoms are coordinated by u-oxo atoms, H_2O molecules and framework O atoms at their first coordination shell and each Fe atom has a coordination number of 6: $[(\text{H}_2\text{O})_2-\text{Fe}(\text{III})-(\mu\text{O})_2-\text{Fe}(\text{III})-(\text{H}_2\text{O})_2]^{2+}$. Upon reaction with H_2O_2 this cluster forms different active sites that are suitable to catalyse methane oxidation. The CASSCF/CASPT2 calculations were performed on a cluster model created by cutting the Si-O bonds and substituting the dangling O atoms with H atoms at fixed distance from Si (1.4 Å) and Al (1.5 Å) atoms [25, 26]. Two models were cut from the zeolite: a 50-atom and a 99-atom cluster model (Figure 5.2 A and B respectively). Both models contain the 8-membered ring of the zeolite, the active site and the methane molecule and later its derivatives, and the bigger model in addition contains the surrounding framework atoms of the zeolite channel. Single point calculations were performed on the cluster models with Gaussian 09 [27] software PBE [28, 29] correlation and exchange functional, def2tzvp basis set [30, 31] and the DFT-D3(BJ) method [32]. The obtained energy differences were compared with the results of the periodic calculation (Table 5.1). It was concluded, that the small cluster is not sufficient to model the reaction since it cannot account for the interaction of the cluster and molecules with the surrounding zeolite framework. The difference between the periodic and the big cluster model is the result of the missing H bonding interactions between the framework O atoms and the water molecules and the non-explicit treatment of the core electrons in case of the periodic calculations. Therefore, it was decided to continue with the larger model.

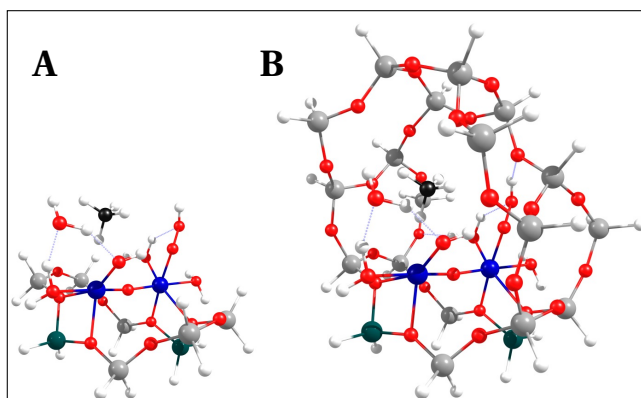


Figure 5.2: Cluster model of a) 57 atom and b) 99 atom zeolite. Colour coding: H: white, C: black, O: red, Fe: blue, Al: green, Si: grey.

5

Table 5.1: Relative energies and their differences of **ITS** (ΔE^a) and **If** (ΔE_R) compared to **1i** in spin state $S = 8/2$ calculated by the periodic, small and large cluster models. The energies are in kJ/mol.

	ΔE^a	ΔE_R
periodic	106	2
small cluster	152	90
big cluster	116	29
$\Delta(\text{small-periodic})$	46	88
$\Delta(\text{big-periodic})$	10	27

5.2.2. DFT CALCULATIONS

Single point calculations were performed on the cluster models with the Gaussian 09 [27] software and the def2tzvp [30, 31] basis set. We chose five popular exchange-correlation functionals: two GGA functionals, OPBE [28, 33] and PBE [28, 29], two meta-GGE functionals, M06L [34] and MN15L [35], and the B3LYP [36] hybrid functional. For PBE Grimme's dispersion correction with Becke-Johnson damping [32] was applied. Integration was carried out using the ultrafine grid with tight convergence criteria. Electronic energy was used to calculate the reaction and activation energy. Partial charges and spin population were determined with the CM5 [37] and Hirshfeld [38] method respectively.

5.2.3. MULTIREFERENCE CALCULATIONS

The complete active space self-consistent field (CASSCF) and restricted active space self-consistent field (RASSCF) methods followed by second-order perturbation theory (CASPT2 and RASPT2, respectively) were employed for the cluster model calculations. In CASSCF, a full-configuration interaction is allowed in a space containing n electrons in m orbitals, this is denoted as $\text{CAS}(n,m)$. In this work, a minimal active space was

determined to be achieved when any orbitals additional to the minimal active space were either doubly occupied or empty ($1.95 < \text{occ nr} < 0.05$). This included the five 3d iron orbitals with the corresponding electrons depending on the oxidation state and in some cases some ligand oxygen p orbitals. The minimum active space was systematically expanded by including one doubly occupied orbital and its correlating orbital at a time. The second shell effects and ligand orbitals were considered expanding the active space to 20 orbitals in some cases. For all active spaces larger than 14 electrons in 14 orbitals, the restricted formalism (RASSCF) was employed, denoted in the same manner to RAS(n, m). In this case the active space is divided in three spaces: RAS1, RAS2 and RAS3. RAS2 space behaves the same way as the CASSCF active space with all configurations possible. RAS1 space contains doubly occupied orbitals, while RAS3 space contains empty orbitals. Double excitations from the RAS1 space to RAS3 space were possible. This restricts the number of possible configurations making the calculations feasible.

The single point calculations were carried out using MOLCAS 8.0 [39, 40] program package. ANO-RCC [41–44] type basis set was used for all atoms: VTZP for Fe; VDZP for methane and the bridging and terminal O(H) groups; and minimal basis set for the rest of the atoms. Cholesky decomposition is used to decompose two-electron integrals All CASPT2 and RASPT2 calculations were performed using an imaginary level shift of 0.2 and an IPEA shift of 0.25. The Hirshfeld spin population [38] and CM5 charges [37] were computed with the MultiWfn package[45].

5.3. RESULTS

IN this section we first describe the oxidation-reduction reactions using formal oxidation states. Then we give a general introduction of the multireference wave functions followed by the description of the active space of our intermediates. These are then compared with the electronic structures obtained by DFT calculations. And finally we present the reaction energies obtained by both CASSCF/CASPT2 and DFT calculations.

5.3.1. DESCRIPTION OF THE REACTIONS

Two distinct mechanism of C-H cleavage occurring via three alternative reaction paths were considered here, namely, the heterolytic (σ -bond metathesis) and two types of homolytic C-H bond dissociations - the rebound and Fenton-type mechanisms. The intermediates are presented in Figure 5.1. The heterolytic reaction path takes place over a $[(\text{H}_2\text{O})_2(\text{HOO})\text{Fe}(\text{III})-\mu\text{O}-\text{Fe}(\text{III})\text{OH}(\text{H}_2\text{O})]^{2+}$ cluster. During the heterolytic reaction a basic OH group of **II** abstracts a proton from the polarized methane

molecule to form H₂O and concomitantly the CH₃ anion is stabilized by the Lewis acidic Fe site. There is no formal oxidation state change along the reaction coordinate, and Fe remains in the +3 and C in -4 oxidation state.

During the homolytic dissociation the OH group of the Fe cluster abstracts an H atom from the methane resulting in the formation of a methyl radical that is not bound with the partially reduced cluster. The di-Fe complex promoting such a homolytic reaction path is [(H₂O)(HO)OFe-μO-Fe(OH)(H₂O)]²⁺, **2i**, which can be formally considered either an Fe(IV)Fe(IV) or an Fe(III)Fe(V) complex. Both these configurations would be characterized by eight unpaired electrons in the high spin state (S = 4). The reaction with methane converts the binuclear Fe(IV) cluster to the partially reduced Fe(III)Fe(IV) state (**2TS**). The high-spin (S = 5) electronic structure of the reaction product (**2f**) is represented by five unpaired 3d electrons on Fe(III), four unpaired 3d electrons on the reduced Fe(IV) site with one more unpaired electron on CH₃ radical species.

5

In the Fenton-type path, the di-Fe active site is indirectly involved in C-H activation. The transition metal in this case catalyses the H₂O₂ activation to form the reactive OH radicals, which, in turn, promote the homolytic C-H cleavage in methane to yield ·CH₃ and H₂O. In the case of the di-Fe complexes in zeolite, both O-O and C-H activations take place consequentially within a single elementary reaction step, in which the former process appears to be most energy demanding. The reaction starts with a binuclear Fe(III) complex bearing an HOO ligand in the first coordination shell of one of the Fe sites [(H₂O)(HOO)Fe-μ(O,OH)-Fe(H₂O)₂]²⁺, and an adsorbed methane molecule (**3i**). In the transition state, the O-O bond of the HOO ligand is cleaved resulting in a transient formation of an OH radical (**3TS**), which readily abstracts an H atom from a vicinal CH₄ molecule to produce water and a methyl radical as the reaction products (**3f**). Along the reaction coordinate several bond-breaking/forming events take place, which are accompanied by changes in the oxidation states: the cleavage of the peroxy-bond entails 1) the oxidation of the cluster to a formally Fe(IV)Fe(III) state, and 2) the reduction of one of the oxygen atoms in the peroxy group from -1 to -2, while the oxidation state of the other peroxy atom forming the OH radical remains unaffected (-1); the formation of the reactive OH radical is followed by 3) the oxidation of methane with C in -4 formal oxidation state to -3 in ·CH₃ with 4) simultaneous reduction of the O atom in OH radical from -1 to -2 state upon the H-abstraction to form H₂O. Overall, the reaction involves the oxidation of one Fe and one C atoms and reduction of two O atoms of the peroxide.

5.3.2. MULTIREFERENCE WAVE FUNCTION AND ACTIVE SPACE DESCRIPTION

During the CASSCF multireference calculations at first usually a Hartree-Fock calculation is performed to obtain the reference wave function. In the next step the orbitals are categorised into doubly occupied, active and empty or virtual orbitals. After this, configuration functions (CFs) are created by the arrangement of the electrons on the active orbitals in all possible configurations. In the next step the multireference calculation is performed, during which the orbitals and the coefficients of the CFs are optimised, and the multireference wave function is created. Each CF has a weight in the wave function, and often one or a few orbitals have a higher weight than the others. These are the dominant configurations. Many molecules, like methane, can be described with a single reference wave function. In this case there is one dominant configuration, and the weight of the rest is negligible. In many cases however, especially in the case of Fe complexes, multiple configurations are necessary to properly describe the wave function.

In the case of molecules containing transition metals it is important to investigate the different spin states. When setting the spin state of a multireference wave function, all the configuration functions have the same spin state. The concept is schematically demonstrated in Figure 5.3 with a representative example of an Fe(III)-O-Fe(III) moiety. There are 5 3d electrons of each Fe atoms, and 2 2p electrons of the O atom in the active space of 11 orbitals. Electrons are placed on the orbitals in different ways representing the configuration functions. A given spin state has CFs of the same spin state. This means, that for example $S = 5$ case will have 11 spin up, and 1 spin down active electrons in each configuration, while $S = 4$ has 10 up, and 2 down spin electrons. Calculating different spin states of a molecule and arranging them based on their energies gives the spin ladder.

In our case each Fe atom can have a maximum local spin state of $5/2$ or $4/2$ in the oxidation state of +3 and +4 respectively. This gives a total of $S = 5$ or $S = 4$ high spin state for a binuclear Fe(III) and Fe(IV) site. The intermediate spin states can be determined from the sum of the intermediate local spin states of the two Fe atoms resulting in $S = 0, 1, 2, 3, 4$ for an Fe(IV)Fe(IV) and additionally 5 for an Fe(III)Fe(III) cluster. The two Fe atoms are coupled through one or two bridging O atoms. This is called super-exchange coupling. This makes it possible for the Fe atoms to interact with each other through this O atom, as it is represented in Figure 5.3. As the spin state decreases, the number of potential CFs increases for the same active space. For example, in the (10,10) active space $S = 5$ spin state there is 1 CF, in $S = 4$ state there are 100, and in $S = 0$ spin state there are 2520 CFs. The number of potential configurations

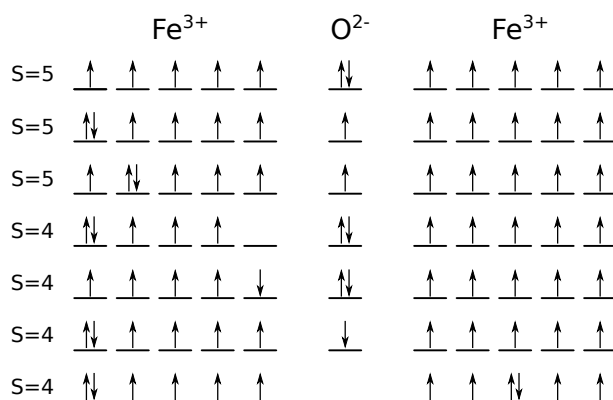


Figure 5.3: Some potential arrangements of 12 electrons on 11 orbitals of an Fe(III)-O-Fe(III) segment in different spin states.

5

also increases with the size of the active space.

With the right combination of so many configurations many types of electronic structures are possible to obtain. This is how it is possible for an intermediate to have near identical electronic structure in the different spin states, which is the situation in our case. The ground state is the $S = 0$ spin state for all intermediates, and the energy increases with the spin state until the $S = 4$ or $S = 5$ high spin state. This will be further elaborated in the next chapters.

HETEROLYTIC DISSOCIATION

The minimal active space for reactant (**1i**), transition state (**1TS**), and products (**1f**) consists of 10 electrons of the 10 3d orbitals of both iron atoms as depicted in Figure 5.4, 5.5 and 5.6 respectively for the initial, transition and final state. The occupation numbers for all intermediates with the various spin states span between 0.9 and 1.1. Excluding the high spin state ($S = 5$), which contains one unique configuration on the CAS(10,10), no dominant configuration was identified for the other spin states. The most important configurations and their weights of **1i** in $S = 4$ spin state with (10,10) active space is shown in Table 5.2. As it can be seen, there is no dominant configuration, but 10 with very similar weights. In each configuration there are 8 singly occupied orbitals, one full, and one empty. The CFs can be arranged in pairs, and in each pair, there is an excitation of two electrons from the doubly occupied orbital to the empty. This is how it is possible to obtain 10 nearly singly occupied orbitals with the combination of $S = 4$ configuration functions. As we go down in spin state, and in the spin ladder, the weight of the highest configuration decreases, in $S = 3$ spin state it is only 3%, while for $S = 0$ it is less, than 1%. All spin states of all three intermediates have a similar electronic structure: 10 nearly singly occupied orbitals

mainly constituted of Fe 3d atomic orbitals with some small contributions from the ligands, mainly from the bridging O.

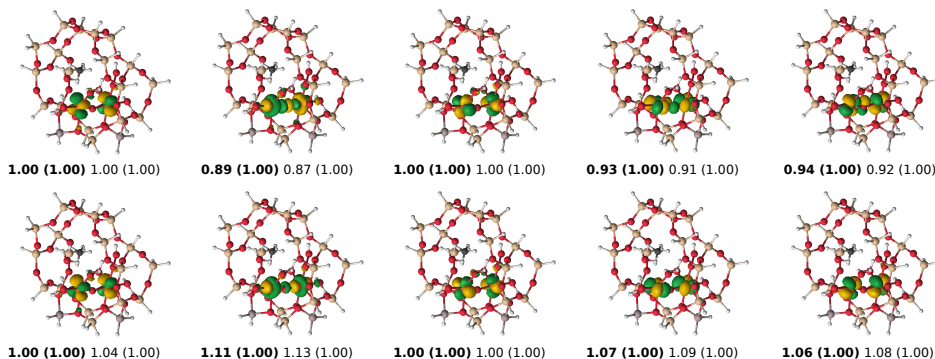


Figure 5.4: CASSCF natural orbitals of the minimal active space of CAS(10,10) for the ground state ($S = 0$) structure for the reactant (**II**) of the heterolytic dissociation of C-H bond. Occupation numbers are shown below the structures: CAS(10,10) $S = 0$, (CAS(10,10) $S = 5$), RAS(16,16) $S = 0$, (RAS(16,16) $S = 5$)

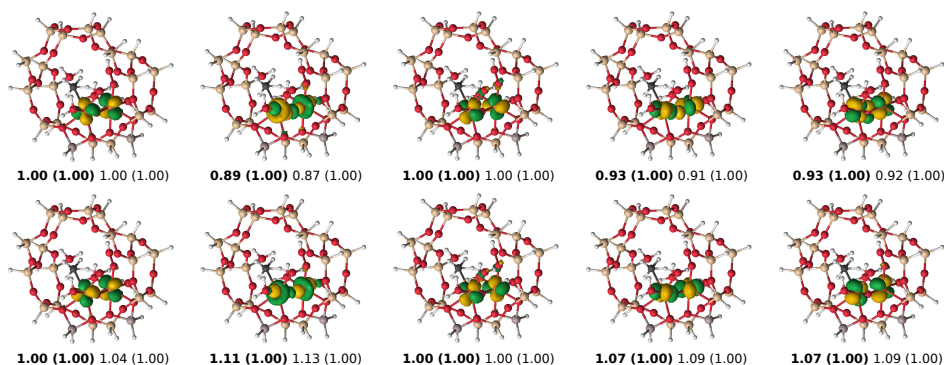


Figure 5.5: CASSCF natural orbitals of the minimal active space of CAS(10,10) for the ground state ($S = 0$) structure for the transition state (**ITS**) of the heterolytic dissociation of C-H bond. Occupation numbers are shown below the structures: CAS(10,10) $S = 0$, (CAS(10,10) $S = 5$), RAS(16,16) $S = 0$, (RAS(16,16) $S = 5$)

Subsequently, the active space was extended starting from the CAS(10,10) wave function by adding stepwise 2 electrons and 2 orbitals until an active space of 20 electrons in 20 orbitals was reached. From CAS(16,16) active space RASSCF/RASPT2 calculations were conducted with the (10,10) minimal active space being in the RAS2 space, and equal number of orbitals in the RAS1 and RAS3 spaces with two holes and two excitations. All the orbitals not belonging to the minimal active space were either doubly occupied ($occ\ nr > 1.95$) or empty ($occ\ nr < 0.05$). The additional orbitals that appeared first were the 2s, 2p doubly occupied and correlating second shell empty orbitals (3s and 3p) of the bridging O. An additional orbital pair appeared

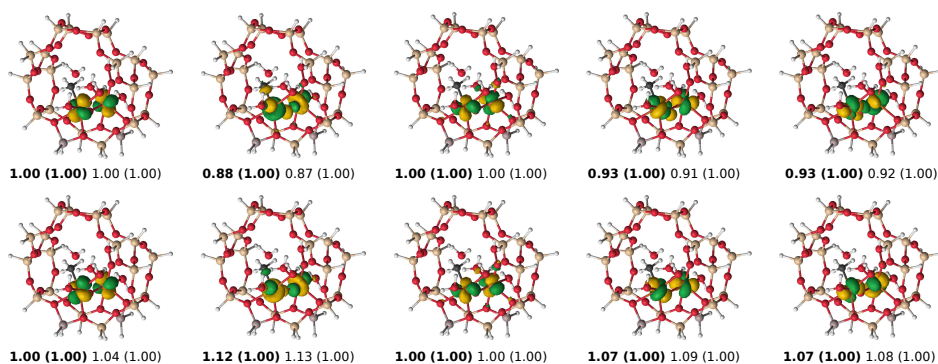


Figure 5.6: CASSCF natural orbitals of the minimal active space of CAS(10,10) for the ground state ($S = 0$) structure for the product (**1f**) of the heterolytic dissociation of C-H bond. Occupation numbers are shown below the structures: CAS(10,10) $S = 0$, (CAS(10,10) $S = 5$), RAS(16,16) $S = 0$, (RAS(16,16) $S = 5$)

Table 5.2: Configurations and their weights with a CI-coefficient larger than 0.01 for **1i** $S = 4$ (10,10) active space. 2 means double occupied orbital, 0 means empty orbital and u means singly occupied orbital with a spin up electron on it.

Configuration	Weight
uuu2uuuu0u	12.0%
0uuu2uuuuu	11.2%
u0uuuu2uuu	11.0%
uu0uu2uuuu	9.8%
uuuuuu2u0	9.8%
uu2uu0uuuu	9.8%
uuuuuu0u2	9.8%
u2uuuu0uuu	9.0%
2uuu0uuuuu	8.9%
uuu0uuuu2u	8.6%

in the transition state corresponding to the C-H-O atoms in the RAS1 and RAS3 spaces.

The near integer occupation number (0, 1 or 2) of all orbitals indicate that the $S = 5$ high spin state case can be described with non-multireference methods, such as DFT.

HOMOLYTIC DISSOCIATION

For all intermediates a minimal active space of CAS(12,12) was found (Figure 5.7, 5.8, and 5.9). In the initial state (**2i**) they are a mixture of Fe ten 3d, one bridging O 2p and one terminal O 2p orbitals. The Fe centres formally bring 8 electrons, while the O ligand 2-2 electrons. In the transition (**2TS**) and final (**2f**) state, as the CH_3 radical is formed, a C 2p orbital swaps with one Fe 3d orbital, which can be found in the doubly occupied inactive space. This agrees with the expected reduction of the Fe centre. Also, it indicates that the original cluster in **2i** is not Fe(IV)Fe(IV), but formally Fe(V)Fe(III) that is reduced to Fe(V)Fe(II), hence the doubly occupied 3d orbital. This is further

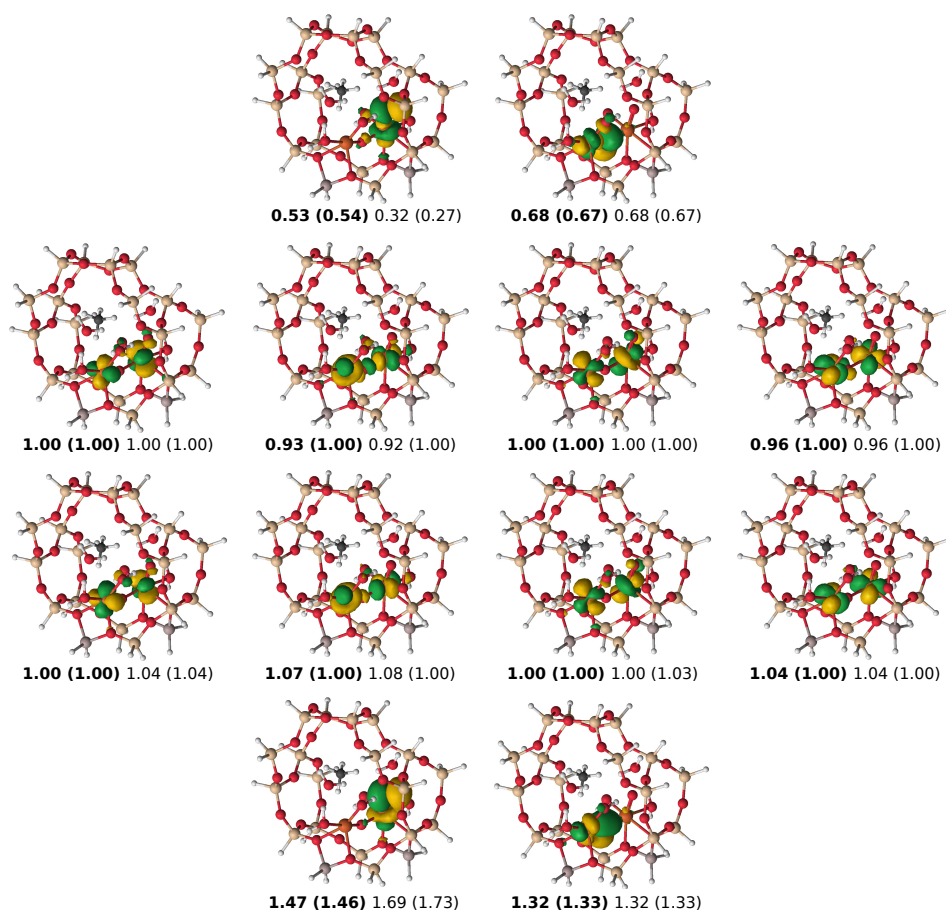


Figure 5.7: CASSCF natural orbitals of the minimal active space of CAS(12,12) for the ground state ($S = 0$) structure for the reactant (**2i**) of the homolytic dissociation of C-H bond. Occupation numbers are shown below the structures: CAS(12,12) $S = 0$, (CAS(12,12) $S = 4$), RAS(16,16) $S = 0$, (RAS(16,16) $S = 4$)

discussed in the next section. The C 2p orbital of the CH_3 radical participates in four orbitals mixing with Fe 3d and in the transition state O 2p orbitals. These orbitals are singly occupied. In **2i** eight orbitals are singly occupied, while the other four orbitals mainly consist of the O 2p atomic orbitals forming a bonding-antibonding pair with a non-integer (not 0, 1 or 2) occupation number. The case of **2TS** and **2f** is very similar, however as the spin state of each intermediate increases, the occupation number of the Fe-O-Fe orbital pair is getting closer to zero, and finally it is singly occupied in the high spin $S = 5$ state.

The highest-weight configurations of the high spin ($S = 4$) **2i** (12,12) intermediate is presented in Table 5.3. The first 16 configurations have the same 8 orbitals singly occupied. These are the singly occupied orbitals in the second and third row of Figure 5.7.

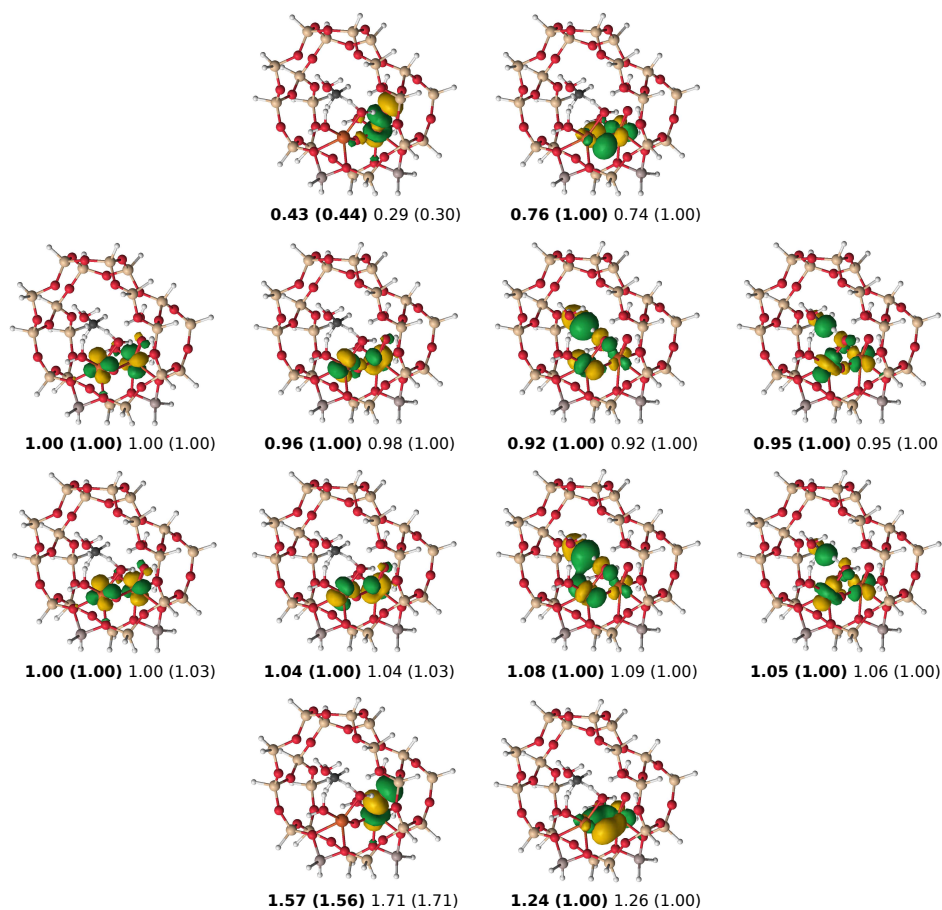


Figure 5.8: CASSCF natural orbitals of the minimal active space of CAS(12,12) for the ground state ($S = 0$) structure for the transition state (2TS) of the homolytic dissociation of C-H bond. Occupation numbers are shown below the structures: CAS(12,12) $S = 0$, (CAS(12,12) $S = 5$), RAS(16,16) $S = 0$, (RAS(16,16) $S = 5$)

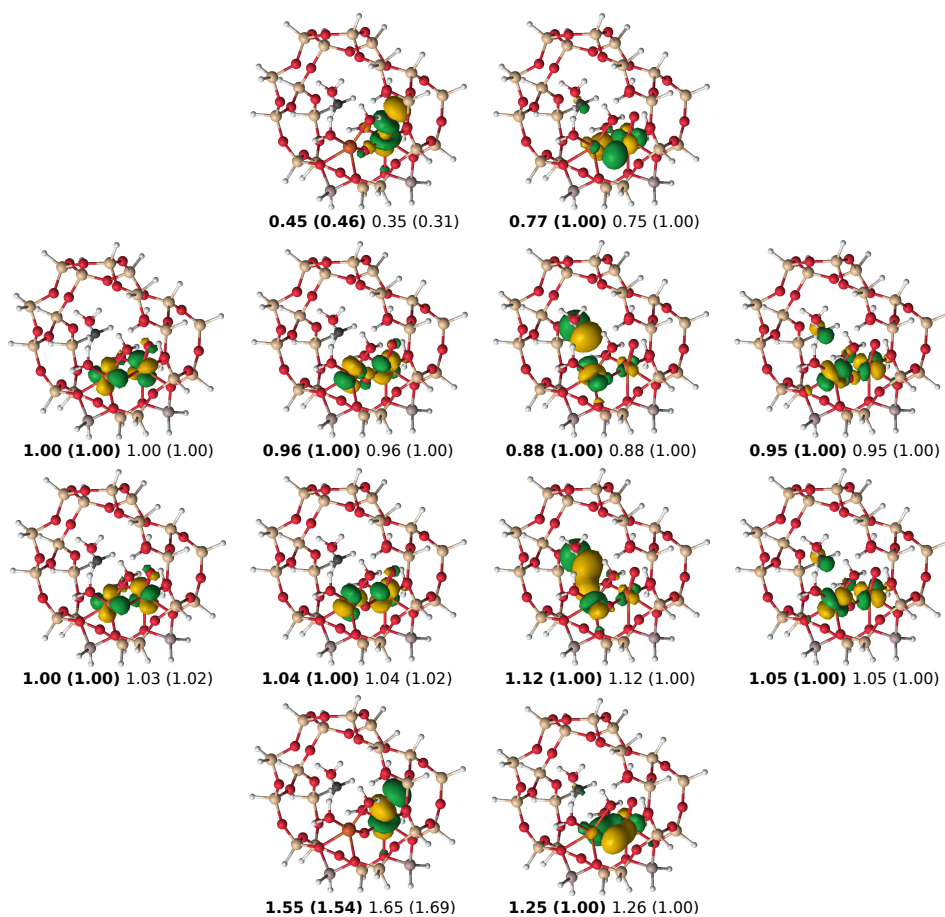


Figure 5.9: CASSCF natural orbitals of the minimal active space of CAS(12,12) for the ground state ($S = 0$) structure for the product (2f) of the homolytic dissociation of C-H bond. Occupation numbers are shown below the structures: CAS(12,12) $S = 0$, CAS(12,12) $S = 5$, RAS(16,16) $S = 0$, RAS(16,16) $S = 5$

The other four orbitals belong to the Fe=O and the Fe-O-Fe bonding-antibonding pairs. The different configurations represent one or two electron excitations from the bonding to the antibonding orbitals. These 16 configurations sum up to almost 88% of the wave function with the highest being 32% and the lowest below 1%. This means, that unlike in the case of Fe(III)Fe(III) clusters, there is no single dominant configuration that could describe well the wave function in the high spin state.

The third and fourth columns of the same Table 5.3 show the first 4 most important configurations of the transition state, **2TS** in the high spin. In this case there are 10 singly occupied orbitals, and one orbital pair with non-integer occupation number. In the four configurations presented here these 10 singly occupied orbitals are indeed singly occupied, and the excitation of one or two electrons from the bonding to the antibonding orbital occurs. These four configurations constitute almost 96% of the multireference wave function. There is a dominant configuration with almost 70% weight, which describes the situation of 10 singly occupied orbitals, a full Fe=O bonding orbital and an empty antibonding orbital. A similar situation is true for the high spin of **2f**.

Table 5.3: Configurations with the highest weight for **2i** S = 4 (12,12) active space and **2TS** S = 5 (12,12) active space. 2 means double occupied orbital, 0 means empty orbital, u means singly occupied orbital with a spin up electron on it, and d means singly occupied orbital with a spin down electron on it.

2i S = 4		2TS S = 5	
Configuration	Weight	Configuration	Weight
uuuuu022uu0u	32.0%	uuuuu2uuu0uu	69.5%
uuuuu202uu0u	11.3%	uuuuu0uuu2uu	13.8%
uuuuudu2uu0u	8.5%	uuuuuduuuuuu	6.8%
uuuuu020uu2u	8.2%	uuuuuuuuudu	5.5%
uuuuud2uu0u	6.0%	Sum	95.6%
uuuuu02duuuu	4.5%		
uuuuu02uuudu	3.7%		
uuuuu200uu2u	3.0%		
uuuuudu0uu2u	2.2%		
uuuuud0uu2u	1.6%		
uuuuu20duuuu	1.6%		
uuuuu20uuudu	1.3%		
uuuuududuuuu	1.1%		
uuuuuduuduudu	1.0%		
uuuuudduuuu	0.8%		
uuuuuduuduudu	0.7%		
Sum	87.5%		

As it was explained for the heterolytic dissociation, with the decrease of the spin state

the weight of the most dominant configuration decreases, for example **2TS** (12,12) in the $S = 4$ spin state has the highest weight of 20%, and in $S = 3$ state below 5% and so on until below 1% in $S = 0$ state. With the combination of all these configurations it is possible to have similar electronic configuration in the different spin states.

The minimal active space was further expanded by adding stepwise two electrons and two orbitals starting from (12,12) until (18,18). Active spaces of (16,16) or larger were treated with the RASSCF/RASPT2 method starting with the orbitals from CAS(12,12) in RAS2 space. The additional orbitals correspond to 2s, 2p and 3s, 3p orbitals of the terminal oxygen with occupation numbers ranging between 1.96 and 2.00, and 0.00 and 0.03, respectively.

FENTON-TYPE ACTIVATION

Structure **3i** is an Fe(III)Fe(III) cluster similar to **1i**. Therefore they have similar electronic configuration (Figure 5.10), which means that the minimal active space is CAS(10,10) consisting of 10 singly occupied Fe 3d orbitals. The increase of the minimal active space also results in similar orbitals: the bridging O 2s, 2p and 3s, 3p orbitals appear in the active space as doubly or empty orbitals, respectively. The configurations are also similar: in $S = 5$ high spin state there is one possibility, and by extending the active space there will be one dominant configuration. In the smaller spin states there is no dominant configuration, and the weight of the highest weight configuration decreases with around 1% in $S = 0$ spin state.

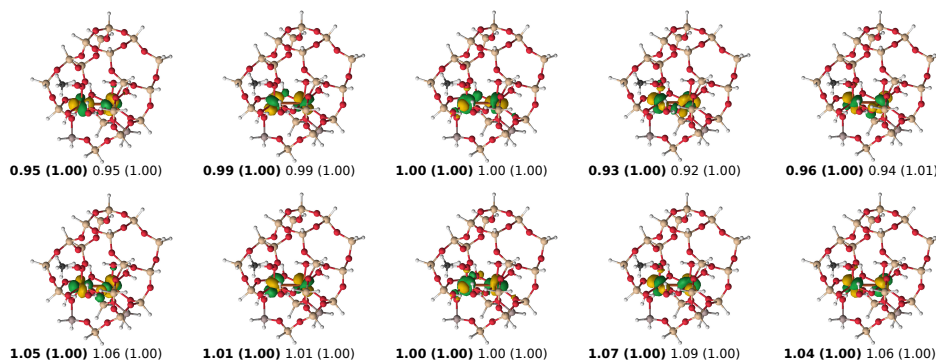


Figure 5.10: CASSCF natural orbitals of the minimal active space of CAS(10,10) for the ground state ($S = 0$) structure for the reactant (**3i**) of the Fenton-type dissociation of C-H bond. Occupation numbers are shown below the structures: CAS(10,10) $S = 0$, CAS(10,10) $S = 5$, RAS(16,16) $S = 0$, RAS(16,16) $S = 5$

On the other hand, the electronic configuration of **3TS** and **3f** (Figure 5.11 and 5.12) are very different from that of the heterolytic reaction, because in this case there is oxidation state change along the reaction, and the Fe(III) clusters are oxidized while

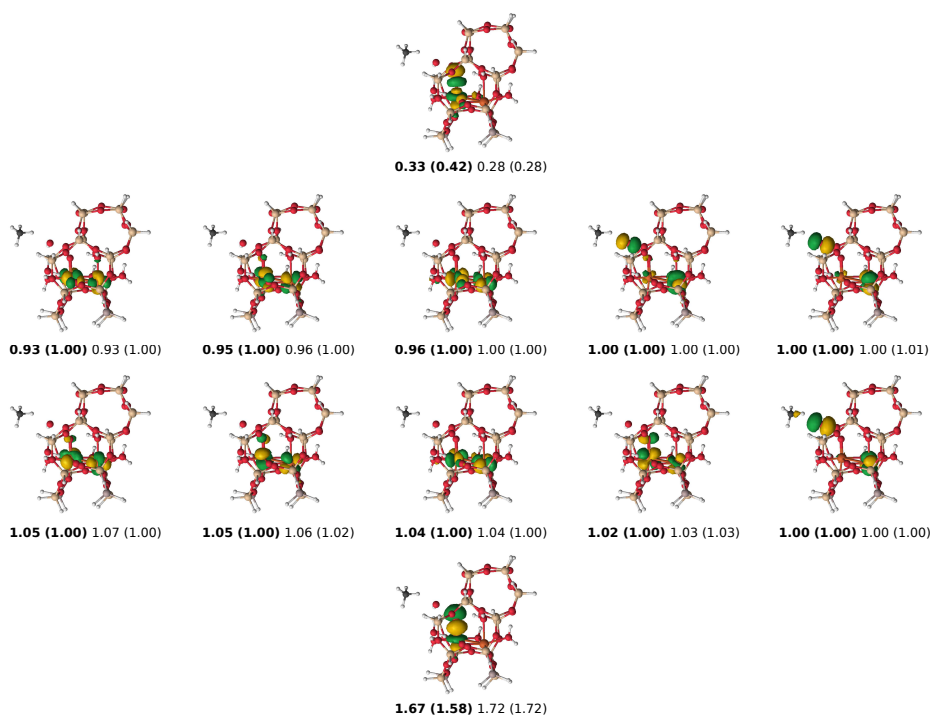


Figure 5.11: CASSCF natural orbitals of the minimal active space of CAS(12,12) for the ground state ($S = 0$) structure for the transition state (**3TS**) of the Fenton-type dissociation of C-H bond. Occupation numbers are shown below the structures: CAS(12,12) $S = 0$, (CAS(12,12) $S = 5$), RAS(16,16) $S = 0$, (RAS(16,16) $S = 5$)

radicals are formed.

3TS has a CAS(12,12) minimal active space: 9 e- on 10 3d orbitals of the Fe atoms, 1 e- on 1 2p orbital of the OH radical and 2 e- on 1 2p orbital of the terminal O. Ten of these orbitals are singly occupied, while the Fe(3d_{z²})=O(2p_z) bonding-antibonding orbital pair has non-integer occupation numbers. **3f** has a similar minimal active space, but the 2p orbital of the OH radical swaps with the 2p orbital of the C atom of the methyl radical. Again, the orbitals with the partial occupation numbers indicate that a multireference wave function is needed for the proper description of the system.

The configuration are also similar to that of **2TS** and **2f**. In the high spin state there are a few configurations that constitute more than 70% of the multireference wave function. 10 of these orbitals are singly occupied, these are the orbitals in the second and third row in Figure 5.11 and 5.12. The other two have different occupation numbers in the different configurations representing the excitation of one or two electrons from the bonding to the antibonding orbitals.

Expanding the active space of **3i** stepwise by two electrons and two orbitals has the

HETEROLYTIC DISSOCIATION

In Figure 5.13 A-C the active space convergence of reactant (**1i**), transition state (**1TS**), and product (**1f**) are depicted with reference to the minimal active space of (10,10) in the ground spin state ($S = 0$). The relative energies increase with the active space size, reaching a plateau around (14,14). For the three intermediates under investigation, the low spin state remains the ground spin state with a separation to the high spin state of about 60 kJ/mol. These HS-LS gaps decrease with the increasing active space size. Henceforth, the (14,14) active space is selected as suitable active space to compare with density functional results.

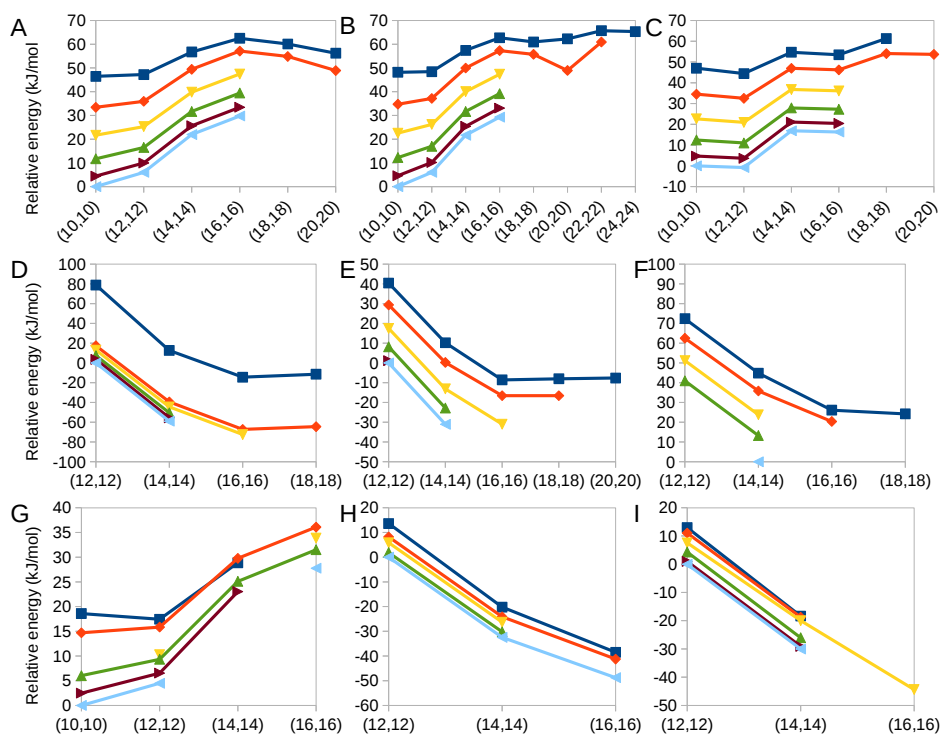


Figure 5.13: Electronic CASPT2 and RASPT2 energy convergence relative to the lowest active space CASSCF/CASPT2 energy in singlet spin state calculations. A: **1i**; B: **1TS**; C: **1f**; D: **2i**; E: **2TS**; F: **2f**; G: **3i**; H: **3TS**; I: **3f**. Colours: S = 0 (BS for DFT): light blue, S = 1: yellow, S = 2: brown, S = 3: green, S = 4: orange, S = 5: dark blue

HOMOLYTIC DISSOCIATION

In Figure 5.13 D-F CASPT2 energy convergence as the function of the active size is plotted against the active space size. The CASPT2 energies decrease for larger active space finding a plateau around (16,16). For **2i** no convergence was reached for calculations with an active space larger than (16,16), while calculations of certain

spin states of **2TS** and **2f** converge with active space (18,18) and (20,20) as well. In this reaction, the ground spin state corresponds to the singlet ($S = 0$), for higher spin states the energy increases accordingly. However, a large energy gap was encountered between $S = 4$ and $S = 5$ for **2i**, as the formal oxidation state of Fe is +4 thus the high spin state is $S = 4$. This energy gap difference disappears in the transition state making the $S = 5$ the high spin state. The HS-LS gap, in contrast with the previous case, is independent from the active space size. For comparison with DFT the (16,16) high spin state space was chosen, and (14,14) for the low spin state, as no convergence was obtained for those calculations.

FENTON-TYPE DISSOCIATION

Figure 5.13 G-I shows how the energy converges as the function of the active space size. The initial state (**3i**) shows the same trend as the heterolytic dissociation case: 1) the energy increases, and 2) the energy gap between the spin states decreases with the active space size. On the other hand, the energy of **3TS** and **3f** decreases as the function of the active space size, and the spin ladder is independent of it. As the energy of **3i** increases, while the energy of **3TS** and **3f** decreases with the size of the active space, the activation and reaction energy very much depend on the chosen active space. As the calculations with the higher active space did not converge within the available time frame, we don't have a choice but to present the results at the (14,14) active space. These numbers however are not suitable for quantitative comparison.

5.3.4. COMPARISON OF THE ELECTRONIC STRUCTURE OBTAINED BY CASSCF AND DFT

Based on the analysis of the previous section in general it can be said that the intermediate spin states calculated by DFT have no chance to describe the same electronic structures as the MR wave function does, because there are many CFs with low weight constituting the wave function without a dominant configuration. On the other hand, the MR method predicts at least 10 or 8 singly occupied molecular orbitals with often a dominant configuration being present in the high spin state, so we are going to focus on the comparison between the high spin states of CASSCF and DFT.

The ground state of all intermediates is $S = 0$, the low spin state. The MR wave functions of all intermediates in the $S = 0$ state consist of thousands of small weight configurations with the highest being below 1.5%. In DFT it is possible to perform broken symmetry calculations. This means, that the total spin state is 0, so there is equal spin up and spin down electrons, however they are not paired. This way it is possible to obtain a similar electronic configuration to that of the high spin

state. Broken symmetry method is often recommended for binuclear transition metal clusters where the ground state is singlet. For this reason, we are also going to examine how well the broken symmetry method can describe the electronic configuration.

At this point it is important to talk about spin contamination. The degree of spin contamination can be assessed by inspection of the deviation of the expectation value of S^2 from the theoretical value. In DFT KS formalism the Slater determinant that is formed from the KS orbitals is the exact wave function for the fictional non-interacting system having the same density as the real system. Spin contamination of a KS-DFT calculation is calculated with the use of this wave function. Although this number is not the expectation value for S^2 of the exact wave function of the interacting system, it is often used as an indication to determine whether a system needs multireference treatment. As a rough rule it is said that if the spin contamination is higher than 5-10% than we are dealing with a system that cannot be described by a single-determinant method.

5

In the case of all investigated intermediates there is a high spin contamination for spin state 0,1 and 2 (TABLES). This is in agreement with the previous paragraph and our analysis of the CASSCF wave functions. However above $S = 2$ the level of spin contamination is below 0.1%, indicating that the systems can be described by single-determinant methods. This is however obviously not true, as we show, that with the exception of the Fe(III)Fe(III) clusters in the high spin state all intermediates in all spin states need multireference methods to be correctly described.

HETEROLYTIC DISSOCIATION

There is one dominant configuration in the $S = 5$ high spin case for all three intermediates. The weight of it in the active spaces bigger than (10,10) is above 99%. This describes an electronic structure of 10 singly occupied orbitals in the active space. DFT $S = 5$ high spin and $S = 0$ broken symmetry are able to produce a density function with ten singly occupied orbitals potentially similar to those of the CASSCF calculations.

To further investigate the similarities and differences of the DFT and the MR electronic structure, the Hirshfeld spin densities and CM5 charges are shown in in Table 5.4 and 5.5 and Figure 5.14 and 5.15. The BS, the $S = 5$ and $S = 4$ spin states are compared with the results obtained from the MR calculations.

CASSCF predicts near equal spin density of the Fe atoms for all intermediates, some small (~ 0.3) spin density on the bridging O and no spin density on the C initially and in the transition state, which increases to 0.1 in the final state. The partial charges

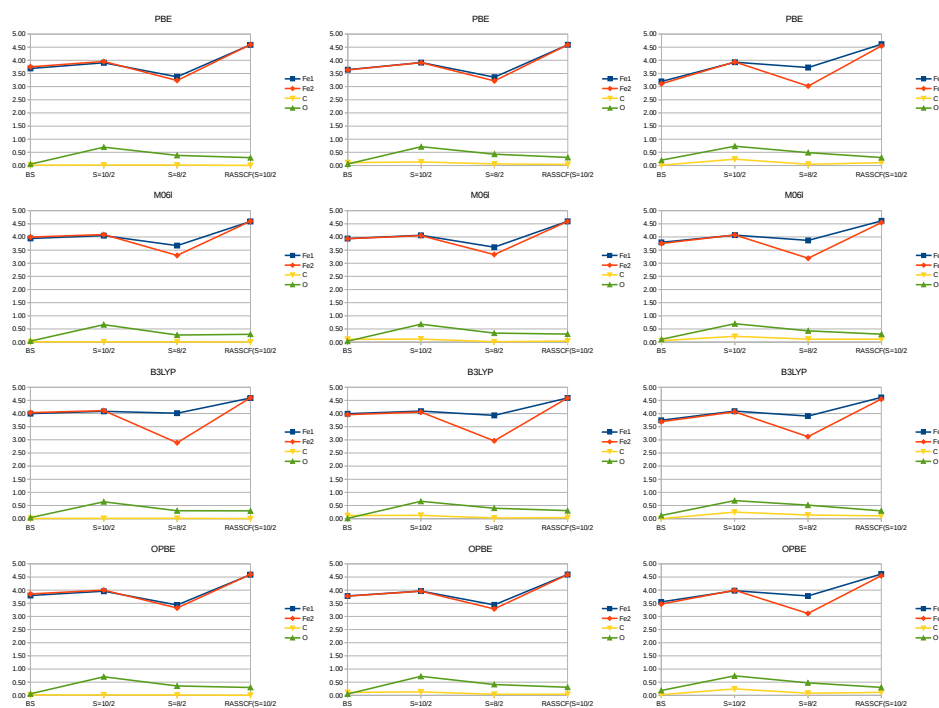


Figure 5.14: The absolute values of Hirshfeld spin densities of **ii**, **ITS** and **If** calculated by different functionals and RASSCF/RASPT2(16,16). Spin states $S = 5$, 4 and broken symmetry 0 are presented for the functionals, and $S = 5$ for the MR calculation. The values of the two Fe atoms, the bridging O and the C of methane are presented.

Table 5.4: Hirshfeld spin densities of **ii**, **ITS** and **If** calculated by different functionals and RASSCF/RASPT2. Spin states $S = 5$, 4 and broken symmetry 0 are presented for the functionals, and $S = 5$ for the MR calculation. The values of the two Fe atoms, the bridging O and the C of methane are presented.

		ii				ITS				If			
		BS	$S = 10/2$	$S = 8/2$	RASSCF $S = 10/2$ (16,16)	BS	$S = 10/2$	$S = 8/2$	RASSCF $S = 10/2$ (16,16)	BS	$S = 10/2$	$S = 8/2$	RASSCF $S = 10/2$ (16,16)
pbe	Fe1	3.69	3.91	3.37	4.59	3.64	3.92	3.36	4.59	3.20	3.93	3.73	4.61
	Fe2	-3.75	3.96	3.23	4.60	-3.64	3.91	3.22	4.59	-3.11	3.94	3.02	4.55
	C	-0.01	0.02	0.02	0.00	-0.10	0.13	0.06	0.04	0.01	0.24	-0.04	0.11
	O	-0.05	0.70	0.38	0.30	-0.06	0.71	0.43	0.31	-0.20	0.73	0.49	0.30
m06l	Fe1	3.94	4.05	3.67	4.59	3.94	4.06	3.61	4.59	3.80	4.07	3.87	4.61
	Fe2	-4.00	4.09	3.30	4.60	-3.93	4.05	3.33	4.59	-3.75	4.08	3.19	4.55
	C	-0.01	0.01	0.01	0.00	-0.11	0.12	0.01	0.04	-0.06	0.22	-0.11	0.11
	O	-0.04	0.66	0.27	0.30	-0.03	0.68	0.34	0.31	-0.10	0.70	0.43	0.30
b3lyp	Fe1	4.00	4.08	4.01	4.59	3.99	4.09	3.93	4.59	3.74	4.09	3.90	4.61
	Fe2	-4.04	4.11	2.89	4.60	-3.96	4.06	2.96	4.59	-3.69	4.07	3.12	4.55
	C	-0.01	0.01	0.01	0.00	-0.12	0.13	-0.03	0.04	-0.01	0.25	-0.14	0.11
	O	-0.04	0.64	0.30	0.30	-0.01	0.66	0.40	0.31	-0.12	0.69	0.52	0.30
opbe	Fe1	3.80	3.96	3.44	4.59	3.78	3.97	3.44	4.59	3.55	3.98	3.78	4.61
	Fe2	-3.86	4.00	3.32	4.60	-3.78	3.96	3.29	4.59	-3.47	4.00	3.11	4.55
	C	-0.01	0.01	0.01	0.00	-0.11	0.13	0.04	0.04	-0.02	0.24	-0.08	0.11
	O	-0.05	0.70	0.36	0.30	-0.05	0.72	0.41	0.31	-0.18	0.74	0.48	0.30

on the two Fe atoms are the same in the initial and final structure and have a small

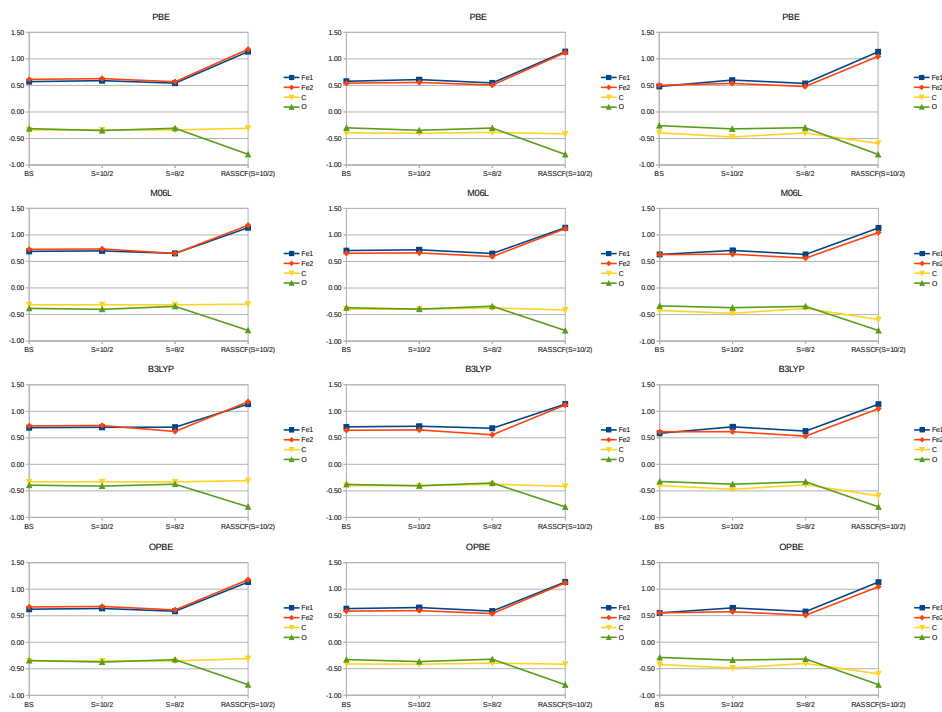


Figure 5.15: CM5 partial charges of **ii**, **ITS** and **If** calculated by different functionals and RASSCF/RASPT2(16,16). Spin states $S = 5, 4$ and broken symmetry 0 are presented for the functionals, and $S = 5$ for the MR calculation. The values of the two Fe atoms, the bridging O and the C of methane are presented.

Table 5.5: CM5 partial charges of **ii**, **ITS** and **If** calculated by different functionals and RASSCF/RASPT2. Spin states $S = 5, 4$ and broken symmetry 0 are presented for the functionals, and $S = 5$ for the MR calculation. The values of the two Fe atoms, the bridging O and the C of methane are presented.

		ii				ITS				If			
		BS	S = 10/2	S = 8/2	RASSCF S = 10/2 (16,16)	BS	S = 10/2	S = 8/2	RASSCF S = 10/2 (16,16)	BS	S = 10/2	S = 8/2	RASSCF S = 10/2 (16,16)
pbe	Fe1	0.57	0.59	0.54	1.14	0.58	0.61	0.55	1.14	0.48	0.60	0.54	1.13
	Fe2	0.61	0.63	0.57	1.18	0.54	0.56	0.51	1.12	0.50	0.54	0.48	1.05
	C	-0.34	-0.34	-0.34	-0.31	-0.39	-0.40	-0.39	-0.41	-0.39	-0.47	-0.40	-0.59
	O	-0.31	-0.35	-0.31	-0.80	-0.30	-0.35	-0.30	-0.80	-0.26	-0.32	-0.30	-0.80
m06l	Fe1	0.69	0.70	0.65	1.14	0.71	0.72	0.65	1.14	0.63	0.71	0.63	1.13
	Fe2	0.73	0.73	0.65	1.18	0.66	0.66	0.59	1.12	0.63	0.64	0.56	1.05
	C	-0.32	-0.32	-0.32	-0.31	-0.40	-0.40	-0.38	-0.41	-0.42	-0.48	-0.38	-0.59
	O	-0.38	-0.40	-0.35	-0.80	-0.37	-0.40	-0.34	-0.80	-0.34	-0.37	-0.34	-0.80
b3lyp	Fe1	0.69	0.70	0.70	1.14	0.71	0.72	0.68	1.14	0.59	0.71	0.63	1.13
	Fe2	0.73	0.73	0.62	1.18	0.64	0.65	0.56	1.12	0.61	0.61	0.53	1.05
	C	-0.33	-0.33	-0.33	-0.31	-0.40	-0.40	-0.37	-0.41	-0.40	-0.47	-0.38	-0.59
	O	-0.39	-0.41	-0.37	-0.80	-0.38	-0.40	-0.35	-0.80	-0.32	-0.37	-0.33	-0.80
opbe	Fe1	0.62	0.64	0.59	1.14	0.63	0.65	0.59	1.14	0.55	0.65	0.58	1.13
	Fe2	0.67	0.68	0.61	1.18	0.59	0.60	0.54	1.12	0.55	0.57	0.51	1.05
	C	-0.35	-0.35	-0.35	-0.31	-0.41	-0.41	-0.39	-0.41	-0.42	-0.49	-0.40	-0.59
	O	-0.34	-0.37	-0.33	-0.80	-0.33	-0.36	-0.32	-0.80	-0.29	-0.34	-0.31	-0.80

deviation in the final state. This confirms that two Fe atoms of **ii** are identical, it

is indeed an Fe(III)Fe(III) cluster. Further in the reaction although formally there is no oxidation state change, the partial charge of the Fe to which the methyl group is connected decreases from 1.18 to 1.05, which means that the ligand H₂O molecule and the methyl group are together less electronegative than the OH group.

DFT $S = 5$ predicts the same trend for the Fe and C atoms as CASSCF, which is equal spin density on the Fe atoms, and some small spin density on the bridging O in all intermediates, and some small spin density on the C atom in **1f**. $S = 0$ describes correctly the spin density of the Fe atoms and the C, however it predicts 0 on the bridging O. The CM5 charges of Fe atoms of **1i** and **1TS** also agree with the MR results in both the $S = 5$ and $S = 0$ spin state. However $S = 5$ of **1f** cannot describe the electronegativity difference between the Fe atoms correctly. C and O are however not correctly predicted. According to CASSCF the bridging O is more negatively charged than C in all three intermediates, and the partial charge of C drops in **1i**, but remains less negative than the O atom. During the course of the reaction the partial charge of O remains constant, while the partial charge of C decreases. On the other hand DFT predicts C and O to have almost the same partial charge in the **1i** intermediate. And in **1TS** and **1f** the partial charge of C is lower instead of higher than the partial charge of O.

Spin state $S = 4$ is also presented to demonstrate that intermediate spin states cannot predict the electronic structure. There is less spin density on the Fe atoms and deviation between the spin densities of the Fe atoms.

The different functionals have the same trends, and very similar absolute values. There are a few exceptions in the intermediate $S = 4$ spin state, for example PBE and OPBE predict the two Fe atoms of structure **1i** to have equal spin densities, while M06L and B3LYP do not. The absolute values of spin densities calculated by all functionals significantly differ from the values calculated by CASSCF. The closest ones are M06L and MN15L with ~ 4 vs ~ 4.5 . The partial charges are even more independent of spin state and functional and the CASSCF predicts much greater polarization than DFT.

HOMOLYTIC DISSOCIATION

The MR method predicts a minimal active space of (12,12), out of which 8 orbitals are singly occupied, and there are two bonding-antibonding orbital pairs containing Fe 3d and O p_z orbitals with a non-integer number of electrons on them. In the high spin state of **2TS** and **2f** there are 10 singly occupied, and two partially occupied orbitals. The highest weight of **2i** $S = 4$ high spin state is 32%, while the highest weights of **2TS** and **2f** $S = 5$ high spin state are 69 and 68%. These configurations can be described by DFT, however as they are significantly below 100%, it is insufficient to describe the

electronic configuration by single reference methods. Neither of the functionals and spin states can correctly capture the electronic structure. For further demonstration let's look at the Hirshfeld spin densities and CM5 charges in Table 5.6 and 5.7 and Figure 5.16 and 5.17.

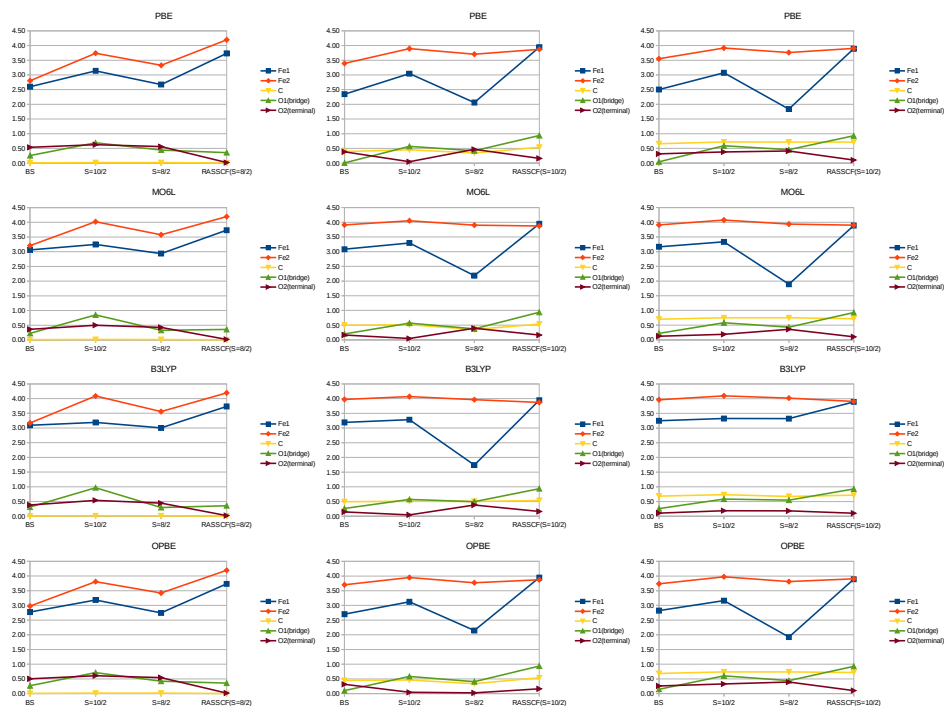


Figure 5.16: The absolute values of Hirshfeld spin densities of **2i**, **2TS** and **2f** calculated by different functionals and RASSCF/RASPT2. Spin states $S = 5, 4$ and broken symmetry 0 are presented for the functionals, and $S = 4$ for **2i** and $S = 5$ for **2TS** and **2f** for the MR calculation. The values of the two Fe atoms, the bridging (O1) and the terminal (O2) and the C of methane are presented.

CASSCF predicts different spin densities of Fe atom of **2i** intermediate. This implies, that the cluster is indeed not an Fe(IV)Fe(IV) site, but rather an Fe(III)Fe(V). However the partial charge on the two Fe atoms is almost identical. This implies that Fe does not want to be in +5 oxidation state, and gets electron density from its ligands. This is in agreement with the way less partial charge (-0.4 vs -0.8) on the bridging O compared to **1i**. During the H atom abstraction formally, Fe(III) is further reduced to Fe(II) while Fe(V) remains unaffected. The calculations however show that while the number of unpaired electrons of Fe(III) decreases, this is in line with getting the 6th electron paired up, the number of unpaired electrons on Fe(V) increases, which indicates, that the new electron is shared between the two atoms. In total 9 electrons are distributed,

Table 5.6: Hirshfel spin densities of **2i**, **2TS** and **2f** calculated by different functionals and RASSCF/RASPT2. Spin states $S = 5$, 4 and broken symmetry 0 are presented for the functionals, and $S = 4$ for **2i** and $S = 5$ for **2TS** and **2f** for the MR calculation. The values of the two Fe atoms, the bridging (O1) and the terminal (O2) and the C of methane are presented.

		2i				2TS				2f			
		BS	$S = 10/2$	$S = 8/2$	RASSCF $S = 8/2$ (16,16)	BS	$S = 10/2$	$S = 8/2$	RASSCF $S = 10/2$ (16,16)	BS	$S = 10/2$	$S = 8/2$	RASSCF $S = 10/2$ (16,16)
pbe	Fe1	2.60	3.14	2.67	3.73	2.35	3.04	2.06	3.95	2.50	3.07	1.84	3.89
	Fe2	-2.80	3.74	3.33	4.19	-3.39	3.90	3.70	3.87	-3.55	3.92	3.76	3.90
	C	-0.01	0.02	0.02	0.00	0.39	0.45	0.34	0.54	0.66	0.72	0.72	0.72
	O1	-0.26	0.69	0.45	-0.36	0.01	0.57	0.42	0.94	-0.04	0.59	0.46	0.93
	O2	0.53	0.63	0.56	0.02	0.38	0.05	0.47	-0.16	0.31	0.38	0.41	-0.10
m06l	Fe1	3.06	3.25	2.94	3.73	3.08	3.30	2.19	3.95	3.17	3.33	1.89	3.89
	Fe2	-3.21	4.02	3.58	4.19	-3.91	4.05	3.90	3.87	-3.91	4.08	3.94	3.90
	C	-0.01	0.01	0.01	0.00	0.50	0.51	0.35	0.54	0.70	0.75	0.75	0.72
	O1	-0.22	0.85	0.33	-0.36	-0.20	0.57	0.37	0.94	-0.22	0.58	0.43	0.93
	O2	0.36	0.50	0.42	0.02	0.16	0.05	0.39	-0.16	0.12	0.19	0.36	-0.10
b3lyp	Fe1	3.09	3.19	3.00	3.73	3.19	3.28	1.74	3.95	3.25	3.33	3.32	3.89
	Fe2	-3.17	4.09	3.56	4.19	-3.97	4.07	3.96	3.87	-3.96	4.10	4.02	3.90
	C	-0.01	0.01	0.01	0.00	0.49	0.51	0.50	0.54	0.68	0.73	-0.67	0.72
	O1	-0.31	0.97	0.29	-0.36	-0.26	0.57	0.50	0.94	-0.26	0.59	0.55	0.93
	O2	0.38	0.54	0.44	0.02	0.15	0.05	0.38	-0.16	0.11	0.19	0.18	-0.10
opbe	Fe1	2.77	3.19	2.74	3.73	2.70	3.12	2.14	3.95	2.82	3.16	1.92	3.89
	Fe2	-2.98	3.81	3.42	4.19	-3.70	3.95	3.77	3.87	-3.73	3.97	3.81	3.90
	C	-0.01	0.01	0.01	0.00	0.45	0.46	0.34	0.54	0.68	0.74	0.74	0.72
	O1	-0.27	0.71	0.42	-0.36	-0.10	0.58	0.41	0.94	-0.15	0.60	0.44	0.93
	O2	0.50	0.61	0.54	0.02	0.32	0.04	0.02	-0.16	0.26	0.33	0.39	-0.10

Table 5.7: CM5 partial charges of **2i**, **2TS** and **2f** calculated by different functionals and RASSCF/RASPT2. Spin states $S = 5$, 4 and broken symmetry 0 are presented for the functionals, and $S = 4$ for **2i** and $S = 5$ for **2TS** and **2f** for the MR calculation. The values of the two Fe atoms, the bridging (O1) and the terminal (O2) and the C of methane are presented.

		2i				2TS				2f			
		BS	$S = 10/2$	$S = 8/2$	RASSCF $S = 8/2$ (16,16)	BS	$S = 10/2$	$S = 8/2$	RASSCF $S = 10/2$ (16,16)	BS	$S = 10/2$	$S = 8/2$	RASSCF $S = 10/2$ (16,16)
pbe	Fe1	0.69	0.67	0.69	1.15	0.76	0.76	0.75	1.20	0.73	0.73	0.68	1.19
	Fe2	0.62	0.62	0.64	1.25	0.56	0.63	0.59	0.77	0.54	0.62	0.57	0.79
	C	-0.34	-0.34	-0.34	-0.31	-0.26	-0.25	-0.30	-0.17	-0.23	-0.24	-0.24	-0.22
	O1	-0.22	-0.25	-0.24	-0.42	-0.30	-0.33	-0.32	-0.45	-0.30	-0.32	-0.31	-0.45
	O2	-0.37	-0.39	-0.37	-0.42	-0.42	-0.55	-0.40	-0.47	-0.44	-0.45	-0.43	-0.43
m06l	Fe1	0.79	0.78	0.79	1.15	0.87	0.86	0.84	1.20	0.84	0.84	0.77	1.19
	Fe2	0.74	0.74	0.75	1.25	0.70	0.74	0.70	0.77	0.69	0.73	0.68	0.79
	C	-0.32	-0.32	-0.32	-0.31	-0.21	-0.21	-0.28	-0.17	-0.21	-0.22	-0.22	-0.22
	O1	-0.25	-0.24	-0.28	-0.42	-0.38	-0.38	-0.36	-0.45	-0.37	-0.37	-0.35	-0.45
	O2	-0.42	-0.39	-0.40	-0.42	-0.48	-0.57	-0.43	-0.47	-0.48	-0.48	-0.47	-0.43
b3lyp	Fe1	0.77	0.77	0.78	1.15	0.86	0.85	0.78	1.20	0.83	0.83	0.83	1.19
	Fe2	0.74	0.74	0.75	1.25	0.71	0.73	0.69	0.77	0.70	0.72	0.71	0.79
	C	-0.34	-0.33	-0.34	-0.31	-0.22	-0.22	-0.22	-0.17	-0.22	-0.24	-0.21	-0.22
	O1	-0.24	-0.20	-0.26	-0.42	-0.38	-0.38	-0.35	-0.45	-0.37	-0.37	-0.37	-0.45
	O2	-0.41	-0.37	-0.39	-0.42	-0.47	-0.57	-0.47	-0.47	-0.48	-0.48	-0.48	-0.43
opbe	Fe1	0.71	0.69	0.72	1.15	0.79	0.78	0.77	1.20	0.76	0.76	0.70	1.19
	Fe2	0.66	0.66	0.68	1.25	0.63	0.68	0.64	0.77	0.61	0.67	0.62	0.79
	C	-0.36	-0.36	-0.36	-0.31	-0.25	-0.26	-0.31	-0.17	-0.23	-0.25	-0.25	-0.22
	O1	-0.23	-0.26	-0.25	-0.42	-0.34	-0.35	-0.33	-0.45	-0.33	-0.33	-0.32	-0.45
	O2	-0.39	-0.39	-0.37	-0.42	-0.44	-0.56	-0.55	-0.47	-0.45	-0.46	-0.44	-0.43

so if someone wants to count them and think about formal oxidation states, then we know that in total the Fe(II) has 5.5 3d electrons, out of which 2 is paired, and Fe(V) has 3.5 electrons, none paired. This way the oxidation states are 2.5 and 4.5.

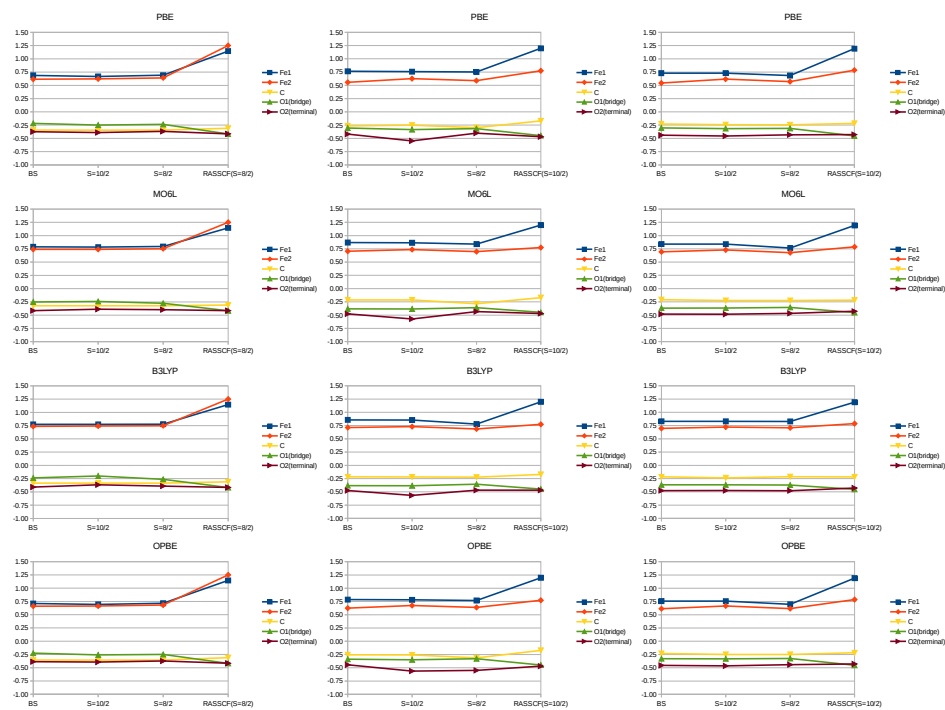


Figure 5.17: CM5 partial charges of **2i**, **2TS** and **2f** calculated by different functionals and RASSCF/RASPT2. Spin states $S = 5$, 4 and broken symmetry 0 are presented for the functionals, and $S = 4$ for **2i** and $S = 5$ for **2TS** and **2f** for the MR calculation. The values of the two Fe atoms, the bridging (O1) and the terminal (O2) and the C of methane are presented.

CASSCF predicts no unpaired electrons on C initially as expected, and along the reaction it increases with the formation of methyl radical. The bridging O has some spin density on it which suddenly increases in the transition state. It might be that the Fe(V) is claiming its electron leaving one unpaired. This also explains that the total number of unpaired electrons on the two Fe is almost 8. In this case if we want to think schematically, then there are 10 electrons on the 3d orbitals of the 2 Fe atoms. Fe(V) has 4, which means it is actually Fe(IV), while Fe(II) has 6, two of which is paired. This gives 4 unpaired electrons on both Fe centres, and one unpaired electron on the bridging O.

There is no spin density on the terminal O in neither part of the reaction. This is an intriguing observation, because in mononuclear Fe-oxo clusters it was demonstrated that the Fe(IV)=O²⁻ cluster can be described as an Fe(III)-O^{*-} moiety, where the oxygen radical anion is the important component of the reaction. Although in this particular reaction it is not the terminal O that accepts the H atom, similar clusters can provide reaction paths where C-H bond activation takes place over the terminal O site as it was demonstrated in Chapter 2.

In the initial **2i** structure the high spin state of DFT is $S = 4$. This predicts, similarly to MR, that the two Fe atoms are not equal, although it puts way less spin density on them (~ 3 and ~ 3.5 vs 3.7 and 4.2). In the transition states and final state $S = 5$ becomes the high spin state. In these cases, DFT predicts a difference between the spin state of the two Fe atoms. It clearly shows, that it is not able to give the correct electronic structure. The broken symmetry $S = 0$ calculations are even worse. They also do not correspond with the spin densities and partial charges of the high spin states.

The spin density on C is correctly predicted by DFT: there is none in the **2i** state, and it increases with the formation of the CH_3 radical. The spin density of the bridging O however stays the same during the course of the reaction. Opposite to the MR calculations the terminal O has a considerable amount of unpaired electrons in the **2i** state (~ 0.5) which then decreases in **2TS** to almost 0, and increases again to ~ 0.25 in the final state.

The relative partial charges of the C, the bridging O and terminal O are also wrong. Initially according to the MR calculations, the two O atoms have similar partial charge, while C is more positive. During the course of the reaction the partial charge of C slightly increases, while the two O atoms become slightly more negative, and approximately the same. On the other hand DFT predicts C and the bridging O to have similar partial charge, and the terminal O to be more negative. During the reaction the partial charge of C slightly increases, while the two O atoms slightly decrease, as in the case of the CASSCF calculations, but the bridging O remains always less negative than the terminal O.

FENTON-TYPE ACTIVATION

Tables 5.8 and 5.9 and Figures 5.18 and 5.19 show the CM5 partial charges and Hirshfeld spin densities of $S = 0, 4$ and 5 spin states of the intermediates of the Fenton-type activation.

CASSCF predicts 10 singly occupied orbitals in the minimal active space of **3i**. This is very similar to **1i**. Also the spin densities on the Fe atoms and the ligand O and C atoms are very similar. DFT $S = 5$ and $S = 0$ broken symmetry calculations can predict equally well the situation as in the case of the heterolytic dissociation.

The electronic configurations of **3TS** and **3f** intermediates are more similar to that of the **2TS** and **2f** cases, because both have non-integer occupation orbitals, and 10 singly occupied orbitals. This is again something that cannot be described by single reference methods. According to the RASSCF calculations the two Fe atoms have ~ 3.8

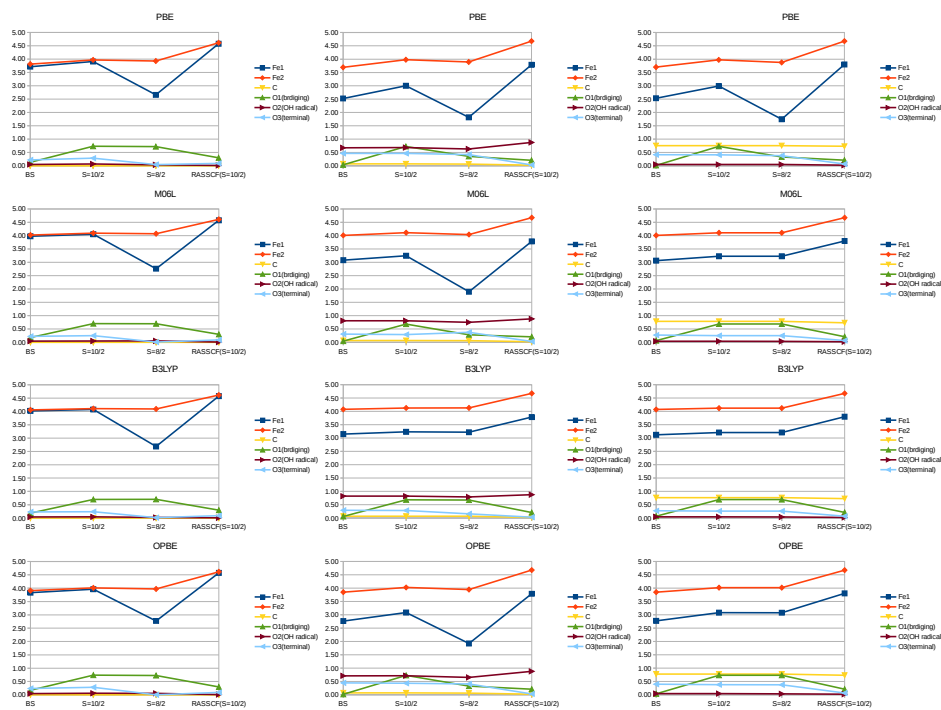


Figure 5.18: Absolute values of Hirshfeld spin densities of **3i**, **3TS** and **3f** calculated by different functionals and RASSCF/RASPT2. Spin states $S = 5$, 4 and broken symmetry 0 are presented for the functionals, and $S = 5$ for the MR calculation. The values of the two Fe atoms, the OH radical (O2), the terminal O (O3), the latter two are peroxo in **3i**, and the C of methane are presented.

and ~ 4.7 unpaired electrons implying a near perfect Fe(IV) and Fe(III) oxidation state. The 10th electron is located on the OH radical in the TS, and on the CH_3 radical in the final state. And there is a small spin density on the bridging O as well. This is not the case for DFT. It delocalizes the unpaired electrons way too much. There are 3 and 4 unpaired electrons on each Fe atoms, and there is considerable amount on the bridging O (~ 0.7 vs 0.2 calculated by RASSCF) and on the terminal O (~ 0.4 vs ~ 0 calculated by RASSCF). With this DFT creates non-existent O radical anions.

5.3.5. COMPARISON OF ΔE_R , ΔE^A AND THE SPIN LADDER OBTAINED BY DFT AND CASSCF/CASPT2 METHODS

We now discuss how well the energetics can be predicted by different DFT methods. For this we compare the results obtained using a number of popular DFT functionals for the elementary reactions discussed above with the values computed at the multireference CASPT2 or RASPT2 level. Singlet electronic structure solutions were computed at the DFT level using the broken-symmetry approach.

Table 5.8: Hirshfel spin densities of **3i**, **3TS** and **3f** calculated by different functionals and RASSCF/RASPT2. Spin states $S = 5, 4$ and broken symmetry 0 are presented for the functionals, and $S = 5$ for the MR calculation. The values of the two Fe atoms, the bridging O (O1) the OH radical (O2), the terminal O (O3), the latter two are peroxis in **3i**, and the C of methane are presented.

		3i				3TS				3f			
		BS	S = 10/2	S = 8/2	RASSCF S = 10/2 (16,16)	BS	S = 10/2	S = 8/2	RASSCF S = 10/2 (16,16)	BS	S = 10/2	S = 8/2	RASSCF S = 10/2 (16,16)
pbe	Fe1	2.60	3.14	2.67	3.73	2.35	3.04	2.06	3.95	2.50	3.07	1.84	3.89
	Fe2	-2.80	3.74	3.33	4.19	-3.39	3.90	3.70	3.87	-3.55	3.92	3.76	3.90
	C	-0.01	0.02	0.02	0.00	0.39	0.45	0.34	0.54	0.66	0.72	0.72	0.72
	O1	-0.26	0.69	0.45	-0.36	0.01	0.57	0.42	0.94	-0.04	0.59	0.46	0.93
	O2	0.53	0.63	0.56	0.02	0.38	0.05	0.47	-0.16	0.31	0.38	0.41	-0.10
m06l	Fe1	3.06	3.25	2.94	3.73	3.08	3.30	2.19	3.95	3.17	3.33	1.89	3.89
	Fe2	-3.21	4.02	3.58	4.19	-3.91	4.05	3.90	3.87	-3.91	4.08	3.94	3.90
	C	-0.01	0.01	0.01	0.00	0.50	0.51	0.35	0.54	0.70	0.75	0.75	0.72
	O1	-0.22	0.85	0.33	-0.36	-0.20	0.57	0.37	0.94	-0.22	0.58	0.43	0.93
	O2	0.36	0.50	0.42	0.02	0.16	0.05	0.39	-0.16	0.12	0.19	0.36	-0.10
b3lyp	Fe1	3.09	3.19	3.00	3.73	3.19	3.28	1.74	3.95	3.25	3.33	3.32	3.89
	Fe2	-3.17	4.09	3.56	4.19	-3.97	4.07	3.96	3.87	-3.96	4.10	4.02	3.90
	C	-0.01	0.01	0.01	0.00	0.49	0.51	0.50	0.54	0.68	0.73	-0.67	0.72
	O1	-0.31	0.97	0.29	-0.36	-0.26	0.57	0.50	0.94	-0.26	0.59	0.55	0.93
	O2	0.38	0.54	0.44	0.02	0.15	0.05	0.38	-0.16	0.11	0.19	0.18	-0.10
opbe	Fe1	2.77	3.19	2.74	3.73	2.70	3.12	2.14	3.95	2.82	3.16	1.92	3.89
	Fe2	-2.98	3.81	3.42	4.19	-3.70	3.95	3.77	3.87	-3.73	3.97	3.81	3.90
	C	-0.01	0.01	0.01	0.00	0.45	0.46	0.34	0.54	0.68	0.74	0.74	0.72
	O1	-0.27	0.71	0.42	-0.36	-0.10	0.58	0.41	0.94	-0.15	0.60	0.44	0.93
	O2	0.50	0.61	0.54	0.02	0.32	0.04	0.02	-0.16	0.26	0.33	0.39	-0.10

Table 5.9: CM5 partial charges of **3i**, **3TS** and **3f** calculated by different functionals and RASSCF/RASPT2. Spin states $S = 5, 4$ and broken symmetry 0 are presented for the functionals, and $S = 5$ for the MR calculation. The values of the two Fe atoms, the bridging O (O1) the OH radical (O2), the terminal O (O3), the latter two are peroxis in **3i**, and the C of methane are presented.

		3i				3TS				3f			
		BS	S = 10/2	S = 8/2	RASSCF S = 10/2 (16,16)	BS	S = 10/2	S = 8/2	RASSCF S = 10/2 (16,16)	BS	S = 10/2	S = 8/2	RASSCF S = 10/2 (16,16)
pbe	Fe1	0.71	0.72	0.63	1.13	0.86	0.87	0.84	1.12	0.78	0.79	0.75	1.12
	Fe2	0.47	0.49	0.48	1.13	0.48	0.54	0.51	1.18	0.48	0.53	0.50	1.18
	C	-0.35	-0.35	-0.35	-0.30	-0.34	-0.34	-0.34	-0.30	-0.23	-0.23	-0.23	-0.20
	O1	-0.30	-0.32	-0.32	-0.73	-0.31	-0.35	-0.31	-0.79	-0.31	-0.35	-0.32	-0.79
	O2	-0.29	-0.30	-0.28	-0.34	-0.37	-0.37	-0.39	-0.28	-0.58	-0.58	-0.58	-0.61
m06l	Fe1	-0.30	-0.31	-0.27	-0.44	-0.42	-0.43	-0.40	-0.46	-0.45	-0.45	-0.43	-0.45
	Fe2	0.82	0.82	0.71	1.13	0.97	0.96	0.91	1.12	0.88	0.88	0.88	1.12
	C	0.59	0.60	0.59	1.13	0.63	0.65	0.63	1.18	0.62	0.64	0.64	1.18
	O1	-0.33	-0.33	-0.33	-0.30	-0.32	-0.32	-0.32	-0.30	-0.22	-0.22	-0.22	-0.20
	O2	-0.36	-0.37	-0.37	-0.73	-0.38	-0.39	-0.36	-0.79	-0.38	-0.39	-0.39	-0.79
b3lyp	Fe1	-0.31	-0.31	-0.29	-0.34	-0.32	-0.32	-0.35	-0.28	-0.60	-0.60	-0.60	-0.61
	Fe2	-0.34	-0.34	-0.29	-0.44	-0.47	-0.47	-0.45	-0.46	-0.48	-0.48	-0.48	-0.45
	C	0.82	0.82	0.71	1.13	0.96	0.96	0.96	1.12	0.88	0.88	0.88	1.12
	O1	0.59	0.59	0.59	1.13	0.64	0.64	0.64	1.18	0.63	0.63	0.63	1.18
	O2	-0.34	-0.34	-0.34	-0.30	-0.32	-0.33	-0.33	-0.30	-0.23	-0.23	-0.23	-0.20
opbe	Fe1	-0.36	-0.36	-0.36	-0.73	-0.39	-0.39	-0.39	-0.79	-0.39	-0.39	-0.39	-0.79
	Fe2	-0.31	-0.31	-0.30	-0.34	-0.31	-0.31	-0.32	-0.28	-0.59	-0.59	-0.59	-0.61
	C	-0.34	-0.34	-0.30	-0.44	-0.47	-0.47	-0.46	-0.46	-0.48	-0.48	-0.48	-0.45
	O1	0.76	0.76	0.65	1.13	0.89	0.89	0.86	1.12	0.81	0.81	0.81	1.12
	O2	0.53	0.54	0.53	1.13	0.55	0.59	0.57	1.18	0.54	0.58	0.58	1.18

As discussed earlier the spin ladder calculated by the MR method for all intermediates is similar: the ground state is the $S = 0$ spin state, and the energy gradually increases with the spin state. Figure 5.20, 5.21 and 5.22 shows the spin ladders and the reaction

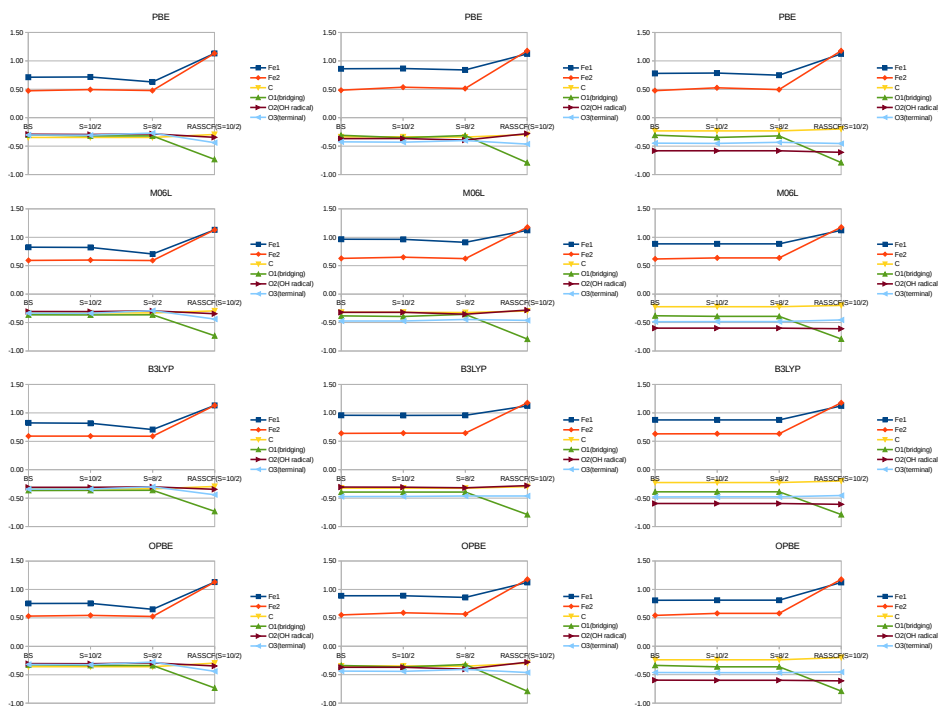


Figure 5.19: CM5 partial charges of **3i**, **3TS** and **3f** calculated by different functionals and RASSCF/RASPT2. Spin states $S = 5, 4$ and broken symmetry 0 are presented for the functionals, and $S = 5$ for the MR calculation. The values of the two Fe atoms, the bridging O (O1) the OH radical (O2), the terminal O (O3), the latter two are perox in **3i**, and the C of methane are presented.

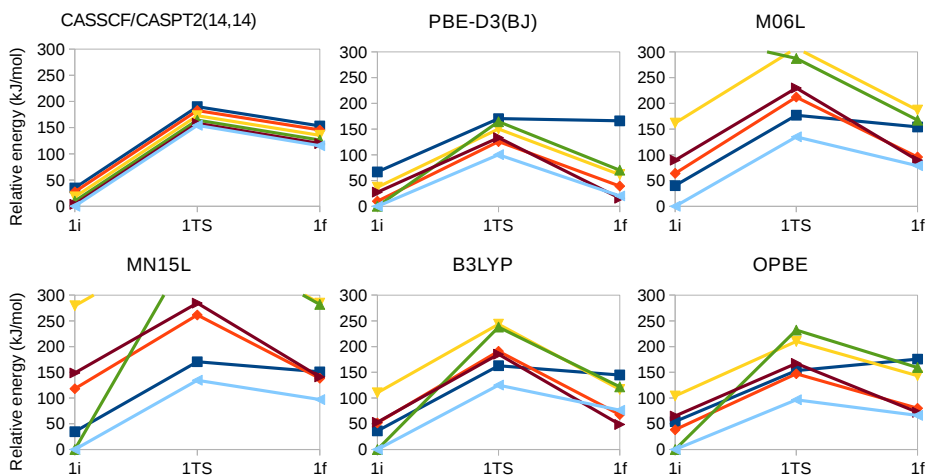


Figure 5.20: Reaction energy diagram of the C-H bond heterolytic dissociation of methane calculated by CASSCF(14,14)/CASPT2 method and different DFT functionals for all possible spin states. Colours: $S = 0$ (BS for DFT): light blue, $S = 1$: yellow, $S = 2$: brown, $S = 3$: green, $S = 4$: orange, $S = 5$: dark blue

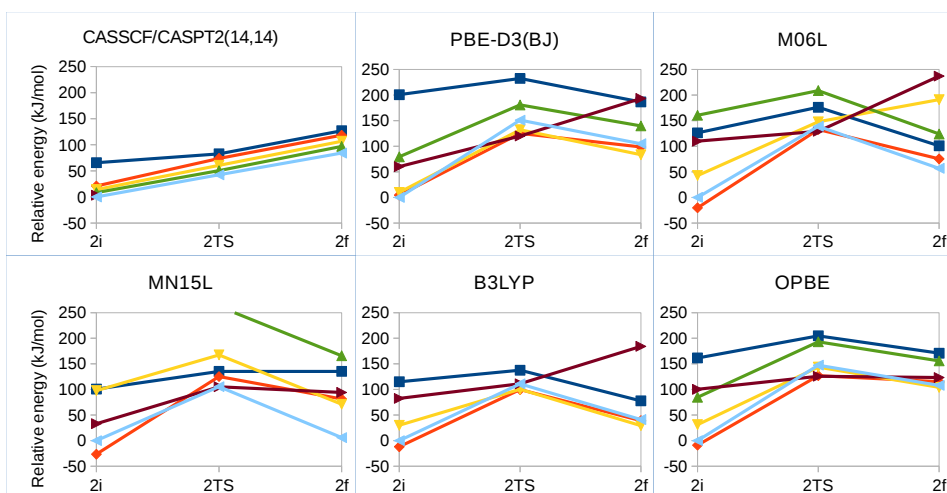


Figure 5.21: Reaction energy diagram of the homolytic dissociation of methane calculated by CASSCF(14,14)/CASPT2 method and different density functionals for all possible spin states. Colours: S = 0 (BS for DFT): light blue, S = 1: yellow, S = 2 brown, S = 3: green, S = 4: orange, S = 5: dark blue

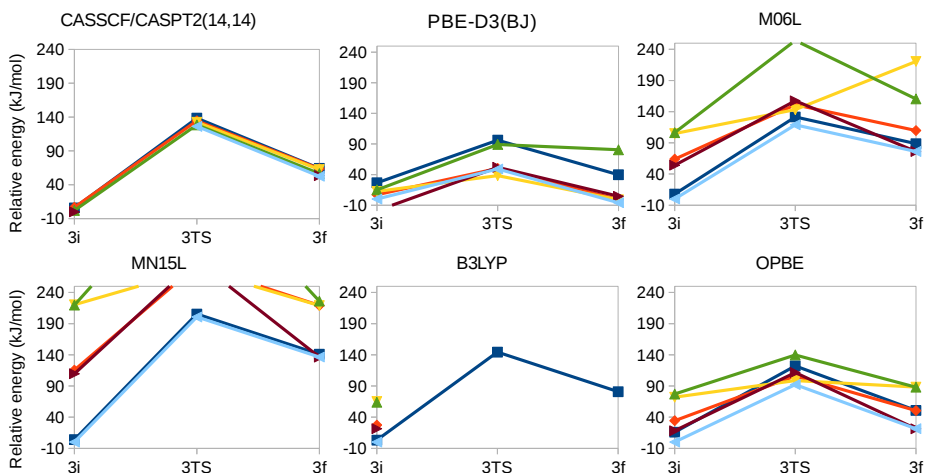


Figure 5.22: Reaction energy diagram of the Fenton-type dissociation of methane calculated by different DFT functionals in all possible spin states Colours: S=0, (BS for DFT): light blue, S = 1: yellow, S = 2 brown, S = 3: green, S = 4: orange, S = 5: dark blue

energy diagram calculated by the different DFT functionals obtained for all three reactions. From the DFT spin ladder it is not possible to identify a trend like the one obtained from MR calculations. And on top of that the order of the stability of the different spin states is also dependent on the functional. Our previous analysis of the electronic structure however shows that the intermediate spin states completely fail to describe the electronic structure, therefore they are going to be disregarded in the following analysis, and we will focus on the high spin and the broken symmetry cases.

HETEROLYTIC DISSOCIATION

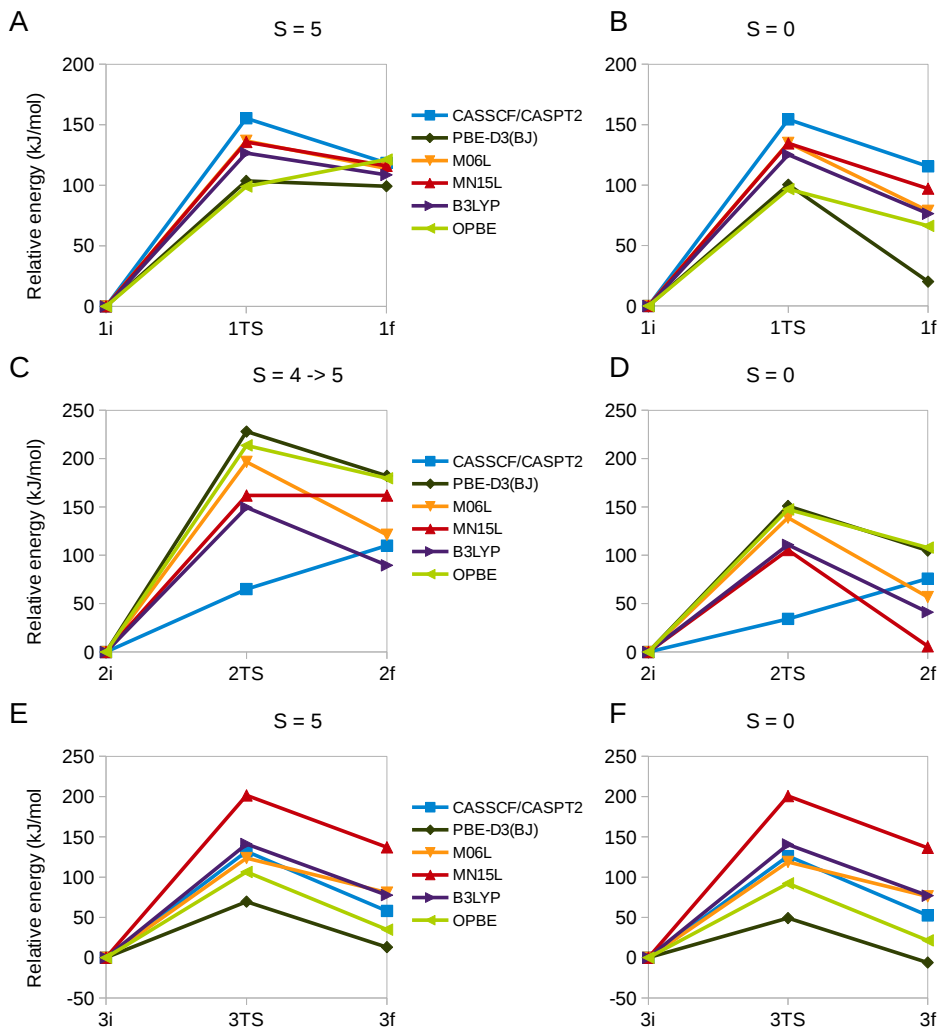


Figure 5.23: Reaction energy diagram of the A, B: heterolytic; C, D: homolytic and E, F: Fenton-type dissociation calculated with different DFT functionals and CASSCF/CASPT2 method.

The reaction energy diagrams obtained with MR and DFT for the $S = 5$ high spin and $S = 0$ broken symmetry cases are presented in Figure 5.23 A and B respectively. The reaction and transition state energies calculated on the $S = 5$ potential energy surface are closer to the CASSCF/CASPT2 calculations. The reason for that might be that the $S = 5$ state describes the electronic structure better, as the broken symmetry density function does not put any spin density on the bridging O atom. The best performing

functionals are M06L and MN15L with a deviation from the CASSCF/CASPT2 results of -19 and -20 and -4 and -2 kJ/mol from the ΔE^a and ΔE_R respectively. While the reaction energy is rather well estimated by all investigated functionals ($\Delta\Delta E_{R,\max} = -19$ kJ/mol for PBE), the transition state energy has a higher deviation from the multireference result. All the investigated functionals underestimate the activation barrier compared to CASPT2, and PBE and OPBE predict the lowest barrier with a deviation from the MR results of $\Delta\Delta E^a = -52$ and -56 kJ/mol respectively.

HOMOLYTIC DISSOCIATION

The reaction energy diagram of the high spin potential energy surface and the broken symmetry $S = 0$ surface calculated by MR and DFT are presented in Figure 5.23 C and D. The spin state of the high spin PES changes during the reaction, as it is explained in detail in the previous sections, we move from $S = 4$ high spin state of **2i** to $S = 5$ of **2TS** and **2f**. We can see, that the CASSCF/CASPT2 calculations do not predict **2TS** to be a transition state. The most likely explanation for this is that single point calculations were performed, and either the transition state or the final state geometry is far from the local minimum on the potential energy surface.

On the contrary all DFT functionals calculate **2TS** to be more unstable than **2f**, all following the same trend, probably as the result of the similar density functions. The reaction energies on the high spin energy surface are best predicted by B3LYP and M06L functionals ($\Delta\Delta E_R = -20$ and $+11$ kJ/mol respectively), however the rest is off by more than 50 kJ/mol. Interestingly PBE and OPBE predict higher activation barriers than the other functionals in contrary to the previous case.

FENTON-TYPE DISSOCIATION

The reaction energy diagrams of the Fenton-type methane activation at the high spin $S = 5$ and broken symmetry $S = 0$ potential energy surfaces obtained by MR and DFT methods are presented in Figure 5.23 E and F. As it is explained earlier the direct comparison of energies in this case should be treated with doubts, because the energy as the function of active space is not converged. From Figure 5.23 it can be seen that the trends of $S = 0$ and $S = 5$ are similar, and the functionals predict a wide range of reaction barriers and energies. Here again PBE and OPBE predict the lowest energies compared with the other functionals, and M06L and B3LYP are the closest to the MR results with only a few kJ/mol energy difference.

5.4. DISCUSSION

WE investigated three fundamentally different reactions over Fe(III) and Fe(IV) clusters. The electronic structure of the Fe(III) cluster **1i** was described with integer occupation numbered (0, 1 and 2) orbitals by CASSCF. The high spin electronic structure calculated was found to have one dominant configuration, and be similar to the electronic configuration obtained by DFT of 10 singly occupied orbitals. The broken symmetry description came also close, but that one could not predict the spin density on the bridging O atom. On the other hand, the intermediate spin states failed to describe the correct electronic structure.

During the heterolytic dissociation reaction there is no formal oxidation state change, the Fe atoms remain in +3 oxidation state throughout the course of the reaction. The transition state (**1TS**) and the final state (**1f**) of the reaction could be described with similar orbitals as **1i** by both CASSCF and DFT methods in the high spin state.

5

The reaction barriers and energies calculated by DFT are rather close to the reference MR case in the high spin $S = 5$ potential energy surface. $S = 0$ broken symmetry calculation approximate the trends well as well, however the not as well as $S = 5$. This is expected, because the electronic structure is better described in the high spin than in the broken symmetry case. We also know that the spin ladder predicted by the MR method is very similar for all three intermediates with identical energy differences between the ground state and high spin state. This means that the relative energies between the intermediates are going to be the same on both the $S = 0$ PES and the $S = 5$ PES. This means that reaction energy calculations can be performed on the high spin potential energy surface. This is beneficial for us, because the broken symmetry calculations are more expensive and often cumbersome.

These findings show that similar cases, binuclear Fe(III) clusters participating in reactions with no oxidation state change, can be safely modelled with DFT, because the electronic structure can be described with single reference wave function. The results also indicate that either the high spin or the broken symmetry low spin potential energy surface can be used to model the reaction. In case a bridging O is present in the complex, the high spin state gives a better prediction of the energy barriers than the broken symmetry low spin even though the low spin is the ground state.

These calculations also indicate that even though the intermediate spin states can sometimes be more stable than the high spin, for example B3LYP predicts $S = 3$ state to be the energetically most favourable, for the correct trend the high spin state should be used in the calculations, because the intermediate spin states cannot describe the electronic structure correctly. Unless, of course, the local spin of the Fe atoms changes

from high to low spin for some reason (e.g. substitution of O ligands with N). In this case additional investigation is needed.

The second reaction, the homolytic dissociation of methane, is catalysed by an Fe(IV)Fe(IV) cluster which according to spin density and partial charge analysis turns out to be rather an Fe(III)Fe(V) cluster (**2i**) which undergoes reduction by the methane to form an Fe(III)Fe(IV) or rather an Fe(II)O(I)Fe(IV) complex and methyl radical (**2f**). During the reaction the high spin changes from $S = 4$ to $S = 5$ before the transition state (**2TS**). All three structures have a strong multireference character, because they have orbitals with a non-integer number of electrons on them. These are the Fe($3d_{z^2}$)=O($2p_z$) and the Fe($3d_{xz}$)-O($2p_z$)-Fe($3d_{xz}$) bonding-antibonding pairs with a total of 4 electrons on the 2 pairs. The orbitals of the latter pair are singly occupied in the high spin state of the transition and final state. As the p orbital of the methyl radical only participates in singly occupied orbitals we think that the multireference character is not due to the type of the reaction, but due to the nature of the Fe site.

The single-reference DFT method cannot properly describe the electronic structure of these intermediates. This means that even if the energy is correctly predicted, e.g. the reaction energy calculated by M06L is only 11 kJ/mol away from the reaction energy predicted by CASSCF/CASPT2, it is not going to be for the right reason. In this particular case while all DFT functionals predict **2TS** to have the highest energy of the three intermediates, CASPT2 predicts **2TS** to have lower energy than the product.

The Fenton-type reaction starts with an Fe(III)Fe(III) cluster that undergoes oxidation by H₂O₂ to form an Fe(IV)Fe(III) cluster, H₂O molecule and methyl radical. The high spin state of all intermediates is $S = 5$. The electronic structure of **3i** is similar to **1i**, it can be described with integer number electrons on each orbital. Both the high spin and broken symmetry $S = 0$ low spin density functions are suitable to correctly describe the electronic structure. The Fe(IV)Fe(III) cluster of **3TS** and **3i** are more similar to that of the homolytic reaction. These have a multireference character. In the minimal active space other than the 10 singly occupied orbitals there are two orbitals with non-integer number electrons on them. These are a bonding anti-bonding pair of Fe($3d_{z^2}$)=O($2p_z$) orbitals. The calculations agree with the results of the homolytic dissociation: the nature of the Fe cluster determines whether the structure has a multireference character or not, and the methyl and OH radicals can be described by singly occupied orbitals.

DFT cannot describe the electronic configuration of **3TS** and **3f** satisfactorily, though B3LYP and M06L predict similar energies as CASSCF/CASPT2 calculations.

5.5. CONCLUSIONS

IN this chapter we investigated three cases of C-H bond dissociation of methane over binuclear iron-oxo clusters with DFT and multireference CASSCF/CASPT2 and RASSCF/RASPT2 methods and compared the results. Our findings can be summarized as follows.

DFT can safely predict reaction and activation barrier trends when the orbitals of the active space have near-integer occupation numbers (0,1 or 2). In this case there is no need for multireference calculations, DFT can describe the electronic configuration. The high spin reaction surface is sufficient to describe the reaction profile. It describe better than the broken symmetry singlet even if that is the ground state. Of course, this only holds if the local spin of the Fe atoms remains high spin throughout the course of the reaction. The intermediate spin states should be disregarded even if they have lower energy. In our study M06L and MN15L functionals had the closest reaction and activation energies to the MR results, and PBE and OPBE had the most significant deviations. All functionals underestimated the activation and reaction barriers. However, this study is not sufficient to draw generalised conclusions.

In case orbitals with non-integer occupation numbers are present in the multireference active space, DFT is not able to satisfactorily describe the electronic structure and predict reaction energies and barriers. Spin contamination does not indicate whether a case is going to be multireference or not. In all investigated cases the spin contamination of $S > 2$ is negligible, and there are structures with multireference character. Whether a case is multireference or not is not influenced by the reaction mechanism: the radicals can be well described with singly occupied orbitals, thus both heterolytic and homolytic dissociation can be multireference case or not. The nature of the Fe site determines whether a structure is multireference or not.

The Fe(IV)=O moiety is often considered the active species in the methane activation reaction. Several DFT studies consider the spin density of the O the determining factor of the activity of the moiety. However, from this study it seems that DFT is not able to predict the spin density of this O on binuclear Fe sites. In fact, MR calculations predict a spin density of near 0 on this O. This indicates that the speculations about the importance of the spin density of the O, and the oversimplified picture of C-H bond dissociation based on molecular orbital theory is not correct.

REFERENCES

- [1] R. Banerjee, Y. Proshlyakov, J. D. Lipscomb and D. A. Proshlyakov, *Nature*, 2015, **518**, 431–434.
- [2] G. I. Panov, V. I. Sobolev, K. A. Dubkov, V. N. Parmon, N. S. Ovanesyan, A. E. Shilov and A. A. Shteinman, *React. Kinet. Catal. Lett.*, 1997, **61**, 251–258.
- [3] M. V. Parfenov, E. V. Starokon, L. V. Pirutko and G. I. Panov, *J. Catal.*, 2014, **318**, 14–21.
- [4] V. I. Sobolev, K. A. Dubkov, O. V. Panna and G. I. Panov, *Catal. Today*, 1995, **24**, 251–252.
- [5] C. Hammond, N. Dimitratos, J. A. Lopez-Sanchez, R. L. Jenkins, G. Whiting, S. A. Kondrat, M. H. Ab Rahim, M. M. Forde, A. Thetford, H. Hagen, E. E. Stangland, J. M. Moulijn, S. H. Taylor, D. J. Willock and G. J. Hutchings, *ACS Catal.*, 2013, **3**, 1835–1844.
- [6] F. Neese, D. G. Liakos and S. Ye, *J. Biol. Inorg. Chem.*, 2011, **16**, 821–829.
- [7] K. Pierloot and S. Vancoillie, *J. Chem. Phys.*, 2006, **125**, year.
- [8] M. Radón, E. Broclawik and K. Pierloot, *J. Phys. Chem. B*, 2010, **114**, 1518–1528.
- [9] M. G. Delcey, K. Pierloot, Q. M. Phung, S. Vancoillie, R. Lindh and U. Ryde, *Phys. Chem. Chem. Phys.*, 2014, **16**, 7929–7938.
- [10] D. J. Xiao, E. D. Bloch, J. A. Mason, W. L. Queen, M. R. Hudson, N. Planas, J. Borycz, A. L. Dzubak, P. Verma, K. Lee, F. Bonino, V. Crocellà, J. Yano, S. Bordiga, D. G. Truhlar, L. Gagliardi, C. M. Brown and J. R. Long, *Nature Chem.*, 2014, **6**, 590–595.
- [11] P. Verma, K. D. Vogiatzis, N. Planas, J. Borycz, D. J. Xiao, J. R. Long, L. Gagliardi and D. G. Truhlar, *J. Am. Chem. Soc.*, 2015, **137**, 5770–5781.
- [12] B. Mondal, F. Neese, E. Bill and S. Ye, *J. Am. Chem. Soc.*, 2018, **140**, 9531–9544.
- [13] C. Kupper, B. Mondal, J. Serrano-Plana, I. Klawitter, F. Neese, M. Costas, S. Ye and F. Meyer, *J. Am. Chem. Soc.*, 2017, **139**, 8939–8949.
- [14] S. Ye, C. Kupper, S. Meyer, E. Andris, R. Navrátil, O. Krahe, B. Mondal, M. Atanasov, E. Bill, J. Roithová, F. Meyer and F. Neese, *J. Am. Chem. Soc.*, 2016, **138**, 14312–14325.
- [15] J. F. Berry, S. DeBeer George and F. Neese, *Phys. Chem. Chem. Phys.*, 2008, **10**, 4361–4374.
- [16] H. Chen, W. Lai and S. Shaik, *J. Phys. Chem. B*, 2011, **115**, 1727–1742.
- [17] T. A. Rokob, J. Chalupský, D. Bím, P. C. Andrikopoulos, M. Srncic and L. Rulíšek, *J. Biol. Inorg. Chem.*, 2016, **21**, 619–644.
- [18] R. K. Carlson, S. O. Odoh, S. J. Tereniak, C. C. Lu and L. Gagliardi, *J. Chem. Theory Comput.*, 2015, **11**, 4093–4101.
- [19] T. V. Harris, Y. Kurashige, T. Yanai and K. Morokuma, *J. Chem. Phys.*, 2014, **140**, year.
- [20] J. Chalupský, T. A. Rokob, Y. Kurashige, T. Yanai, E. I. Solomon, L. Rulíšek and M. Srncic, *J. Am. Chem. Soc.*, 2014, **136**, 15977–15991.

- [21] T. Ikuno, J. Zheng, A. Vjunov, M. Sanchez-Sanchez, M. A. Ortuño, D. R. Pahls, J. L. Fulton, D. M. Camaioni, Z. Li, D. Ray, B. L. Mehdi, N. D. Browning, O. K. Farha, J. T. Hupp, C. J. Cramer, L. Gagliardi and J. A. Lercher, *J. Am. Chem. Soc.*, 2017, **139**, 10294–10301.
- [22] S. Grundner, M. A. C. Markovits, G. Li, M. Tromp, E. A. Pidko, E. J. M. Hensen, A. Jentys, M. Sanchez-Sanchez and J. A. Lercher, *Nat. Commun.*, 2015, **6**, 7546.
- [23] C. Hammond, M. M. Forde, M. H. Ab Rahim, A. Thetford, Q. He, R. L. Jenkins, N. Dimitratos, J. A. Lopez-Sanchez, N. F. Dummer, D. M. Murphy, A. F. Carley, S. H. Taylor, D. J. Willock, E. E. Stangland, J. Kang, H. Hagen, C. J. Kiely and G. J. Hutchings, *Angew. Chem. Int. Ed.*, 2012, **51**, 5129–5133.
- [24] C. Hammond, R. L. Jenkins, N. Dimitratos, J. A. Lopez-Sanchez, M. H. Ab Rahim, M. M. Forde, A. Thetford, D. M. Murphy, H. Hagen, E. E. Stangland, J. M. Moulijn, S. H. Taylor, D. J. Willock and G. J. Hutchings, *Chem. Eur. J.*, 2012, **18**, 15735–15745.
- [25] S. Svelle, C. Tuma, X. Rozanska, T. Kerber and J. Sauer, *J. Am. Chem. Soc.*, 2009, **131**, 816–825.
- [26] J. T. Fermann, T. Moniz, O. Kiowski, T. J. McIntire, S. M. Auerbach, T. Vreven and M. J. Frisch, *J. Chem. Theory Comput.*, 2005, **1**, 1232–1239.
- [27] M. J. Frisch, G. W. Trucks, H. B. Schlegel, G. E. Scuseria, M. A. Robb, J. R. Cheeseman, G. Scalmani, V. Barone, G. A. Petersson, H. Nakatsuji, X. Li, M. Caricato, A. V. Marenich, J. Bloino, B. G. Janesko, R. Gomperts, B. Mennucci, H. P. Hratchian, J. V. Ortiz, A. F. Izmaylov, J. L. Sonnenberg, D. Williams-Young, F. Ding, F. Lipparini, F. Egidi, J. Goings, B. Peng, A. Petrone, T. Henderson, D. Ranasinghe, V. G. Zakrzewski, J. Gao, N. Rega, G. Zheng, W. Liang, M. Hada, M. Ehara, K. Toyota, R. Fukuda, J. Hasegawa, M. Ishida, T. Nakajima, Y. Honda, O. Kitao, H. Nakai, T. Vreven, K. Throssell, J. A. Montgomery, Jr., J. E. Peralta, F. Ogliaro, M. J. Bearpark, J. J. Heyd, E. N. Brothers, K. N. Kudin, V. N. Staroverov, T. A. Keith, R. Kobayashi, J. Normand, K. Raghavachari, A. P. Rendell, J. C. Burant, S. S. Iyengar, J. Tomasi, M. Cossi, J. M. Millam, M. Klene, C. Adamo, R. Cammi, J. W. Ochterski, R. L. Martin, K. Morokuma, O. Farkas, J. B. Foresman and D. J. Fox, *Gaussian-09*, 2016, Gaussian Inc. Wallingford CT.
- [28] J. P. Perdew, K. Burke and M. Ernzerhof, *Phys. Rev. Lett.*, 1996, **77**, 3865–3868.
- [29] J. P. Perdew, K. Burke and M. Ernzerhof, *Phys. Rev. Lett.*, 1997, **78**, 1396.
- [30] F. Weigend and R. Ahlrichs, *Phys. Chem. Chem. Phys.*, 2005, **7**, 3297–3305.
- [31] F. Weigend, *Phys. Chem. Chem. Phys.*, 2006, **8**, 1057–1065.
- [32] S. Grimme, J. Antony, S. Ehrlich and H. Krieg, *J. Chem. Phys.*, 2010, **132**, 154104.
- [33] A. J. Cohen and N. C. Handy, *Mol. Phys.*, 2001, **99**, 607–615.
- [34] Y. Zhao and D. G. Truhlar, *Theor. Chem. Acc.*, 2008, **119**, 525.
- [35] H. S. Yu, X. He and D. G. Truhlar, *J. Chem. Theory Comput.*, 2016, **12**, 1280–1293.
- [36] P. J. Stephens, F. J. Devlin, C. F. Chabalowski and M. J. Frisch, *J. Phys. Chem.*, 1994, **98**, 11623–11627.
- [37] A. V. Marenich, S. V. Jerome, C. J. Cramer and D. G. Truhlar, *J. Chem. Theory Comput.*, 2012, **8**, 527–541.
- [38] F. L. Hirshfeld, *Theor. Chim. Acta*, 1977, **44**, 129–138.

- [39] V. Veryazov, P. Widmark, L. Serrano-ANDRÉS, R. Lindh and B. O. Roos, *Int. J. Quantum Chem.*, 2004, **100**, 626–635.
- [40] F. Aquilante, J. Autschbach, R. K. Carlson, L. F. Chibotaru, M. G. Delcey, L. De Vico, I. Fdez. Galván, N. Ferré, L. M. Frutos, L. Gagliardi, M. Garavelli, A. Giussani, C. E. Hoyer, G. Li Manni, H. Lischka, D. Ma, P. A. Malmqvist, T. Müller, A. Nenov, M. Olivucci, T. B. Pedersen, D. Peng, F. Plasser, B. Pritchard, M. Reiher, I. Rivalta, I. Schapiro, J. Segarra-Martí, M. Stenrup, D. G. Truhlar, L. Ungur, A. Valentini, S. Vancoillie, V. Veryazov, V. P. Vysotskiy, O. Weingart, F. Zapata and R. Lindh, *J. Comput. Chem.*, 2016, **37**, 506–541.
- [41] B. O. Roos, V. Veryazov and P. Widmark, *Theor. Chem. Acc.*, 2004, **111**, 345–351.
- [42] B. O. Roos, R. Lindh, P. Malmqvist, V. Veryazov and P. Widmark, *J. Phys. Chem. A*, 2004, **108**, 2851–2858.
- [43] B. O. Roos, R. Lindh, P. Malmqvist, V. Veryazov and P. Widmark, *J. Phys. Chem. A*, 2005, **109**, 6575–6579.
- [44] B. O. Roos, R. Lindh, P. Malmqvist, V. Veryazov and P. Widmark, *Chem. Phys. Lett.*, 2005, **409**, 295–299.
- [45] T. Lu and F. Chen, *J. Comput. Chem.*, 2012, **33**, 580–592.

SUMMARY

IN this thesis we presented comprehensive studies on methane activation by binuclear Fe-oxo sites located in porous MOF and zeolite frameworks. Many of such studies have been previously performed, however the main focus was usually on the C-H bond activation of methane. Here we focused on the whole reaction mechanism including the activation of the Fe site and the overoxidation of methanol, as well as the effects of the porous framework.

In **Chapter 2** periodic DFT calculations were carried out to investigate the mechanism of methane oxidation with H_2O_2 over sites in Fe/ZSM-5 zeolite. The initial Fe site was modelled as a $[(\text{H}_2\text{O})_2\text{-Fe(III)-}(\mu\text{O})_2\text{-Fe(III)-}(\text{H}_2\text{O})_2]^{2+}$ extra-framework cluster deposited in the zeolite pore charge-compensated by two anionic lattice sites. The activation of this cluster with H_2O_2 gives rise to the formation of a variety of Fe(III)-oxo and Fe(IV)-oxo complexes potentially reactive towards methane dissociation. These sites are all able to promote the first C-H bond cleavage in methane by following three possible reaction mechanisms, namely, the (a) heterolytic and (b) homolytic methane dissociation as well as (c) Fenton-type activation involving free OH radicals as the catalytic species. Fe(III) was established to promote the heterolytic and Fenton-type reaction, while Fe(IV) the homolytic. The calculations indicate, that the type of activating O (Fe=O, Fe- μ O-Fe or Fe-OH) is unimportant from energetic point of view for both type of activation. The C-H activation step is followed by the formation of MeOH and MeOOH and the regeneration of the active site. Methanol can be formed following all types of C-H bond activation via the recombination of the CH_3 moiety and an OH ligand reducing the active site. MeOOH can be obtained from the reaction of CH_3 radical and O_2 molecule followed by the abstraction of a H atom from the active site. The Fenton-type path is found to proceed with the lowest activation barrier. Although the barriers for the alternative heterolytic and homolytic pathways are found to be somewhat higher, they are still quite favourable and expected to be feasible under reaction conditions, resulting ultimately in MeOH and MeOOH products. H_2O_2 oxidant competes with CH_4 substrate for the same sites. Since the oxidation of H_2O_2 to O_2 and two $[\text{H}^+]$ is energetically more favourable than the C-H oxo-functionalization, the overall efficiency of the latter target process remains low. This study demonstrates that the system cannot be reduced to a single-site single-cycle concept. Even with the simplification to a single-type of Fe cluster at a given position of the zeolite framework the formation of multiple types of active sites are possible catalysing three

mechanistically different C-H bond activations.

In **Chapter 3** we investigated methane activation over Fe containing MIL-53(Al) metal organic framework. MOFs are an alternative for zeolites with the possibility of infinite amount of structures and therefore tunability. Also they have the advantage of having the transition metals incorporated in their framework allowing for uniform clusters and therefore controllable structure and activity. In this chapter we investigated the reaction of methane with H_2O_2 over a similar binuclear Fe-oxo cluster as in Chapter 2. Additionally a monomeric Fe-oxo site was considered as it was found by thorough characterisation to be present in the material. Not only the activation of methane, but the full reaction network was considered, which includes the formation of the active site, the overoxidation of methane to CO_2 and the decomposition of H_2O_2 to H_2O and O_2 . As we focused on the consecutive reactions of methane oxidation, only the homolytic C-H bond activation of methane was investigated over the MIL-53 MOF, however as the active species are very similar, it is expected that both the heterolytic and Fenton-type activations are possible. Comparing the reaction barriers of the C-H bond activation over the binuclear Fe cluster in the zeolite presented in Chapter 2 and the Fe-MIL-53(Al) MOF, we might conclude that the MOF is more active, as the reaction barrier of this reaction step is lower. However if we look at Figure 4.4 where the activation barrier of the MOF (including activation over the bridging O, the OH and the terminal O species) is compared with activation in the zeolite, we can conclude, that there are clusters in the zeolite with similar or even higher activity as in the MOF. Calculations indicate, that the first C-H bond dissociation of methane is only one of the rate determining steps. The reaction barrier that leads to the active site formation, the O-H bond dissociation of CH_3OH and the conversion of HCOOH is in the same order of magnitude. The oxidation of H_2CO and CO has a low reaction barrier indicating that these intermediates have a low concentration in the reaction mixture in line with experiments. The pronounced selectivity of the oxidation reaction over Fe-MIL-53(Al) towards the target mono-oxygenated CH_3OH and CH_3OOH products is attributed to the limited coordination freedom of the Fe species encapsulated in the extended octahedral $[\text{AlO}_6]$ structure-forming chains, which effectively prevents the direct overoxidation paths prior to product desorption from the active sites. Importantly, our computational analysis reveals that the active sites for the desired methane oxidation are able to much more efficiently promote the direct catalytic H_2O_2 decomposition reaction, rendering thus the current combination of the active site and the reactants undesirable for the perspective methane valorization process. Also, there is no difference between the H_2O_2 decomposition pathways over zeolite and MOF, it proceeds swiftly in the case of both catalysts. The activity of mononuclear and binuclear sites were compared. The calculations indicate that despite monomeric species go through

formal oxidation state of +5 in the reaction, while dimeric species are only oxidized until formal oxidation state +4, the activity of the species are comparable, and they promote the same reaction steps.

In Chapter 2 we found that confinement of the zeolite has a significant effect on the C-H bond activation reaction step. This prompted us to further study the effects of the zeolite framework in **Chapter 4**, where we investigated the role of secondary effects such as confinement, flexibility and multifunctionality of the active site on the reactivity of well-defined Fe complexes in ZSM-5 zeolite towards methane oxofunctionalization. We used linear energy scaling relationships for the analysis. Linear energy scaling laws connect the kinetic and thermodynamic parameters of key elementary steps for heterogeneously catalysed reactions over defined active sites on open surfaces. Such scaling laws provide a framework for a rapid computational activity screening of families of new catalysts, but they also effectively impose a fundamental limit on the theoretically attainable activity. Understanding the limits of applicability of the linear scaling laws is therefore crucial for the development of predictive models in catalysis. The computed C-H activation barriers over Fe-sites at different locations inside the zeolite pores generally follow the associated reaction enthalpies and the hydrogen affinities of the active site, reflecting the O-H bond strength. Nevertheless, despite the close similarity of the geometries and intrinsic reactivities of the considered active sites, substantial deviations from these linear scaling relations are apparent from the DFT calculations. We identify three major factors behind these deviations, namely, (1) confinement effects due to zeolite micropores, (2) coordinative flexibility of the active site, and (3) multifunctionality. The latter two phenomena impact the mechanism of the catalytic reaction by providing a cooperative reaction channel for the substrate activation or by enabling the stabilizing of the intra-zeolite complex along the reaction path. Direct stabilization of the transition state was observed when the interaction of a close-by OH group and the CH₃ radical was realized. This interaction lowers the energy of the transition state and breaks the scaling relations, which is proposed to be a practical strategy for catalyst design towards methane activation. These computational findings point to the need for the formulation of multidimensional property-activity relationships accounting for both the intrinsic chemistry of the reactive ensembles and secondary effects due to their environmental and dynamic characteristics.

In **Chapter 5** we carried out a detailed comparative analysis of the performance of modern quantum chemical methods for studying the C-H bond activation of methane by binuclear iron-oxo clusters deposited in Fe-ZSM-5. Three alternative reaction mechanisms, namely the homolytic and heterolytic C-H activation and the Fenton

path were included in the analysis. The energetics of the reactions and electronic structures of the involved reaction intermediates were studied by a selection of five popular density functional methods (GGA: OPBE, PBE(D3-BJ); meta-GGA: M06L, MN15L; and hybrid: B3LYP functional), which results were compared with those obtained with the multiconfigurational self-consistent field (MC SCF) method followed by second order perturbation theory (CASSCF/CASPT2). Higher active spaces were achieved by the application of restricted active space SCF followed by the PT2 method (RASSCF/RASPT2). Qualitatively similar performance is shown for all functionals. In case the intermediates can be described without multiconfigurational wave function, which means all the orbitals have integer (0, 1 or 2) occupation number, MN15L and M06L performs the best. Although all investigated functionals in such cases reproduce the energy trends derived using the higher-level wavefunction method, they somewhat underestimate the reaction barrier and energy. The spin ladder was also investigated, and the calculations suggest, that in this case either the high spin or the broken symmetry low spin potential energy surface should be applied to describe the reaction profile. Of course, this only holds if the local spin of the Fe atoms remains high spin throughout the course of the reaction. Also, the intermediate spin states should be disregarded even if they have lower energy, because the electronic configuration is intrinsically wrong. However, if it is necessary to employ multiconfigurational methods, neither of the functionals perform satisfactorily. In these cases, DFT cannot describe the electronic configuration properly and therefore even when providing energetics in a satisfactory agreement the explanation behind the reactivity based on electronic structure is not valid. Besides the transferability of the functional to other complexes is not guaranteed. Whether a case is multireference (MR) or not is not influenced by the reaction mechanism: the radicals can be well described with singly occupied orbitals, thus both heterolytic and homolytic dissociation can be potentially described by DFT. The calculations indicated, that the nature of the Fe site determines whether a structure needs multiconfigurational treatment. In this study we calculated the spin population and partial charges, because in several DFT studies the spin density of the O atom of the Fe(IV)=O moiety is considered the determining factor of the activity. However, from this study it seems that DFT is not able to predict the spin density of this O on binuclear Fe sites. In fact, MR calculations predict a spin density of near 0 on this O atom. This indicates that the speculations about the importance of the spin density of the O, and the oversimplified picture of C-H bond dissociation based on molecular orbital theory is not correct.

Ab initio calculations present a unique opportunity to investigate catalysts and their performance on the atomic level gaining insight to individual pathways of a reaction. This is however the disadvantage of this method as well. In case of complex catalytic

systems, such as zeolites with extra-framework clusters, the possibility of potential topologies and reaction pathways is overwhelmingly numerous. When designing the calculations one must rely on chemical intuition, which leads to bias highly influencing the obtained results. For this reason with the improvement of computers the development of automated procedures gained interest [1–5]. These methods explore the potential energy surface without human bias and might lead to reaction paths that one would not consider intuitively. The increased number of calculations prevent the use of highly accurate methods and usually rely on lower level calculations, and only the most important parts are analysed with higher accuracy. And even with those methods chemical accuracy (usually defined as 4 kJ/mol [6]), which is necessary for the creation of kinetic models, might not be reached. For this reason currently reaction analysis with computational methods can supply us with semi-quantitative results at best. In some cases not even that is possible. As it is presented in Chapter 5, in multireference problems such high level computation intensive calculations are necessary for the correct description of a system, that geometry optimisation is not possible. Therefore if we want to gain chemical insight, we must rely on geometries obtained by DFT or Hartree-Fock (HF) methods. Some studies performed on smaller molecules found that these methods can predict surprisingly well the correct geometries, however according to Srnec *et al.* [7] DFT might not even be capable of predicting the correct reaction mechanism. As binuclear Fe sites and other transition metal clusters with multireference character are important catalysts the development of less calculation-intensive multiconfigurational HF [8–10] and DFT [11] methods is of utmost importance.

REFERENCES

- [1] Z. W. Ulissi, A. J. Medford, T. Bligaard and J. K. Nørskov, *Nature Commun.*, 2017, **8**, 14621.
- [2] K. Tran and Z. W. Ulissi, *Nature Catal.*, 2018, **1**, 696–703.
- [3] B. Meredig, A. Agrawal, S. Kirklin, J. E. Saal, J. W. Doak, A. Thompson, K. Zhang, A. Choudhary and C. Wolverton, *Phys. Rev. B: Condens. Matter*, 2014, **89**, 094104.
- [4] K. Gubaev, E. V. Podryabinkin and A. V. Shapeev, *J. Chem. Phys.*, 2018, **148**, year.
- [5] M. Sumita, X. Yang, S. Ishihara, R. Tamura and K. Tsuda, *ACS Central Science*, 2018, **4**, 1126–1133.
- [6] G. Piccini, M. Alessio and J. Sauer, *Angew. Chem. Int. Ed.*, 2016, **55**, 5235–5237.
- [7] J. Chalupský, T. A. Rokob, Y. Kurashige, T. Yanai, E. I. Solomon, L. Rulišek and M. Srnec, *J. Am. Chem. Soc.*, 2014, **136**, 15977–15991.
- [8] G. K. Chan and S. Sharma, *Annu. Rev. Phys. Chem.*, 2011, **62**, 465–481.
- [9] G. H. Booth, A. J. W. Thom and A. Alavi, *J. Chem. Phys.*, 2009, **131**, 054106.
- [10] J. E. T. Smith, B. Mussard, A. A. Holmes and S. Sharma, *J. Chem. Theory Comput.*, 2017, **13**, 5468–5478.
- [11] L. Gagliardi, D. G. Truhlar, G. L. Manni, R. K. Carlson, C. E. Hoyer and J. L. Bao, *Acc. Chem. Res.*, 2017, **50**, 66–73.

SAMENVATTING

IN dit proefschrift wordt onderzoek naar methaan-activering door Fe-oxo dimeren in poreuze Metal Organic Frameworks (MOF) en zeolieten beschreven. Bij de meeste studies die in het verleden zijn uitgevoerd, was de meeste aandacht voor de activering van de C-H binding van methaan. In dit proefschrift is het volledige reactiemechanisme, inclusief de activering van het Fe centrum en de over-oxidatie van methanol, naast de effecten van het poreuze materiaal bestudeerd.

In **Hoofdstuk 2** wordt het mechanisme van methaan-activering met waterstofperoxide over actieve centra in Fe/ZSM-5 zeoliet middels periodieke Dichtheidsfunctionaaltheorie (Density Functional Theory, DFT) onderzocht. De begintoestand van het Fe-centrum is gemodelleerd als een $[(\text{H}_2\text{O})_2\text{-Fe(III)-}(\mu\text{O})_2\text{-Fe(III)-}(\text{H}_2\text{O})_2]^{2+}$ cluster, gelokaliseerd buiten het geraamte in een zeolietporie en ladingsgecompenseerd door twee anionische kristalcentra. Door H₂O₂-activering worden verschillende Fe(III)-oxo en Fe(IV)-oxo complexen gevormd die potentieel reactief naar methaan-activering zijn. Deze actieve centra zijn in staat om de breuk van de eerste C-H binding te katalyseren, gevolgd door drie mogelijke reactiemechanismen. Deze mechanismen zijn: (a) heterolytische en (b) homolytische methaan-dissociatie als ook (c) Fenton-type activering waarbij vrije OH-radicalen als katalysator werken. Vastgesteld is dat Fe(III) de heterolytische en Fenton-type reacties katalyseert, Fe(IV) katalyseert de homolytische reacties. De berekeningen tonen aan dat het type O-activering (Fe=O, Fe- μ O-Fe of Fe-OH) uit energetisch oogpunt niet belangrijk is voor beide activeringstypes. De activering van de C-H binding wordt gevolgd door de vorming van MeOH en MeOOH en de regeneratie van het actieve centrum. Methanol kan worden gevormd, volgende uit alle types C-H bindingsactivering via de recombinitie van een CH₃ fragment en een OH-ligand, daarbij het actieve centrum reducerend. MeOOH kan worden gevormd uit de reactie van een CH₃-radicaal en een O₂-molecuul gevolgd door de verwijdering van een H-atoom uit het actieve centrum. Er is gevonden dat het Fenton-type mechanisme de laagste activerings-energie heeft. Weliswaar zijn de activerings-energieën voor de alternatieve heterolytische en homolytische mechanismen wat hoger, maar deze zijn nog steeds behoorlijk gunstig en naar verwachting mogelijk onder reactiecondities, resulterend in MeOH en MeOOH producten. De oxidant H₂O₂ is in competitie met het substraat CH₄ voor dezelfde actieve centra. De efficiëntie van de gewenste C-H oxo-functionaliserings is laag vanwege de energetisch gunstigere oxidatie van H₂O₂ naar O₂ en twee [H⁺]. Deze studie toont aan dat het

model niet kan worden vereenvoudigd tot een enkelvoudig actief centrum met een enkelvoudige reactiecyclus. Zelfs met de vereenvoudiging tot enkelvoudig actief centrum binnen een Fe cluster op een zeolietstructuur, kunnen meerdere actieve centra worden gevormd, die drie verschillende C-H bindingsactiveringen katalyseren.

In **Hoofdstuk 3** is een studie naar de methaan-activering over Fe in een MIL-53(Al) Metal Organic Framework (MOF) beschreven. MOFs zijn een alternatief voor zeolieten met de mogelijkheid voor oneindig veel structuren en daardoor een hoge aanpasbaarheid. Ook hebben MOFs het voordeel dat transitie-metalen in het geramte kunnen worden geïncorporeerd, waarbij uniforme clusters en daardoor gecontroleerde structuur en activiteit kunnen worden verkregen. In dit hoofdstuk is de reactie van methaan met H_2O_2 over een vergelijkbaar Fe-oxo dimeer-cluster als in Hoofdstuk 2 beschreven. Tevens is een monomeer Fe-oxo centrum onderzocht, dit naar aanleiding van een gedegen karakteriseringsstudie, die de aanwezigheid van dit centrum in het materiaal heeft aangetoond. Het gehele reactie-netwerk is bestudeerd en niet slechts de methaan-activering. Dit gehele reactie-netwerk is inclusief de vorming van het actieve centrum, de over-oxidatie van methaan naar CO_2 en de ontleding van H_2O_2 naar H_2O en O_2 . Aangezien de focus lag op de volgreacties na methaan-activering, is enkel de homolytische C-H bindingsactivering over MIL-53 MOF onderzocht. De reactiecomplexen zijn echter vergelijkbaar, en derhalve zijn waarschijnlijk heterolytische en Fenton-type activeringen ook mogelijk. Bij vergelijking van de activeringsenergieën van de C-H bindingsactivering over het dimere Fe-cluster in het zeoliet (Hoofdstuk 2) en over de Fe-MIL-53(Al) MOF, is een mogelijke conclusie dat de MOF een hogere activiteit heeft, aangezien de activeringsenergie lager is. Echter, bij de vergelijking in Figuur 4.4 van de activeringsenergie van de MOF (inclusief activering over de brugvormende O, de OH en de eindstandige O centra) met het zeoliet, kan geconcludeerd worden dat er clusters in het zeoliet met vergelijkbare of zelfs hogere activiteit aanwezig zijn. De berekeningen tonen aan dat de eerste dissociatie van de C-H binding in methaan slechts één van de snelheidsbepalende stappen is. De reactiebarrière naar de vorming van het actieve centrum, namelijk de dissociatie van de O-H binding van CH_3OH en de omzetting van HCOOH , is in dezelfde orde grootte. De oxidatie van H_2CO en CO heeft een lage reactiebarrière, wat in overeenstemming met experimentele waarnemingen is en de lage concentraties in reactiemengsels verklaart. De hoge selectiviteit van de oxidatiereactie over Fe-MIL-53(Al) naar gewenste enkelvoudig geoxideerde CH_3OH en CH_3OOH -producten wordt toegeschreven aan de beperkte coördinatie-vrijheid van de Fe centra die zijn ingebouwd in de uitgebreide octaëdrische $[\text{AlO}_6]$ structuurvormende ketens. Hierdoor worden de directe over-oxidatie reacties voordat productdesorptie van de actieve centra plaatsvindt voorkomen. Van belang is dat de berekeningen hebben

aangetoond dat de actieve centra voor de gewenste methaanoxidatie in staat zijn om veel efficiënter de directe H_2O_2 -ontledingsreactie te katalyseren. Daardoor is de huidige combinatie van actief centrum en reactanten niet geschikt voor het gewenste methaanvalorisatie-proces. Ook is er geen verschil tussen de H_2O_2 -ontledingsreacties over zeoliet of MOF, in beide gevallen is de reactiesnelheid hoog. De activiteit van monomere en dimere actieve centra zijn vergeleken. De berekeningen tonen aan dat, hoewel monomere centra door de formele oxidatietoestand van +5 in de reactie gaan, en dimere centra slechts een formele oxidatietoestand van +4 bereiken, de activiteit van deze centra vergelijkbaar is en dezelfde reactiestappen katalyseren.

In Hoofdstuk 2 is gevonden dat de ruimtelijke beperking van het zeoliet een significant effect heeft op de activering van de C-H binding. Dit leidde tot een verder onderzoek naar de effecten van de zeolietstructuur in **Hoofdstuk 4**, waar de rol van secundaire effecten zoals ruimtelijke beperking, flexibiliteit en multifunctionaliteit van de actieve centra op de reactiviteit van goed gedefinieerde ijzercomplexen in ZSM-5 zeoliet naar methaan oxo-functionaliseren. Lineaire energieschaling is toegepast voor deze analyse. Lineaire energieschalingswetten verbinden de kinetische en thermodynamische parameters van de belangrijkste elementaire deelstappen voor heterogeen gekatalyseerde reacties over gedefinieerde actieve centra op open oppervlakken. Deze schalingswetten geven een raamwerk voor screening door snelle berekeningen van nieuwe katalysatorfamilies, maar bieden ook op effectieve wijze een fundamentele grens aan de theoretisch bereikbare activiteit. Begrip van de toepassingsgrenzen van lineaire schalingswetten is derhalve cruciaal voor de ontwikkeling van voorspellende modellen in de katalyse. De berekende C-H activeringsdrempel over Fe-centra op verschillende locaties binnen zeolietporiën volgt over het algemeen de gerelateerde reactie-enthalpie en de waterstofaffiniteit van de actieve centra, weergegeven door de O-H bindingssterkte. Echter, ondanks de overeenkomst in geometrie en intrinsieke reactiviteit van de beschouwde actieve centra, zijn er significante afwijkingen van de lineaire schalingswetten gevonden met DFT-berekeningen. Drie belangrijke oorzaken voor deze afwijkingen zijn gevonden, namelijk (1) ruimtelijke beperkingen door de microporiën in het zeoliet, (2) flexibiliteit in coördinatie door het actieve centrum en (3) multifunctionaliteit. De laatste twee verschijnselen hebben een invloed op katalytische reactiemechanisme door het verzorgen van een samenwerkende reactieroute voor substraat-activering of door het mogelijk maken van stabilisatie van het intra-zeolietcomplex op de reactieroute. Directe stabilisatie van de overgangstoestand is mogelijk als de interactie van een nabijge OH-groep en het CH_3 -radicaal gerealiseerd wordt. Deze interactie verlaagt de energie van de overgangstoestand en verbreekt de schalingsrelatie, die wordt voorgesteld als een praktische strategie voor het ontwerp van katalysatoren voor methaan-activering. Deze uitkomst van de berekeningen wijst

op de noodzaak van het formuleren van multidimensionale eigenschap-activiteit-relaties, die zowel de intrinsieke chemie van de reactieve complexen als wel de secundaire effecten van hun omgevings- en dynamische karakteristieken meenemen.

In **Hoofdstuk 5** is een gedetailleerde vergelijkende analyse gemaakt van de prestaties van moderne kwantumchemische methoden voor het bestuderen van de C-H bindingsactivering in methaan door dimere ijzer-oxo clusters die in Fe-ZSM-5 zijn afgezet. Drie alternatieve reactiemechanismen, namelijk de homo- en heterolytische C-H activering en de Fenton-route zijn in de analyse meegenomen. De energieën van de reacties en de elektronische structuur van de betrokken tussenproducten zijn bestudeerd middels vijf populaire dichtheidsfunctionaaltheorie-methoden (GGA: OPBE, PBE(D3-BJ); meta-GGA: M06L, MN15L; en hybride: B3LYP functionaal). De resultaten zijn vergeleken met resultaten verkregen uit de multiconfigurational self-consistent field (SCF) methode gevolgd door tweede orde perturbatie-theorie (CASSCF/CASPT2). Door de toepassing van restricted active space SCF gevolgd door de PT2 methode (RASSCF/RASPT2) konden hogere orde activiteitsruimten worden verkregen. Kwalitatief vergelijkbare resultaten zijn verkregen met alle methoden. In het geval dat de tussenproducten kunnen worden beschreven zonder een multiconfiguratiele (MC, ook wel multireferentiële) golf functie (hierbij hebben alle orbitalen een integer (0, 1 of 2) bezettingsgetal), geven MN15L en M06L de beste resultaten. Hoewel alle onderzochte methoden in deze gevallen de van de hogere niveau golf functie-methode afgeleide energietrends geven, onderschatten ze in geringe mate de reactiebarrière en energie. De spinladder is ook onderzocht en de berekeningen tonen aan dat in dit geval ofwel de hoge spin ofwel de verbroken symmetrie lage spin potentiaalenergie-oppervlakte toegepast zou moeten worden om het reactieprofiel te beschrijven. Natuurlijk is dit alleen geldig wanneer de lokale spin van de ijzeratomen in de hoge-spin toestand blijft gedurende het verloop van der reactie. Ook moeten de spintoestanden van de intermediären niet worden meegenomen, zelfs als zij een lagere energie hebben. Dit is omdat de elektronische configuratie intrinsiek incorrect is. Wanneer het echter noodzakelijk is om multiconfiguratiele methoden toe te passen, levert geen van de methoden een bevredigend resultaat. In deze gevallen kan DFT de elektronische configuratie niet juist weergeven en daarom, zelfs als de energieniveaus in goede overeenstemming zijn, is de verklaring achter het reactieverloop (gebaseerd op de elektronische structuur) niet juist. Daarnaast is ook de toepasbaarheid van de methode op andere complexen niet gegarandeerd. Het reactiemechanisme heeft invloed op of een geval wel of niet multireferentieel is: de radicalen kunnen door enkelvoudig bezette orbitalen worden beschreven, dus zowel hetero- als homolytische dissociatie kunnen door DFT worden beschreven. In dit onderzoek zijn de spinpopulatie en deelladingen berekend, omdat verschillende DFT-studies

de spindichtheid van het O-atoom van het Fe(IV)=O ensemble als een beslissende factor voor de activiteit beschouwen. Uit dit onderzoek blijkt echter dat DFT niet is staat is om de spindichtheid van deze O op de dimere Fe centra te voorspellen. MC berekeningen geven juist een spindichtheid van bijna 0 op dit zuurstofatoom. Dit laat zien dat veronderstellingen over het belang van spindichtheid van de zuurstof en het oververeenvoudigde beeld van C-H bindingsdissociatie gebaseerd op moleculaire orbitaaltheorie niet juist zijn.

Ab initio berekeningen bieden een unieke kans om katalysatoren en hun werking op atomaire schaal te onderzoeken en geven inzicht in deelstappen in een reactie. Dit is echter ook het nadeel van de methode. Bij complexe katalytische systemen, zoals zeolieten met clusters buiten het geraamte, is het aantal mogelijke topologieën en reactieroutes overweldigend groot. Bij het ontwerp van de berekeningen moet men vertrouwen op chemische intuïtie, dit leidt tot voorkeuren die de resultaten sterk beïnvloeden. Om deze reden, en samen met de verbetering van computers, heeft de ontwikkeling van automatische procedures meer aandacht gekregen [1–5]. Deze methoden verkennen de potentiaalenergie-oppervlakte zonder menselijke voorkeur en leiden mogelijk tot reactieroutes die men intuïtief niet zou beschouwen. Het gebruik van methoden met hoge nauwkeurigheid is niet mogelijk vanwege het grote aantal berekeningen, daardoor worden berekeningen uitgevoerd op een lager niveau, slechts de belangrijkste delen worden met hoge nauwkeurigheid geanalyseerd. Zelfs met deze methoden kan de chemische nauwkeurigheid (gewoonlijk gedefinieerd als 4 kJ/mol [6]), noodzakelijk voor het maken van kinetische modellen, buiten bereik liggen. Hierdoor leveren de huidige reactie-analyses met computerberekeningen in het beste geval semi-kwantitatieve resultaten. In sommige gevallen is zelfs dat niet mogelijk. Zoals in Hoofdstuk 5 is beschreven, is voor multireferentie-vraagstukken, de toepassing van intensieve berekeningen op een hoog niveau noodzakelijk voor een juiste beschrijving van het systeem. Hierdoor is een optimalisatie van de geometrie niet mogelijk. Voor het verkrijgen van chemisch inzicht is derhalve nodig om DFT of HF methoden te gebruiken. Sommige onderzoeken naar kleinere moleculen tonen aan dat deze methoden verrassend goed de juiste geometrieën voorspellen, anderzijds is volgens Srnc *et al.* [7] DFT wellicht zelfs niet geschikt voor het voorspellen van het juiste reactiemechanisme. Aangezien dimere Fe-centra en andere overgangsmetaal-clusters met multireferentieel karakter belangrijke katalysatoren zijn, is de ontwikkeling van minder rekenintensieve multiconfiguratiele Hartree-Fock [8–10] en DFT [11] methoden van het grootste belang.

BIBLIOGRAFIE

- [1] Z. W. Ulissi, A. J. Medford, T. Bligaard and J. K. Nørskov, *Nature Commun.*, 2017, **8**, 14621.
- [2] K. Tran and Z. W. Ulissi, *Nature Catal.*, 2018, **1**, 696–703.
- [3] B. Meredig, A. Agrawal, S. Kirklín, J. E. Saal, J. W. Doak, A. Thompson, K. Zhang, A. Choudhary and C. Wolverton, *Phys. Rev. B: Condens. Matter*, 2014, **89**, 094104.
- [4] K. Gubaev, E. V. Podryabinkin and A. V. Shapeev, *J. Chem. Phys.*, 2018, **148**, year.
- [5] M. Sumita, X. Yang, S. Ishihara, R. Tamura and K. Tsuda, *ACS Central Science*, 2018, **4**, 1126–1133.
- [6] G. Piccini, M. Alessio and J. Sauer, *Angew. Chem. Int. Ed.*, 2016, **55**, 5235–5237.
- [7] J. Chalupský, T. A. Rokob, Y. Kurashige, T. Yanai, E. I. Solomon, L. Rulišek and M. Srnc, *J. Am. Chem. Soc.*, 2014, **136**, 15977–15991.
- [8] G. K. Chan and S. Sharma, *Annu. Rev. Phys. Chem.*, 2011, **62**, 465–481.
- [9] G. H. Booth, A. J. W. Thom and A. Alavi, *J. Chem. Phys.*, 2009, **131**, 054106.
- [10] J. E. T. Smith, B. Mussard, A. A. Holmes and S. Sharma, *J. Chem. Theory Comput.*, 2017, **13**, 5468–5478.
- [11] L. Gagliardi, D. G. Truhlar, G. L. Manni, R. K. Carlson, C. E. Hoyer and J. L. Bao, *Acc. Chem. Res.*, 2017, **50**, 66–73.

ACKNOWLEDGEMENTS

I thank my supervisor, Evgeny for the guidance and patience that made my PhD possible. I would like to acknowledge the contribution of Guanna, who taught me how to use VASE, read my manuscripts and discussed my results. Jorge, thank you for giving me the opportunity to do a PhD at TU Delft. Lena, you were my favourite master student. I would like to thank my collaborators from the University of Minnesota, Laura and Varinia for their input.

Els and Caroline, thank you for taking care of all bureaucratic matters.

I acknowledge the contribution of Allert and Bart, my colleagues at Nouryon who translated some parts of this thesis to Dutch.

I thank the members of the crochet club, Alma, Ina, Sonia, Irina and Nastya for wine therapy. Ina and Annika, thank you for keeping me in shape. I thank my office mates, Robert, Guanna, Jara, Alma, Ina and Filipe for being fun. I miss throwing stuff at my office mates at my new job. Robbert, thank you for protecting Annika, Guanna and me on the Russian metro. Edu, thank you for being the organiser of the Friday drinks.

I thank my manager, Bart for being lenient in the period when I was writing my thesis during office hours.

I thank my family for supporting me even when they disagreed with my decisions.

Finally I thank my husband, Máté for preparing dinner every evening and thus contributing to the success of my PhD.

LIST OF PUBLICATIONS

PUBLICATIONS RELATED TO THIS THESIS

A. I. Olivos-Suarez, Á. Szécsényi, E. J. M. Hensen, J. Ruiz-Martinez, E. A. Pidko, and J. Gascon, Strategies for the Direct catalytic valorization of methane using heterogeneous catalysis: challenges and opportunities, *ACS Catalysis*, **6** (2016) 2965-2981.

D. Osadchii, A. I. Olivos-Suarez, Á. Szécsényi, G. Li, M. A. Nasalevich, A. I. Dugulan, P. Serra-Crespo, E. J. M. Hensen, S. L. Veber, M. V. Fedin, G. Sankar, E. A. Pidko, and J. Gascon, Isolated Fe sites in Metal Organic Framework catalyze the direct conversion of methane to methanol, *ACS Catalysis*, **8** (2018) 5542-5548.

Á. Szécsényi, G. Li, J. Gascon, and E. A. Pidko, Mechanistic complexity of methane oxidation with H₂O₂ by single-site Fe/ZSM-5 catalyst, *ACS Catalysis*, **8** (2018) 7961-7972.

Á. Szécsényi, G. Li, J. Gascon, and E. A. Pidko, Unraveling reaction networks behind the catalytic oxidation of methane with H₂O₂ over a mixed-metal MIL-53(Al,Fe) MOF catalyst, *Chemical Science*, **9** (2018) 6765-6773.

Á. Szécsényi, E. Khramenkova, G. Li, J. Gascon, and E. A. Pidko, Breaking linear scaling relationships with secondary interactions in zeolite micropores: a case study of methane oxidation by Fe/ZSM-5 zeolite, *submitted*

Á. Szécsényi, V. Bernales, J. Gascon, L. Gagliardi, E. A. Pidko, Multireference problem in methane activation by diiron sites in zeolites, *in preparation*

OTHER PUBLICATIONS

I. Vollmer, N. Kosinov, Á. Szécsényi, G. Li, I. Yarulina, E. Abou-Hamad, A. Gurinov, S. Ould-Chikh, A. Aguilar, J-L. Hazemann, E. A. Pidko, E. J. M. Hensen, F. Kapteijn, J. Gascon, A site-sensitive quasi-in situ strategy to characterize Mo/HZSM-5 during activation, *Journal of Catalysis*, **370** (2019) 321-331.

PRESENTATIONS

Á. Szécsényi, E. Khramenkova, G. Li, J. Gascon, E. A. Pidko, *Computational study of Fe containing porous catalysts for selective methane oxidation*, 5th International School-Conference on Catalysis for Young Scientists, Moscow, Russia, 2018 (oral)

Á. Szécsényi, E. Khramenkova, G. Li, J. Gascon, E. A. Pidko, *Magic of linear correlations – Selective methane oxidation over high valent Fe sites – A DFT study*, XIXth Netherlands' Catalysis and Chemistry Conference, Noordwijkerhout, Netherlands, 2018 (poster)

D. Osadchii, A. I. Olivos-Suárez, Á. Szécsényi, G. Li, M. A. Nasalevich, I. A. Dugulan, P. Serra Crespo, E. J. M. Hensen, S. L. Veber, M. V. Fedin, G. Sankar, E. A. Pidko, J. Gascon, *Selective oxidation of methane by Fe sites incorporated into MIL-53(Al) metal organic framework*, 6th Chemistry as Innovating Science Conference, Veldhoven, Netherlands, 2017 (oral)

Á. Szécsényi, G. Li, J. Gascon, E. A. Piko, *Methane oxidation to methanol over Fe sites encapsulated in MOF lattice*, 2nd European Conference on Metal Organic Frameworks and Porous Polymers, Delft, Netherlands, 2017 (poster)

Á. Szécsényi, V. Bernalez, L. Gagliardi, E. A. Pidko, *Theoretical Study of Methane Oxidation Catalysed by Diiron-complex Deposited on ZSM5 zeolite*, XVIIIth Netherlands' Catalysis and Chemistry Conference, Noordwijkerhout, Netherlands, 2017 (oral)

D. Osadchii, A. I. Olivos-Suárez, Á. Szécsényi, G. Li, M. A. Nasalevich, I. A. Dugulan, P. Serra Crespo, E. J. M. Hensen, S. L. Veber, M. V. Fedin, G. Sankar, E. A. Pidko, J. Gascon, *Direct oxidation of methane to methanol catalysed by metal organic framework Fe containing MIL-53*, Fundamentals and Applications of Advanced Porous Materials Conference, Adelaide, Australia, 2016 (oral)

Á. Szécsényi, G. Li, J. Gascon, E. A. Piko, *Selective oxidation of CH₄ with H₂O₂ over Fe containing ZSM-5 and MIL-53*, The 26th Conference of the Condensed Matter Division of the European Physical Society, Groningen, Netherlands, 2016 (oral)

Á. Szécsényi, G. Li, J. Gascon, E. A. Piko, *Periodic DFT study about the mechanism of direct oxidation of methane with H₂O₂ over Fe-ZSM-5*, 16th International Conference on Theoretical Aspects of Catalysis, Zakopane, Poland, 2016 (poster)

Á. Szécsényi, G. Li, J. Gascon, E. A. Piko, *On the nature of active sites and mechanism of selective methane oxidation with H₂O₂ over Fe-ZSM-5 catalyst: a periodic DFT study*, XVIIth Netherlands' Catalysis and Chemistry Conference, Noordwijkerhout, Netherlands, 2016 (oral)

CURRICULUM VITÆ

Szécsényi Ági was born on the 27th of January in 1990 in Szekszárd, Hungary. She grew up in Paks with her parents and sister. She finished her elementary and high school education there in 2008.

She attended the Budapest University of Technology where she studied chemical engineering on the process technology track. During her bachelor she participated in two research projects. At first she did preparative colloid chemistry synthesising nanoparticles for drug delivery purposes under the supervision of Nagyné Dr. Naszályi Lívía, then she was measuring reaction kinetics



in supercritical carbon dioxide in the group of Kőzelné Dr. Székely Edit. She continued this project during her master studies. She had the opportunity to study for 6 months in the Netherlands at the Delft University of Technology with Erasmus Scholarship in 2013 where she was assigned to the group of Prof. dr. Jorge Gascon for a project work and was offered a PhD position there at the end of the semester.

She returned to the Netherlands on the 1th of September in 2014, when she started her PhD under the supervision of Prof. dr. Evgeny Pidko. In this book you can read in detail about her work on the modelling of methane oxidation in porous catalysts.

Since the 1th of October in 2018 she has been working for Nouryon (former AkzoNobel) in the RD&I Salt and Crystallization Group, where her main activity is process modelling of salt plants.

Currently she resides in Amersfoort where she spends her days in happiness with her husband, Máté.